

Epitaxial Growth of Single Crystal Noble Metals for Plasmonic and Nanophotonic Applications

by

Sasan V. Grayli

M.A.Sc. (School of Engineering), Simon Fraser University, 2012

B.A.Sc., Aachen University of Applied Sciences, 2007

Thesis Submitted in Partial Fulfillment
of the Requirements for the Degree of
Doctor of Philosophy

in the
Department of Chemistry
Faculty of Science

© **Sasan V. Grayli 2019**

SIMON FRASER UNIVERSITY

Spring 2019

All rights reserved.

However, in accordance with the *Copyright Act of Canada*, this work may be reproduced, without authorization, under the conditions for "Fair Dealing." Therefore, limited reproduction of this work for the purposes of private study, research, criticism, review and news reporting is likely to be in accordance with the law, particularly if cited appropriately.

Approval

Name: Sasan V. Grayli
Degree: Doctor of Philosophy
Title of Thesis: *Epitaxial Growth of Single Crystal Noble Metals for Plasmonic and Nanophotonic Applications*

Examining Committee:

Chair: Michael Eikerling, Professor

Gary W. Leach
Senior Supervisor
Associate Professor

Neil Branda
Supervisor
Professor

Hua-Zhong Yu
Supervisor
Professor

Steven Holdcroft
Internal Examiner
Professor

Alex Brolo
External Examiner
Professor
Department of Chemistry
University of Victoria

Date Defended/Approved: January 17, 2019

Abstract

Material quality and crystallinity play an important role in the activity of plasmonic devices. Plasmonic structures made from monocrystalline metals may be expected to display much higher efficiency and stability than polycrystalline devices which are subject to many losses due to the presence of grain boundaries and defects. With the help of a novel epitaxial electroless deposition (EED) chemistry, ultrasmooth gold films can be grown on monocrystalline silver surfaces. In this approach, the electrochemical incompatibility of gold and silver can be overcome in concentrated sodium hydroxide (NaOH) solution (1 M), where the presence of OH^- causes a decrease in the reduction potential of gold cations by forming $\text{Au}(\text{OH})_4^-$ complexes ($E \approx 0.56 \text{ V}$), an increase in the oxidation potential of the silver electrode ($E \approx 1.40 \text{ V}$), and acts as a reducing agent. As a result, ultrasmooth monocrystalline gold films are grown with the same crystalline orientation as the underlying silver film. This chemistry enables the growth of gold from a few monolayers up to few hundreds of nanometers uniformly over a large area. Furthermore, this approach enables the fabrication of large area metasurfaces made of gold and silver epitaxially grown nanostructures that can be used in a variety of different applications. The growth of gold films and nanostructures can also be manipulated by the introduction of anionic species during the deposition, and leads to the formation of surface nanostructures with specific shape, due to preferential interaction of the anions with certain facets of the growing crystalline structures. Subtractive fabrication of bowtie nanoantenna devices by focussed ion beam milling of gold films deposited by EED chemistry are compared to those deposited by conventional physical vapour deposition (PVD) methods using two-photon photoluminescence spectroscopy and imaging methods, employed as a proxy for plasmonic excitation. The monocrystalline EED gold films demonstrate excellent pattern transfer characteristics, functional device yield, improved tailoring of local near fields, as well as increased thermal and mechanical stability compared to devices patterned identically on polycrystalline PVD films. Taken together, the work described in this thesis represents a novel and powerful new approach to the fabrication of monocrystalline noble metal films and nanostructures useful for plasmonic and metamaterial research and application.

Keywords: Plasmonic metals, nanofabrication, nano-antennas, electrochemistry, capping agent, localized surface plasmon, plasmonic devices, thin film, electroless deposition, epitaxial growth, monocrystalline, nanostructures

Dedication

This Work is dedicated to those who supported me during my doctorate work, especially my parents who taught me to never give up.

Acknowledgements

I would like to thank Leach Lab for the help and support during my doctorate work, the 4D LABS for enabling the use of the facility and specifically Dr. Xin Zhang for his scientific support, LASIR and Dr. Saeid Kamal for assisting in experimental work and Professor Gary Leach for his scientific supervision and guidance.

Table of Contents

| | |
|--|-----------|
| Approval..... | ii |
| Abstract..... | iii |
| Dedication..... | v |
| Acknowledgements..... | vi |
| Table of Contents..... | vii |
| List of Figures..... | ix |
| List of Acronyms or Glossary..... | xvi |
| Image..... | xviii |
| | |
| 1. Introduction | 1 |
| 1.1. Surface Plasmons | 3 |
| 1.2. Localized Surface Plasmons | 8 |
| References..... | 14 |
| | |
| 2. Experimental Methods | 16 |
| 2.1. X-Ray Diffraction Analysis | 16 |
| 2.2. Scanning Electron Microscopy | 18 |
| 2.3. Transmission Electron Microscopy | 21 |
| 2.4. Atomic Force Microscopy | 24 |
| 2.5. Electron Beam Lithography | 27 |
| 2.6. Focused Ion Beam | 30 |
| 2.7. Physical Vapour Deposition..... | 32 |
| 2.8. Integrating Sphere Absorption Measurements..... | 36 |
| 2.9. Multiphoton Photoluminescence Analysis..... | 38 |
| 2.10. Raman and Surface Enhanced Raman Spectroscopy..... | 40 |
| 2.11. Finite-Difference Time-Domain..... | 43 |
| References..... | 44 |
| | |
| 3. Electrochemical Reduction of Metal Ions from Hydroxide Ion Oxidation..... | 49 |
| | |
| 4. Scalable Green Synthesis of Monocrystalline Noble Metal Nanostructures for Low-Loss Plasmonic and Nanophotonic Applications..... | 65 |
| References..... | 78 |
| <i>Supplementary Materials.....</i> | <i>82</i> |
| Single Crystal Ag(100)/Si(100) Substrates | 82 |
| Physical Vapour Deposition of Gold Films..... | 83 |
| Electroless Growth of Noble Metal Films | 83 |
| Cyclic Voltammetry..... | 84 |
| Nanopillar Array Fabrication | 85 |
| 2-Dimensional X-ray Diffraction of Au films | 88 |
| Cross-sectional SEM and TEM Analysis | 89 |
| Surface Roughness Analysis..... | 89 |
| Focused-Ion Beam Nano-Patterning | 91 |

| | |
|---|------------|
| Electron-Beam Lithographed Lines | 92 |
| Laser Scanning Microscopy | 93 |
| Sheet Resistance | 94 |
| Spectroscopic Ellipsometry | 94 |
| | |
| 5. Shape-Controlled Growth of Single Crystal Gold Surface Nanostructures for Plasmonic and Photonic Applications | 98 |
| References..... | 111 |
| <i>Supplementary Materials</i> | 114 |
| Single crystal silver Ag(100) substrate preparation:..... | 114 |
| Gold (Au) nanopyramid synthesis with sulphate ion (SO ₄ ²⁻):..... | 115 |
| Au growth under influence of chloride ion (Cl ⁻): | 116 |
| Au growth under influence of bromide ion (Br ⁻):..... | 116 |
| Au growth under influence of Cl ⁻ and SO ₄ ²⁻ ions: | 117 |
| Au growth under influence of Br ⁻ and SO ₄ ²⁻ ions:..... | 117 |
| Single crystal Au(100) substrate preparation:..... | 118 |
| Nano-electrode array patterning using electron-beam lithography (EBL):..... | 118 |
| Au growth in nano-electrode arrays:..... | 119 |
| Rhodamine 6G (R6G) preparation for surface enhanced Raman spectroscopy (SERS): | 119 |
| Benzoic acid (BA) preparation for SERS: | 120 |
| Sample preparation for transmission electron microscopy (TEM): | 120 |
| Nanopyramid surface absorption measurement: | 120 |
| | |
| 6. High Efficiency, Single Crystal, Plasmonic Gold Nano-Antennas via Epitaxial Electroless Deposition | 123 |
| 6.1. Yield and Activity as a Function of Film Quality | 126 |
| 6.2. Polarization Dependence of the Nano-Antennas | 128 |
| 6.3. Device Stability | 131 |
| 6.4. Plasmonic Activity and Field Enhancement | 133 |
| 6.5. Conclusion | 135 |
| <i>Supplementary Materials</i> | 139 |
| Monocrystalline Silver Deposition on Silicon | 139 |
| Electroless Deposition of Monocrystalline Gold on Silver | 139 |
| Bowtie Gold Nano-Antenna Fabrication..... | 140 |
| Benzoic Acid (BA) Preparation for SERS | 140 |
| Finite-Difference Time-Domain Simulations | 141 |
| Laser Scanning Microscopy | 141 |
| Surface Enhanced Raman Spectroscopy (SERS) | 142 |
| | |
| 7. Future Work and the Impact of EED | 143 |
| References..... | 148 |
| | |
| Appendices..... | 150 |
| Appendix Lift-Out Process for TEM..... | 151 |

List of Figures

| | |
|---|----|
| Figure 1: Gold nanorods were produced with synthetic method. The color red is due to the dispersion effect. | 2 |
| Figure 2. Schematic of the excitation of the plasmon at the metal-dielectric interface, where E represents the electric field and H_y is the magnetic field vector. | 4 |
| Figure 3. Decay of the SPP at the metal-dielectric interface. | 4 |
| Figure 4. The diagram shows the nonlinear dispersion relation of SP's in red and the linear dispersion relation of incident photons without the prism in orange and incident photons at the total internal reflection in blue. | 6 |
| Figure 5. Schematic of Otto configuration is shown. The blue dashed lines represent the surface plasmonic wave induced evanescently by the electric field of the incident photons which have undergone total internal reflection in the prism. | 7 |
| Figure 6. Kretschmann configuration is shown. The evanescent waves generated by the incident photons at the point of reflection in the prism can reach to the other side of a thin metal film and propagate as SPs at the metal-air interface. | 8 |
| Figure 7. Schematic of the excitation of localized surface plasmons in nanoparticles is shown. This non-propagating plasmonic mode occurs in nanoparticles in the presence of electromagnetic waves. | 9 |
| Figure 8. Polarized Optical response of a gold nanopillar array measured in an integrating sphere with incident angle at 20° | 13 |
| Figure 9. Illustration of X-ray diffraction by crystalline planes of a solid crystal. | 17 |
| Figure 10. The 2D X-ray diffractometer manufactured by Rigaku which is located in 4D LABS facility located at Simon Fraser University. | 18 |
| Figure 11. Schematic of a scanning electron microscope. Different components of the electron microscope are shown in this figure. | 20 |
| Figure 12. Electron Microscopes located in 4D LABS, a) FEI Helios NanoLab 650 and b) NanoSEM 430 | 21 |
| Figure 13. The FEI Tecnai Osiris STEM system located in the center of soft materials (CSM) of 4D LABS facility | 24 |
| Figure 14. An NaioAFM AFM, which was used to measure surface roughness in this thesis work. | 27 |

| | |
|--|----|
| Figure 15. The e_LiNE EBL system in 4D LABS clean room facility. | 29 |
| Figure 16. Schematic of a beam of focused ions used to remove atoms from the surface. The scattered ions can be used to form an image of the specimen, similar to electron imaging in SEM. | 31 |
| Figure 17. The Helios dual beam microscope located at CSM in 4D LABS facility. | 32 |
| Figure 18. The e-beam/thermal PVD at 4D LABS clean room which is listed as PVD 3. | 35 |
| Figure 19. The custom build PVD at the 4D LABS facility which is listed as PVD 5. | 36 |
| Figure 20. The integrating sphere and the optical components for directing the light into the sphere that were used for the absorption measurements. | 38 |
| Figure 21. Multi-photon fluorescence microscopes available in LASIR facility, a) is a Zeiss LSM510 two photon scanning confocal microscope housed in LASIR facility at UBC and b) is Leica SP5 laser scanning confocal two photon microscope located at LASIR at SFU. | 40 |
| Figure 22. Illustration of energy levels in a Raman scattering process. | 41 |
| Figure 23. A Renishaw inVia Raman microscope used for Raman spectroscopy and demonstrating the SERS from the substrates made in this thesis work. | 43 |
| Figure 24. Illustration of galvanic replacement of Ag atoms by Au ³⁺ ions that leads to formation of a porous and polycrystalline gold film. | 51 |
| Figure 25. Single crystal Ag(100) film which has undergone galvanic replacement by Au cations obtained by dissolving HAuCl ₄ in deionized water; a) shows the macroscopic appearance of the Ag(100) film and b) shows the SEM image of the galvanically replaced region. | 52 |
| Figure 26. CV scan of Ag(100) WE in 1 M NaOH solution (scan rate 50 mV/s) measured with respect to a Ag/AgCl reference electrode. | 55 |
| Figure 27. Electroless deposition of Au for 30 s. a)-c) are SEM images at different magnifications and d) is a tilt view SEM image showing Au nucleation at many positions on the growing film taken at 40° tilt angle. | 57 |
| Figure 28. SEM images of deposited Au after a) 1 minute, b) 5 minutes, c) 8 minutes and d) 15 minutes of deposition. | 58 |
| Figure 29. Thickness of the Au film as a function time for 15 minutes, 20 minutes and 30 minutes was shown. | 60 |

| | |
|--|----|
| Figure 30. Measured Au film thickness versus deposition time for films deposited under the same conditions..... | 61 |
| Figure 31. Epitaxial electrochemical deposition of monocrystalline noble metals for low-loss plasmonic, nanophotonic, and nanoelectronics applications. Left: Solution phase reduction of $\text{Au}(\text{OH})_4^-$ ions to Au atoms at the Ag(100)/aqueous alkaline electrolyte interface. Upper Central: Deposition of a uniform, ultrasmooth, epitaxial, single crystal Au(100) film of controlled thickness. Upper Right: Excitation of a bowtie nanoantenna fabricated via FIB milling of the single crystal Au film. Lower Central: Solution phase deposition of Au into pores formed by patterning a PMMA resist layer provides an oriented crystalline nanostructured metamaterial array. | 67 |
| Figure 32. (a) 2D-XRD of gold deposited from an uncontrolled pH HAuCl_4 solution onto a Ag(100)/Si(100) single crystal substrate. (b) 2D-XRD of gold deposited from a pH 14 HAuCl_4 solution onto a Ag(100)/Si(100) single crystal substrate. (c) Top view SEM of a 100 nm thick gold film deposited from pH 14 HAuCl_4 solution onto a Ag(100)/Si(100) single crystal substrate. (d) Top view SEM of a 100 nm thick Au film evaporated onto an atomically flat Si(100) substrate with a 5nm Cr adhesion layer. High resolution transmission electron microscopy of pH 14 solution-deposited, 70 nm thick Au film onto a Ag(100)/Si(100) single crystal substrate: (e) TEM cross section image of protective Pt-overlayer/Au(100)/Ag(100) /Si(100) with Pt appearing in the lower left and silicon wafer appearing dark in the upper right hand region of the image. (f)-(h) Elemental mapping of the Au(100)/Ag(100)/Si(100) structure (silicon upper right). (i) Cross-sectional TEM image of the Pt /Au(100)/Ag(100) interface region. (j) Expanded view of the Au(100)/Ag(100) interface. (k) The Au(100)/Ag(100) interface showing alignment of atomic planes across the interface. (l) Selected area electron diffraction from the region highlighted in (k) viewed along the [011] zone axis. | 70 |
| Figure 33. Focused ion beam milling of 100 nm thick, polycrystalline, PVD-deposited Au nanostructures and monocrystalline, solution-deposited Au nanostructures. SEM images of (a) ring resonator structures from polycrystalline, PVD-deposited Au (left) and solution-deposited Au (right), (b) 30 nm wide lines in PVD-deposited Au (left) and solution-deposited Au (right), (c) patterned windows in PVD-deposited Au (left) and solution-deposited Au (right), (d) 90 nm diameter holes patterned in PVD-deposited Au (left) and solution-deposited Au (right). | 72 |

- Figure 34. Single crystal versus polycrystalline bowtie nanoantenna fabrication and performance. SEM image of bowtie nanoantenna patterned by FIB milling of (a) solution-deposited Au(100) and (b) PVD-deposited polycrystalline Au films. Scanning laser microscope image of 2PPL (horizontally-polarized, 780 nm excitation, 120 fs pulse duration) of 3 x 3 bowtie nanoantenna arrays fabricated from (c) solution-deposited Au(100) and (d) PVD-deposited polycrystalline Au films. 2PPL image of (e) individual solution-deposited Au(100) nanoantenna and (f)-(g) individual PVD-deposited polycrystalline Au nanoantennas. 74
- Figure 35. Additive patterning of single crystal metals through solution-deposition on EBL-patterned substrates. (a) SEM top view image of a large area crystalline Au nanopillar array with pillar diameter of 120 nm and period 550 nm, solution-deposited on an EBL-patterned, solution-deposited Au(100) substrate. (b) SEM 30° tilt view image of an individual gold nanopillar exhibiting crystalline facets. (c) Pillar-resolved 2PPL from the Au plasmonic metamaterial array. (d) SEM top view image of a crystalline silver nanopillar solution-deposited onto a solution-deposited Au(100) substrate, exhibiting well defined top facets. (e) SEM top view image of a faceted gold-capped silver nanopillar obtained by solution-deposition of 10 nm of Au onto a Ag(100) nanopillar array. (f) SEM top view image of high aspect ratio concentric square Au nanowire structures EBL-deposited from solution onto a Ag(100) substrate. (g) The wires appear continuous and are characterized by widths of 40 nm and lengths of 2 mm, limited by e-beam exposure and pattern dimension, respectively. (h) 2PPL image of the concentric square nanowire structure described in (f) excited by 800 nm light polarized horizontally, perpendicular to the vertical nanowire axes. 76
- Figure 36. Photo of a Au film following Au deposition onto a single crystal Ag(100)/Si(100) substrate from (a) an electroless deposition bath containing H₂AuCl₄ at uncontrolled pH and b) an electroless deposition bath containing H₂AuCl₄ at pH 14 (1 cm x 1 cm substrate)..... 84
- Figure 37. Cyclic Voltammetry of a Ag(100)/Si(100) single crystal working electrode immersed in a 1 M OH⁻ electrolyte. The lowest potential oxidation wave (indicated by the red arrow) appears at 0.375 V versus Ag/AgCl. 85
- Figure 38. SEM of Au nanopillars (100 nm height, 700 nm period, 450 nm diameter) grown on Au(100) substrate through a nano-electrode array formed with PMMA A4 resist..... 87
- Figure 39. A cross-sectional SEM image of the electrolessly deposited Au film on single crystal Ag(100). 89
- Figure 40. AFM surface topography image of a) solution-deposited, electroless single crystal Au film and b) thermally evaporated, polycrystalline Au film. The area of the scanned regions is approximately 700 x 700 nm². 90

| | |
|---|-----|
| Figure 41. The constructed 3D AFM image of the surface of a) solution-deposited, electroless single crystal Au film and b) thermally evaporated, polycrystalline Au film..... | 91 |
| Figure 42. Top view SEM image of a FIB-milled bowtie nanoantenna fabricated with a) epitaxially-grown solution-deposited monocrystalline Au, and b) thermally evaporated polycrystalline Au..... | 92 |
| Figure 43. Top view SEM image of epitaxially grown Au lines on a single crystal Ag(100) substrate patterned by EBL and deposited from an alkaline Au(OH) ₄ ⁻ deposition bath as described. | 93 |
| Figure 44. The real (n) and imaginary (k) parts of the refractive index as determined from spectroscopic ellipsometry of a 100 nm thick polycrystalline Au film deposited by thermal evaporation (blue) and a 100 nm thick, electroless, solution-deposited monocrystalline Au(100) film (red). | 95 |
| Figure 45. The effect of sulfate anion on single crystal Au deposition. a) Plan view SEM of a smooth, epitaxial, single crystal Au film deposited through alkaline electroless deposition of a HAuCl ₄ solution onto a Ag(100)/Si(100) single crystal substrate. b) Tilt view SEM of a Au-nanopyramid textured Au film grown as in a) but with the incorporation of 0.25 M NaSO ₄ in the deposition bath. c) Expanded view of b) highlighting the strong square pyramidal shape preference, the common orientation of square pyramids with respect to the underlying substrate, and the smooth facets of the nanostructures. | 101 |
| Figure 46. a) and b) are the elemental mapping done by TEM, b) shows the Au film (green) grown on top of Ag film (red), c) is a TEM image in which the angle of the pyramid's facet and the surface is measured and d) is a high-resolution TEM image of side of a nanopyramid in which the angle between the crystalline lattice is measured. | 102 |
| Figure 47. SERS spectra obtained from a) BA-coated Au nanopyramids, BA-coated monocrystalline Au(100) film and a silicon wafer reference sample, b) R6G-coated Au nanopyramids, R6G-coated monocrystalline Au(100) film and a silicon wafer reference sample. | 105 |
| Figure 48. Growth of single crystal Au films under the influence of different anionic additive species. Top-view SEM image of a Au film grown under the influence of a) 0.25 M Cl ⁻ , b) expanded top-view SEM of one of the structures identified in a). Top-view SEM image of a Au film grown under the influence of c) 0.75 M Br ⁻ , d) 0.25 M SO ₄ ²⁻ , e) 0.25 M Cl ⁻ and 0.25 M SO ₄ ²⁻ , and (f) 0.25 M SO ₄ ²⁻ and 0.75 M Br ⁻ | 107 |

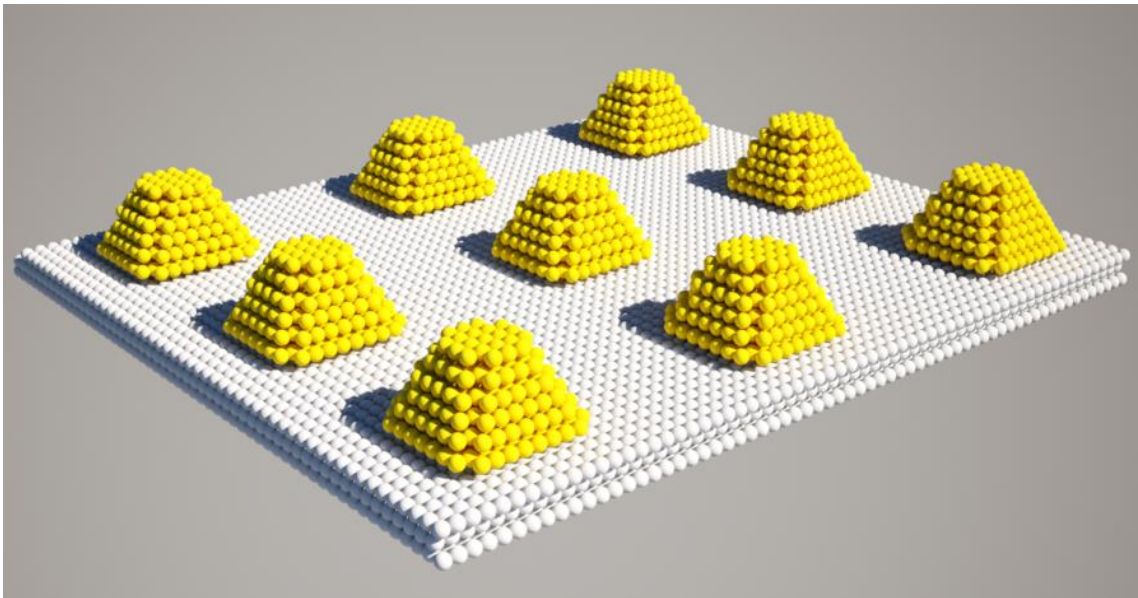
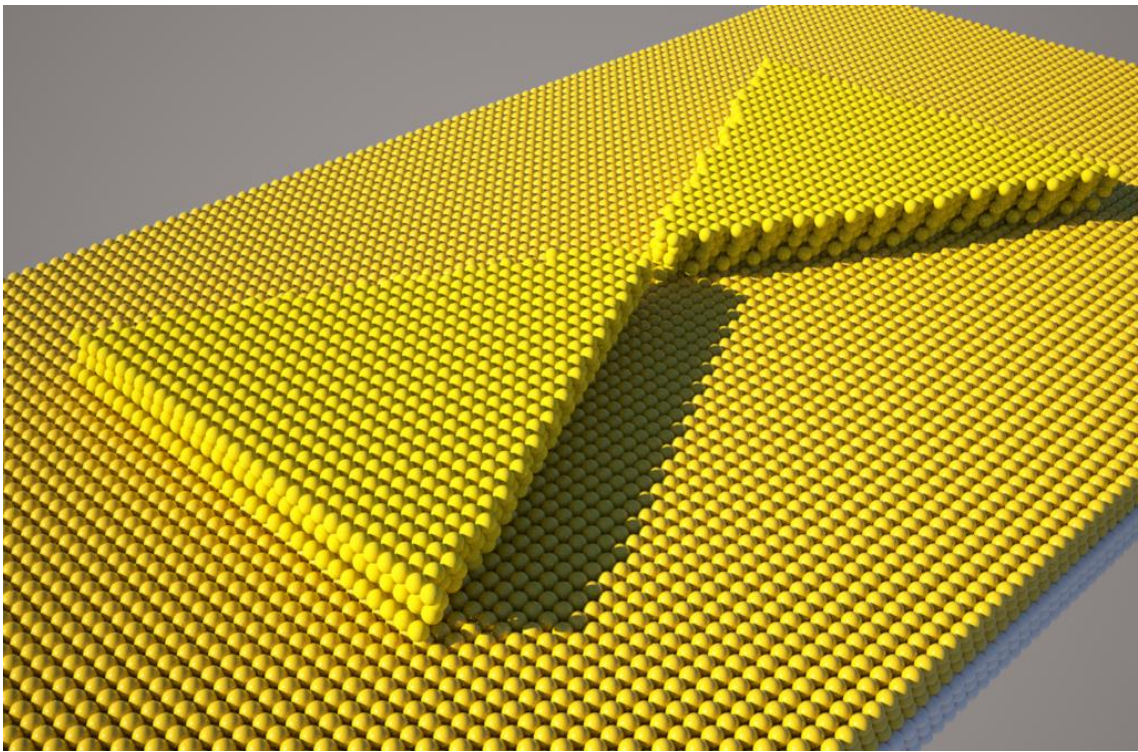
| | |
|---|-----|
| Figure 49. a) Plan view SEM image of an ordered array of shape-controlled Au nanostructures fabricated by electroless deposition and EBL patterning (see text) on a Au(100) substrate (hole diameter of 200 nm, 700 nm periodicity. b) Expanded top-view SEM of an individual single crystal pillar at 500000x magnification, showing a (100) top facet and angled (111) side facets..... | 110 |
| Figure 50. Top-view SEM images of Au grown under the influence of SO_4^{2-} at a) 0.5 M concentration and b) 0.75 M concentration. | 116 |
| Figure 51. The growth of Au under the influence of Br^- and SO_4^{2-} leads to the formation of 3-D square pyramidal surface nanostructures with primary (110) facets. Their orientation can be assigned based on the orientation that they have with respect to the edge of the Si(100) substrate which is cut along the 4-fold [110] directions. | 118 |
| Figure 52. Top-view SEM image of nano-electrode array on PMMA A4 after development with 250 nm hole diameter..... | 119 |
| Figure 53. SEM image of the sample suspended on the TEM grid, a) cross-sectional SEM of the lifted-out sample and b) SEM image of a zoomed-in region of the sample shown in a)..... | 120 |
| Figure 54. Integrating sphere nanopyr amid absorbance measurement. The SERS spectra described in the text were collected with a 785 nm excitation wavelength, the surface had demonstrated up to 20% absorption..... | 121 |
| Figure 55. a) Fabrication steps of a bowtie nano-antenna on gold, that involves FIBing away two rectangles and squares to form the basis and the sides of the triangles, b) shows the FIB mechanism for milling, c) shows the SEM images bowtie antennas made on a monocrystalline (left) and polycrystalline (right) Au film respectively..... | 125 |
| Figure 56. Yield and functionality of bowtie nano-antennas as function of film quality have been demonstrated. Simultaneous excitation of 30 bowtie nano-antennas made on a) single crystal Au film, b) multi-crystalline film..... | 127 |
| Figure 57. The effect of polarization on the activity of bowtie nano-antennas is shown. a) and b) FDTD modeled antenna for horizontally and vertically polarized excitation respectively. Monocrystalline bowtie nano-antenna (c) and d)) and polycrystalline bowtie nano-antenna (e) and f)) for horizontally and vertically polarized excitation respectively..... | 129 |
| Figure 58. Effect of film quality on bowtie nano-antenna stability. The device stability of a) monocrystalline bowtie antenna and b) polycrystalline bowtie antenna as the incident laser power is sequentially increased. Both devices were excited by a 780nm, 120 fs pulse duration laser. Percentages reflect the fraction of maximum incident laser intensity. | 133 |

| | |
|---|-----|
| Figure 59. Surface enhanced Raman spectra of benzoic acid from a) monocrystalline Au bowtie nano-antenna and b) polycrystalline Au bowtie nano-antenna, are shown and compared in c). The SERS was carried out by a Renishaw Raman microscope (785 nm). | 134 |
| Figure 60. The fabricated Au bowtie nano-antennas on a) monocrystalline Au(100) and b) thermally evaporated polycrystalline Au. | 140 |
| Figure 61. Demonstration of the healing effect of the EED process; a) and b) are the e-beam polycrystalline Au before and c) and d) are the polycrystalline Au film after EED treatment. | 144 |
| Figure 62. Au nanostructures grown on a polycrystalline Au substrate using EED process..... | 145 |
| Figure 63. a) shows the SEM image of series of Au nanopillars after material conversion, an ordered textured surface can be noticed. b) is SEM image of a clean Au nanopillar before the addition of BA. c) SEM image of an Au nanopillar after exposure. d) is the absorption data of the same array before (black) and after being coated with BA (red), collected in an integrating sphere. e) is the Raman spectrum collected from the Au nanopillar array after the exposure. | 146 |
| Figure 64. a) Cu metasurface array on Au(100) and b) is a tilt view of the same array of Cu nanostructures. | 147 |

List of Acronyms or Glossary

| | |
|--------|---|
| SPP | Surface Plasmon Polariton |
| SP | Surface Plasmon |
| FTIR | Frustrated Total Internal Reflection |
| LSP | Localized Surface Plasmon |
| NIR | Near-Infrared |
| UV | Ultraviolet |
| EBL | Electron Beam Lithography |
| FIB | Focused Ion Beam |
| DUL | Deep-UV Lithography |
| IC | Integrated Circuit |
| SEM | Scanning Electron Microscope |
| BE | Backscattered Electron |
| SE | Secondary Electron |
| EDAX | Energy Dispersion Analysis X-ray |
| TEM | Transmission Electron Microscope |
| CTEM | Conventional Transmission Electron Microscope |
| STEM | Scanning Transmission Electron Microscope |
| SAED | Selected Area Electron Diffraction |
| AFM | Atomic Force Microscope |
| STM | Scanning Tunneling Microscope |
| PR | Photo Resist |
| PHS | Polyhydroxystyrene |
| PMMA | Poly(methyl methacrylate) |
| HSQ | Hydrogen Silsesquioxane |
| PVD | Physical Vapour Deposition |
| e-Beam | Electron Beam |
| IR | Infrared |
| MPL | Multiphoton Luminescence |
| LSM | Laser Scanning Microscope |

| | |
|----------|---|
| LASIR | Advanced Spectroscopy and Imaging Research |
| UBC | University of British Columbia |
| SFU | Simon Fraser University |
| CCD | Charge-Couple Device |
| SERS | Surface-Enhanced Raman Scattering |
| FDTD | Finite-Difference Time-Domain |
| CV | Cyclic Voltammetry |
| Redox | Reduction-Oxidation |
| WE | Working Electrode |
| RF | Reference Electrode |
| DI-Water | Deionized water |
| FCC | Face Centered Cubic |
| XRD | X-ray Diffraction |
| 2PPL | Two-Photon Photoluminescence |
| CFI | Canada Foundation for Innovation |
| BCKDF | British Columbia Knowledge Development Fund |
| BOE | Buffered Oxide Etch |
| CMOS | Complementary Metal-Oxide-Semiconductor |
| SHE | Standard Hydrogen Electrode |
| EHT | Extra High Tension |
| IPA | Isopropyl Alcohol |
| EED | Epitaxial Electroless Deposition |
| BA | Benzoic Acid |
| R6G | Rhodamine 6G |
| rGO | Reduced Graphene Oxide |
| VGH | Vancouver General Hospital |



1. Introduction

With the advancement of technology, the fabrication of nanoscopic features is now achievable. Plasmonic nanostructures (nanostructures of highly conductive materials, e.g. gold, silver, graphene, etc.) have shown great potential in various applications such as sensors, photovoltaics, cancer treatment and many more. Surface plasmons, the collective oscillation of interface electrons, result from the interaction of light and matter at the interfaces of conductive materials. The plasmonic properties directly depend upon the size, shape and nature of the plasmonic materials at the nanoscale. The capability of fabricating nanoscale plasmonic materials in a variety of shapes and sizes is of great importance to researchers to create a new generation of materials with specific optical and electronic properties^{1,2}.

It is well understood that the behaviour of an excited plasmon at metal-dielectric interfaces is a function of the quality of the metallic surface and is limited by the method of metal deposition³. The existence of grain boundaries leads to scattering effects and the decoupling of photons from the surface electron plasma which reduces the intensity of the propagating wave on planar surfaces. Likewise, the existence of grain boundaries in metallic nanostructures results in rapid decoherence and decay of excited surface plasmons. Each of the nanocrystallites (grains) behaves as an individual nanostructure in which the excitation of plasmons occur at different crystalline facets. The collection of local excitations can be observed in the overall nanostructure; resulting in lower intensity, higher losses and lower mechanical stability which are important factors for devices taking advantage of surface plasmons. In chapter 3 the effect of grain boundaries on device stability is discussed further.

In order to exploit plasmonic effects in devices, it is not only necessary to control the nanoscale geometry of the plasmonic structures, but also to control their location on a surface, so they can be addressed with light or electricity. The solution phase synthesis of nanostructures has allowed chemists to create a huge array of nanostructures of well-defined size, shape and composition^{4,5}. The use of specific

chemical interactions between components of the solution and the growing nucleation centres in solution can alter the rates of chemical growth to provide shape selectivity. Preferential adsorption on certain crystal facets leads to growth kinetics that differs for these facets and provides the potential for shape control^{4,6}. The resulting structures include nanospheres, nanowires and other 3-dimensional shapes that display unique, size- and shape-dependent optical and electronic properties⁴. However, one major challenge related to this approach is that the nanostructured products of these synthetic methods are suspended in a solution [Figure 1], isolated from each other by the use of capping agents to enhance their stability and prevent their aggregation into larger structures. In this form, it is difficult to assemble, locate and address these nanostructures individually with either light or electricity, preventing them from broader use in devices⁴.

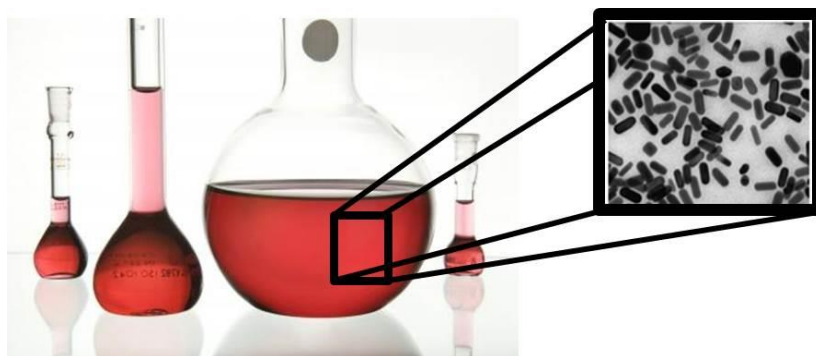


Figure 1: Gold nanorods were produced with synthetic method. The color red is due to the dispersion effect¹.

The focus of this thesis is to introduce a new and novel deposition technique to form single crystal and ultra-smooth plasmonic metallic surfaces. These films can then be used to fabricate metasurfaces and plasmonic surface nanostructures with control

¹ The images are courtesy of: “<http://www.bbisolutions.com/products/1496-diagnostic-gc-starter-pack-plus>” and “N. Khlebtsov and et al. Chem Soc. Rev., 2011”

over their crystalline orientation. The process offers a platform for deposition of both plasmonic and non-plasmonic metals and their alloys through electroless deposition chemistry. Further, this chemistry can be readily carried out in non-cleanroom conditions and coupled with various patterning methods to provide a new and cost-effective approach to the fabrication of nanostructured plasmonic-based devices.

1.1. Surface Plasmons

Surface plasmons were first described in 1908 by the German physicist Gustav Mie when he published a paper on the color effects associated with colloidal gold particles⁷. In this paper, light scattering by the spherical particles was described by Maxwell's theory and used to simulate the light-matter interactions. He managed to predict the changes of the optical response of gold as the diameter of the spherical particles was altered. The development of Mie theory to describe this phenomenon (now known more commonly as surface plasmon resonance) is the result of his work in explaining the scattering effects of electromagnetic radiation by homogeneous, isotropic spheres⁸. Rufus H. Ritchie in 1957 explains in his paper, published in "*Physical Review*", how the energy losses of the passing electrons through thin films are related to "excitation of plasma oscillations or plasmons in the sea of conduction electrons"⁹. The surface plasmon and its properties were subsequently studied extensively by H. Raether, E. Kretschmann and A. Otto, resulting in the introduction of methods for the excitation of surface plasmons optically, on smooth metallic surfaces.

Surface plasmons, which in a more complete description should be referred to as surface plasmon polaritons (SPPs), are the collective oscillation of the electrons which result from the coupling of the electromagnetic radiation with the free surface electrons that propagate at the metal-dielectric interface¹⁰ [Figure 2].

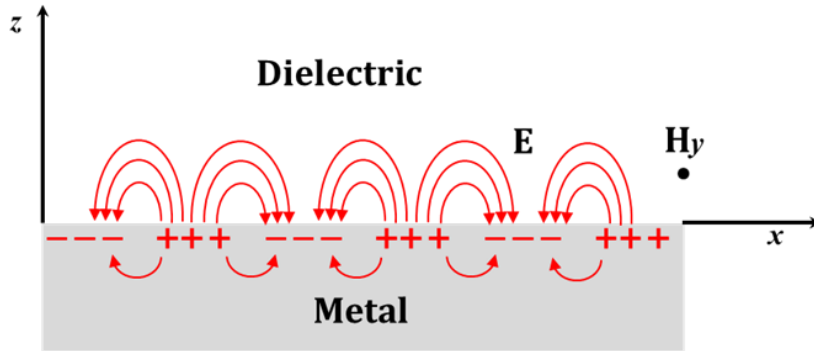


Figure 2. Schematic of the excitation of the plasmon at the metal-dielectric interface, where E represents the electric field and H_y is the magnetic field vector.

It should be noted that there is an exponential decay in the propagation intensity of the SPP along a smooth surface at a metal-dielectric interface, due to the dielectric constants of the two materials which have opposite signs^{11,12} [Figure 3]. This indicates that the SPP can only exist at the interface of a metal ($\epsilon_m < 0$) and a dielectric material where $\epsilon_d > 0$ and this condition can be shown by using the Maxwell's equations to solve for solutions that satisfy the modes for the interface.

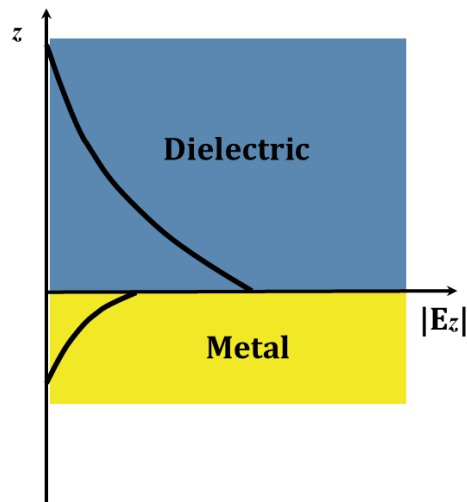


Figure 3. Decay of the SPP at the metal-dielectric interface.

Maxwell's equations show that the surface plasmons (SPs) on the surface of the metals must be polarized in such a way that their magnetic field should be parallel to the metal-dielectric interface [Figure 2]. SPs on the surface of a metallic film can be induced in two general forms:

1. By incident electrons (scattering electrons on the metal surface)
2. By photons (photon-electron coupling)

The main focus of this work is on photon-based excitation of SPs.

The boundary conditions of the generated SPs by an incoming electromagnetic wave of frequency ω can be calculated using Maxwell's equations. The resulting condition on the wavevectors is given by

$$k_{SP} = \sqrt{\frac{\varepsilon(\omega)\varepsilon_d}{\varepsilon(\omega) + \varepsilon_d}} k_0 \quad (1)$$

where the wavevectors of the SPs and the incident light are k_{SP} and k_0 respectively, the dielectric permittivity of the metal is $\varepsilon(\omega)$ and ε_d represents the permittivity of the dielectric material¹³. The wavevector of the incident light (k_0) can be obtained by dividing the frequency ω by the speed of light c :

$$k_0 = \omega/c \quad (2)$$

The dielectric constant of the metal has a magnitude and phase with respect to the incident electromagnetic field and can be written as a combination of a *real* and an *imaginary* part:

$$\varepsilon(\omega) = \varepsilon_1 + i\varepsilon_2 \quad (3)$$

where $|\varepsilon_1| \gg |\varepsilon_2|$ and from Drude theory^{11,14}, in which the electrical conduction and the movement of electron are modeled, the *real* part of the dielectric constant of the metal we can be expressed as:

$$\varepsilon_1 = 1 - \left(\frac{\omega_p}{\omega}\right)^2 \quad (4)$$

where ω_p is the bulk plasma frequency and can be defined as:

$$\omega_p = \sqrt{\left(\frac{ne^2}{\epsilon_0 m^*}\right)} \quad (5)$$

where n is the electron density, e is the electron charge, ϵ_0 is the permittivity of free space and m^* is the effective mass of electrons in the metal. Figure 4 describes the behavior of the SP's wavevector (red) and free-space photons (yellow), and illustrates that the direct illumination of the smooth metallic surfaces will not lead to excitation of SPs since k_0 and k_{SP} do not intersect each other, preventing momentum matching, necessary to excite the plasmons).

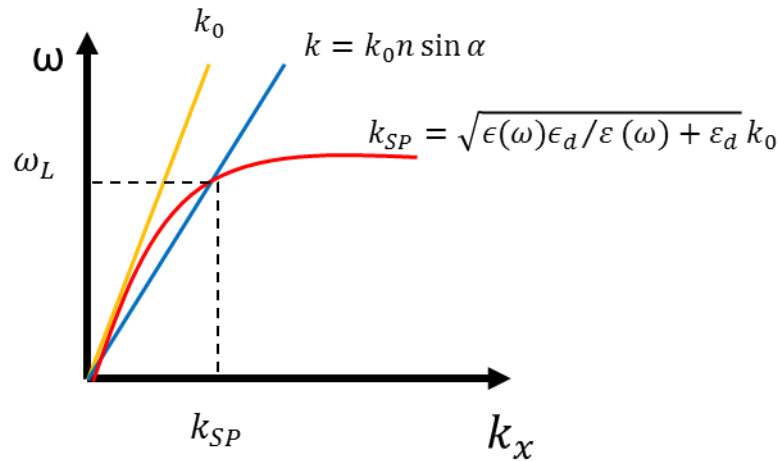


Figure 4. The diagram shows the nonlinear dispersion relation of SP's in red and the linear dispersion relation of incident photons without the prism in orange and incident photons at the total internal reflection in blue.

The wavevector of the photons directly reaching the surface of the metal is not large enough to excite the SPs and requires an indirect excitation method to couple with the surface electrons^{14,15}. Otto in 1968 showed that with help of a prism, when light undergoes total internal reflection, the wavevector becomes large enough to excite SPs [Figure 5]. The changes in the wavevector and its magnitude are shown in Figure 4. The wavevector of the photons in the Otto configuration can be calculated by:

$$k = k_0 n \sin \alpha \quad (6)$$

where the n is the index of refraction of the prism and α is the angle of incident light from normal line to the surface. From the above equation, the wavevector of the photons in the prism is greater than it is in air by factor of $n \sin \alpha$. It is important to know that at the total internal reflection there will be no light passing through the prism at the point of incidence, however the field generated by incident photons will evanescently propagate at the glass-air interface and it undergoes an exponential decay. In the Otto configuration, the prism is placed in the vicinity of the metallic film but with a small air gap between them such that there is no contact between the two surfaces. The evanescent waves generated by the photons couple through the air gap and reach the surface of the metal, inducing SPs at the metal-air interface. A schematic of the Otto's configuration for generating SPs is depicted in Figure 5.

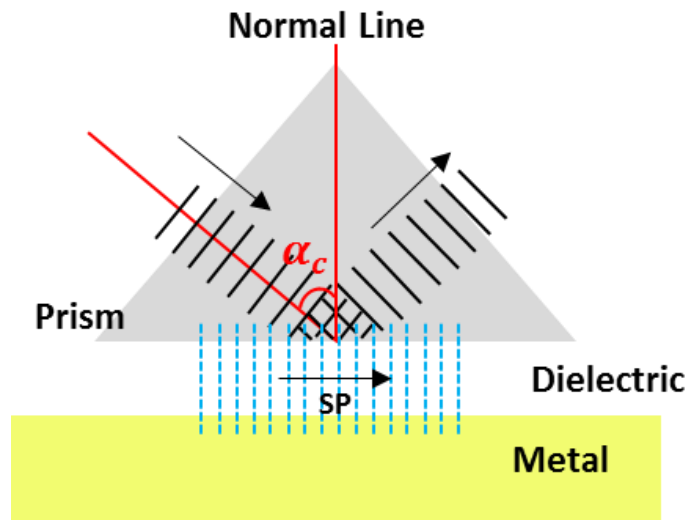


Figure 5. Schematic of Otto configuration is shown. The blue dashed lines represent the surface plasmonic wave induced evanescently by the electric field of the incident photons which have undergone total internal reflection in the prism.

In order to generate SPs using the Otto configuration, the air gap should be between 100-200 nm, which is difficult to achieve without the proper tools and setup. As an alternative, E. Kretschmann proposed a configuration in which the air gap was removed. Instead Kretschmann deposited metal on the surface of the prism and through total internal reflection, SPPs are generated at the metal-air interface [Figure 6]. Despite the fact that in both the Kretschmann and Otto configurations, the incident light in the prism undergoes total internal reflection, the mechanism with which the SPP is

generated is quite different. As mentioned, in the Otto approach, the extension of the electric field of the incident photons causes the generation of SPs, while in the Kretschmann's configuration it is a phenomenon known as frustrated total internal reflection (FTIR) which is analogous to quantum tunnelling where, instead of quantum particles (i.e. electrons), photons that form evanescent waves at the point of reflection in the prism extend into the metal. In the case of a thin metallic film, these evanescent waves can reach the metal-air interface and propagate as SPs at the metal-air interface¹⁴.

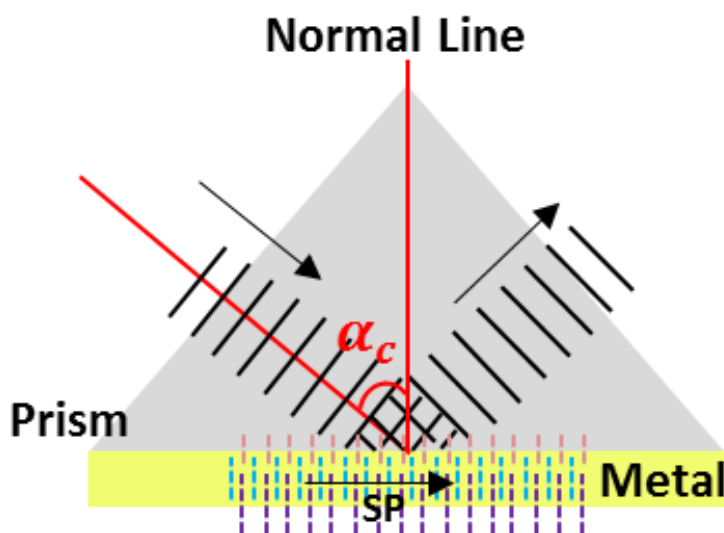


Figure 6. Kretschmann configuration is shown. The evanescent waves generated by the incident photons at the point of reflection in the prism can reach to the other side of a thin metal film and propagate as SPs at the metal-air interface.

1.2. Localized Surface Plasmons

The non-propagating modes of SPs are known as localized surface plasmons (LSPs) which occur on metallic nanoparticles or in nanostructured metal surfaces. LSPs are induced by the coupling of electromagnetic radiation with the plasma of the conduction electrons resulting in a localized and non-propagating excitation mode^{11,16}. Such electronic excitations on nanoparticles results in amplification of the field both

inside and outside (in the near-field zone) of the particles. Direct illumination of nanostructures can lead to excitation of LSPs, unlike the propagating mode (SPPs), for which phase-matching techniques are required in order to achieve wavevectors large enough to couple with the surface electrons. Figure 7 illustrates a nanoparticle being influenced by electromagnetic radiation and how the electric field distribution in the nanoparticle changes with respect to changes in the direction of the electric field of the electromagnetic wave.

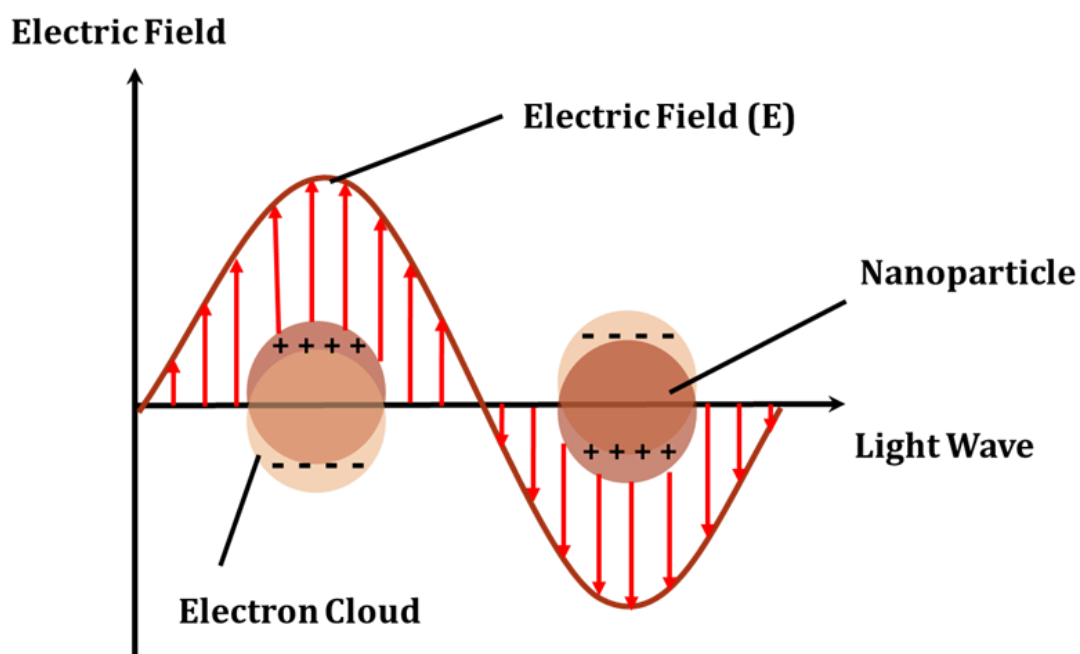


Figure 7. Schematic of the excitation of localized surface plasmons in nanoparticles is shown. This non-propagating plasmonic mode occurs in nanoparticles in the presence of electromagnetic waves.

Metallic nanoparticles with sizes smaller than the wavelength of light exhibit strong dipolar excitation in the form of LSPs. The shape of the metallic nanosized particles also plays an important role in the intensity of the generated localized field and the plasmonic response resulting from illumination by a particular wavelength. The plasmonic field intensity and the frequency of the resonance of the LSPs are highly

dependent upon the dielectric properties of the metal and the medium in which the particles exist^{10,17}.

The spectral region in which the nanoparticles exhibit the plasmonic response also depends on the type and the dielectric constant of the constituent metal. For instance, gold and silver nanoparticles have a resonance response in the visible portion of the electromagnetic spectrum. The plasmonic response of gold ranges from the near-infrared (NIR) region to ~530 nm while LSPs in silver nanoparticles can be excited even in the ultraviolet (UV) region of spectrum.

As mentioned, the LSPs are the result of the resonance caused by coupling of an incident light beam with the oscillating valence electrons of the metal. This resonant condition occurs only when the natural oscillating frequency of the valence electrons matches the frequency of the incident electromagnetic radiation. As a result of this resonance condition, the nanoparticles will often exhibit bright colors in transmission and reflection due to the resonant absorption and scattering effects respectively. The spatial field distribution can be calculated where from the Laplace equation for the potential, we have $\nabla^2\phi = 0$ and thus the electric field will be $E = -\nabla\phi$. The potential inside and outside of the spherical nanoparticle can be presented as¹¹:

$$\Phi_{in} = -\frac{3\varepsilon_m}{\varepsilon_{NP} + 2\varepsilon_m} E_0 r \cos \theta \quad (7)$$

$$\Phi_{out} = -E_0 r \cos \theta + \frac{\varepsilon_{NP} - \varepsilon_m}{\varepsilon_{NP} + 2\varepsilon_m} E_0 \left(\frac{d}{2}\right)^3 \frac{\cos \theta}{r^2} \quad (8)$$

where E_0 is the amplitude of the electric field, ε_{NP} and ε_m are the dielectric permittivity of the nanoparticle and of the medium (surrounding the nanoparticle) respectively. It should be noted that both dielectric constants are functions of the excitation frequency ω , and r is the position vector which creates the angle θ with the surface normal. The Φ_{out} is the superposition of the central dipole of the nanoparticle and the applied field that induces the dipole moment within the sphere. By including the dipole moment P to equation (8) it can be rewritten as:

$$\Phi_{out} = -E_0 r \cos \theta + \frac{P \cdot r}{4\pi\epsilon_0\epsilon_m r^3} \quad (9)$$

and P is defined as:

$$P = 4\pi\epsilon_0\epsilon_m a^3 \frac{\epsilon_{NP} - \epsilon_m}{\epsilon_{NP} + 2\epsilon_m} E_0 \quad (10)$$

From equation (10), where at the boundary condition $r = a$, we can see that there is a dipole moment inside the sphere of magnitude proportional to $|E_0|$ which has been induced by the applied field. The polarizability α of a spherical nanoparticle with sub-wavelength diameter under the influence of the electromagnetic radiation is:

$$\alpha = 4\pi a^3 \frac{\epsilon_{NP} - \epsilon_m}{\epsilon_{NP} + 2\epsilon_m} \quad (11)$$

therefore, P can be rewritten as:

$$P = \epsilon_0\epsilon_m \alpha E_0 \quad (12)$$

The polarizability will undergo a resonant enhancement when the $|\epsilon_{NP} + 2\epsilon_m|$ becomes a minimum in the equation (11).

It should be noted that excitation of SPs is a band limited phenomenon due to the negative values of the permittivity in metals. Therefore, excitation of SPs in different metals requires different wavelengths¹⁸; i.e. in gold, wavelengths below 530 nm cannot excite SP modes. To achieve the polarization enhancement, the real part of the permittivity of the nanoparticles must reach the value of -2 and that occurs when the imaginary part of the permittivity has little or no variation with frequency. This is known as the Fröhlich condition and can be shown as:

$$Re[\epsilon(\omega)_{NP}] = -2\epsilon_m \quad (13)$$

In order to satisfy the Fröhlich condition for the spherical nanoparticles located in the air we have:

$$\omega_0 = \frac{\omega_p}{\sqrt{3}} \quad (14)$$

where ω_0 and ω_p are frequency of the SP and the frequency of the electron plasma respectively. Equation 13 shows the strong dependency of the LSPs on the dielectric constant of the medium with which the nanoparticle is surrounded; i.e. there will be a shift towards the red end of spectrum as the value of the dielectric constant of the environment (ϵ_m) increases, and that is an important property of LSPs that is being investigated widely for sensing applications^{11,15}.

The electric field inside and outside of the sphere can be expressed by:

$$E_{in} = \frac{3\epsilon_m}{\epsilon_{NP} + 2\epsilon_m} E_0 \quad (15)$$

$$E_{out} = E_0 + \frac{3n(n.P) - P}{4\pi\epsilon_0\epsilon_m} \left(\frac{1}{r}\right)^3 \quad (16)$$

where P is the dipole moment shown in equation (12). Equations (15) and (16) describe the distribution of the electric field $E = -\nabla\phi$ and they indicate that a resonance in polarization α (eq. 11) is a resonance enhancement in the internal and dipole fields.

Up to this point, all discussion has been related to spherical metallic nanoparticles. However, it has been shown experimentally by many groups that the shape and the size of the nanoparticles play an important role in its plasmonic response^{17,19}. In a spherical particle, the dimension of the particle is the same along all three axes, but changing the symmetry of the particle can change the dimension along one or more of the axes. Thus, any changes to this ratio will be followed by the changes in the ratio of the dipole moment and therefore the excitation of LSP in different directions will result in different optical responses which at some cases can be visually noticed through the scattered, absorbed or the emitted light. Furthermore, if the polarization occurs along the shorter axis (transverse mode) the plasmonic resonance

will have a slight blue-shift in its optical response with respect to the spherical particle. Polarization of the incident electric field along the longer axis (longitudinal mode) will result in a red-shifted plasmonic resonance with respect to the spherical particle [Figure 8].

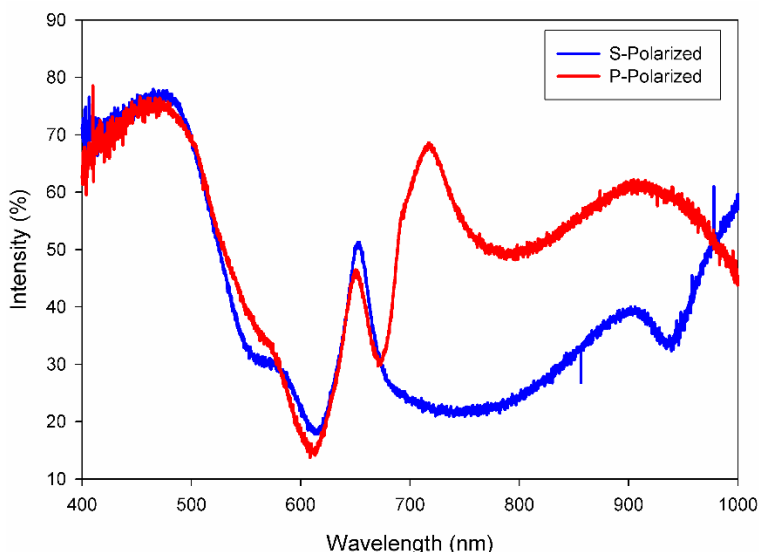


Figure 8. Polarized Optical response of a gold nanopillar array measured in an integrating sphere with incident angle at 20°.

These shape-dependent characteristics can be taken advantage of to create selective optically sensitive response for photonic devices, sensors, photonic and quantum circuits, and energy harvesting devices. For these reasons the area of plasmonics offers a promising and bright future; however, many challenges remain. One major hurdle that must be overcome relates to the fabrication and patterning of highly crystalline plasmonic structures that lack grain boundaries. SPP-based devices require ultra-smooth or single crystalline thin film surfaces for optimal performance, which are difficult and expensive to prepare. As for the non-propagative mode of SPs (LSP), the fabrication of nanostructures with specific shapes and geometry is required. Through advancements in nanotechnology, the fabrication of many nanosized structures have been enabled and the result of such technological improvements can be seen in the devices that have become an important part of our day to day lives, such as smart phones and computers. Even though the ability of current nanofabrication tools is sophisticated, the capability of existing infrastructure to create nanostructures with

complex geometries is still limited. Tools such as electron beam lithography (EBL), focused ion beam (FIB), deep-UV lithography (DUL) systems which are widely used by the integrated circuit (IC) industry might be able to address this challenge up to certain level, but the cost and time required to use these tools make these approaches a significant challenge. In the next section a brief overview of the commonly used nanofabrication methods for creating nanostructured surfaces as well as characterization and modeling techniques used in this work will be presented.

References

1. Mock, M. & Mock, J. J. Shape effects in plasmon resonance of individual colloidal silver nanoparticles. *J. Chem. Phys.* **116**, 6755–6759 (2002).
2. Zhang, A.-Q., Qian, D.-J. & Chen, M. Simulated optical properties of noble metallic nanopolyhedra with different shapes and structures. *Eur. Phys. J. D* **67**, 231 (2013).
3. Yallup, K. & Basiricò, L. *Sensors for Diagnostics and Monitoring*. (CRC Press, 2018).
4. Xia, Y., Xiong, Y., Lim, B. & Skrabalak, S. E. Shape-Controlled Synthesis of Metal Nanocrystals: Simple Chemistry Meets Complex Physics? *Angew. Chem. Int. Ed.* **48**, 60–103 (2009).
5. Wiley, W. & Wiley, B. Maneuvering the surface plasmon resonance of silver nanostructures through shape-controlled synthesis. *J. Phys. Chem. B* **110**, 15666–15675 (2006).
6. Choi, C. & Choi, K. S. Shape control of inorganic materials via electrodeposition. *Dalton Trans.* 5432–5438 (2008).
7. Mie, G. Beiträge zur Optik trüber Medien, speziell kolloidaler Metallösungen. *Ann. Phys.* **330**, 377–445 (1908).
8. Hergert, W. Gustav Mie: From Electromagnetic Scattering to an Electromagnetic View of Matter. in *The Mie Theory* 1–51 (Springer, Berlin, Heidelberg, 2012). doi:10.1007/978-3-642-28738-1_1
9. Ritchie, R. H. Plasma Losses by Fast Electrons in Thin Films. *Phys. Rev.* **106**, 874–881 (1957).
10. Maier, S. A. & Atwater, H. A. Plasmonics: Localization and guiding of electromagnetic energy in metal/dielectric structures. *J. Appl. Phys.* **98**, 011101 (2005).

11. Maier, S. A., *Plasmonics: Fundamentals and Applications* Springer.
12. Raether H., *Surface Plasmons on Smooth and Rough Surfaces and on Gratings* || Springer.
13. Barnes, W. L., Dereux, A. & Ebbesen, T. W. Surface plasmon subwavelength optics. *Nature* (2003). doi:10.1038/nature01937
14. Kretschmann, E. & Raether, H. Notizen: Radiative Decay of Non Radiative Surface Plasmons Excited by Light. *Z. Für Naturforschung A* **23**, 2135–2136 (2014).
15. Zhang, J., Zhang, L. & Xu, W. Surface plasmon polaritons: physics and applications. *J. Phys. Appl. Phys.* **45**, 113001 (2012).
16. Kik, P. G. & Brongersma, M. L. Surface Plasmon Nanophotonics. in *Surface Plasmon Nanophotonics* 1–9 (Springer, Dordrecht, 2007). doi:10.1007/978-1-4020-4333-8_1
17. Link, S. & El-Sayed, M. A. Shape and size dependence of radiative, non-radiative and photothermal properties of gold nanocrystals. *Int. Rev. Phys. Chem.* **19**, 409–453 (2000).
18. Sihvola, A. H. Character of Surface Plasmons in Layered Spherical Structures. *Prog. Electromagn. Res.* **62**, 317–331 (2006).
19. Mock, J. J., Barbic, M., Smith, D. R., Schultz, D. A. & Schultz, S. Shape effects in plasmon resonance of individual colloidal silver nanoparticles. *J. Chem. Phys.* **116**, 6755–6759 (2002).

2. Experimental Methods

2.1. X-Ray Diffraction Analysis

The X-ray region is part of the electromagnetic radiation spectrum with wavelengths ranging from 0.01 nm up to 10 nm^{1,2}. The short wavelength of X-rays has allowed this spectral range to be useful for non-destructive crystallographic analysis where information about the crystalline lattices and orientations of different crystal planes of materials can be learned³. Incident X-ray waves can be diffracted by atomic planes which leads to formation of fringes that define the orientations in which the atoms are packed^{1,2,4}. The crystalline planes are defined by convention with Miller Indices [hkl] which describe the lattice direction for different atomic orientation in three dimensions (3D)². In solids, the X-ray waves get diffracted by parallel planes of atoms within the crystal which are spaced equally. This interatomic plane distance, also known as d-spacing, is different for each crystalline direction, and can be calculated with respect to the angle at which the X-ray is diffracted using the Bragg's law^{2,4}:

$$\lambda = 2d_{hkl} \sin \theta \quad (17)$$

in which λ is the X-ray wavelength, d is the space between the crystalline planes and θ is the angle of incident. The d-spacing is related to the Miller indices by⁴:

$$d_{hkl} = \frac{a_0}{\sqrt{h^2 + k^2 + l^2}} \quad (18)$$

where the a_0 is the lattice constant which defines the physical dimensions within the unit cell. Figure 9 illustrates the X-ray diffraction process caused by crystal planes.

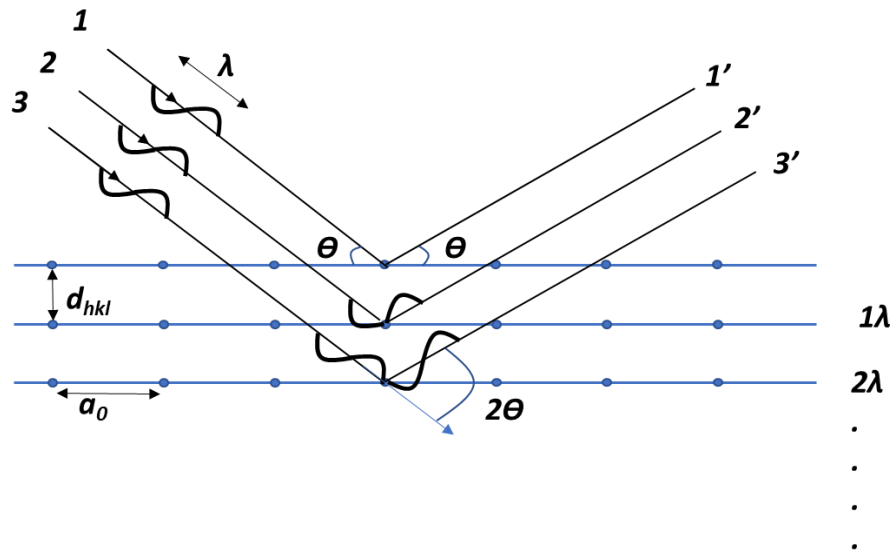


Figure 9. Illustration of X-ray diffraction by crystalline planes of a solid crystal.

This approach in identifying different crystalline lattices and crystalline directions is used in a tool known as an X-ray diffractometer, where the diffraction from powders or larger crystal pieces is collected as a function of incident (Θ) and diffracted (2Θ) angles. The diffracted X-ray intensity is digitally processed and displayed as peaks which can be used as a method to define elements and compounds. In conventional X-ray diffractometers, point detectors collect X-rays scattered along a detection circle (which is the axis over which the detector scans) and ignore X-rays scattered away from this axis. However, with a large area two-dimensional detector, the collection of scattered X-rays over many angles is enabled, providing more information about the sample under study. The two-dimensional (2D) XRD patterns of single crystal materials appear as single diffraction spots. These spots include the diffraction contributions of crystalline planes with the same crystalline orientation that form constructive interference at only specific regions of the detector. In contrast, polycrystalline materials comprised of many crystallites oriented in different directions diffract X-rays in multiple directions and result in collected diffraction patterns that appear as diffraction rings (or arcs) for different crystalline lattices⁵.

In this thesis work, X-ray diffraction was used to analyze metallic crystals and their atomic plane orientations. The source of the X-rays in the diffractometer used for this work is copper (Cu) with 1.54 Å wavelength. The X-ray diffractometer is a product of

Rigaku, model Rapid Axis, that is capable of detecting 2D X-ray diffraction. This tool is housed in 4D LABS facility at Simon Fraser University and is ideal for rapid analysis of crystalline structures [Figure 10].



Figure 10. The 2D X-ray diffractometer manufactured by Rigaku² which is located in 4D LABS facility located at Simon Fraser University.

2.2. Scanning Electron Microscopy

The synthesis and fabrication of nano-scaled materials and structures have been enabled with advanced technology. The ability to characterize and image the miniaturized features depends directly upon the wavelength of light and particles with which the surface is scanned. Photons in the visible spectral range, used in optical microscopes, have wavelengths that can be used to image features which are hundreds

² <https://users.4D LABS.ca/tools/xrd1.html>

of nanometers to a micron in size, however smaller structures will meet the diffraction limit of such instruments. With the recognition of the wave characteristics of quantum particles, physicists in the late 1920s and early 1930s managed to demonstrate the ability to image nanoscopic features with electrons. These initial investigations led to the development of the modern-day scanning electron microscope (SEM) which is now one of the well-recognized and most widely used tools for surface characterization of materials⁶.

The scanning electron microscope takes advantage of electrons scattering from a surface. By collecting and amplifying the signal from backscattered electrons (BEs) and/or secondary electrons (SEs), an image containing detailed information about the morphology and characteristics of the material can be obtained^{6,7}. The quality of the image acquired by the microscope depends on the mechanism of interaction between the incident electrons and the materials under investigation, as this determines the energies of the electrons that are collected by the detector. There are two main scattering types caused by interaction between the electrons and the target material⁷:

- Elastic scattering
- Inelastic scattering

In elastic scattering, the electrons are collected after deflecting from the outer-shell electrons or the nuclei of the sample, and this process often results in incident electrons that are scattered in a wide-angle with negligible loss of energy^{6,7}. The collected electrons can provide a high-resolution image of the sample which can be used to characterize the surface morphology. Inelastic scattering is caused by energy transfer of the incident electrons to the sample material. Lower energy, secondary electrons that scatter from the sample surface can be collected to yield images with resolutions as high as 1 nm.⁷ If the result of the inelastic scattering is ejection of electrons from an inner atomic orbital, this will lead to formation of a hole in that orbital and will be followed by decay of an electron from an outer shell. The electron-hole recombination will lead to emission of X-ray photons. This mechanism can be used to further characterize the sample at the chemical level and identify the chemical composition of the specimen. This technique is called energy dispersive X-ray analysis (EDAX) which is a standard add-on capability in most electron microscopes^{6,7}.

A typical SEM consists of an electron gun where the electrons are produced by heating a tungsten filament with a sharp tip. The generated electrons then are guided towards the anode which is a negatively charged component that accelerates the electron beam towards the magnetic lenses through which the electrons can be focused. The magnetic field of the scanning coil causes the electron beam to deflect and this enables the surface of the specimen to be raster-scanned where the BE or SE signals are collected with the help of designated detectors⁶. Figure 11 illustrates components of an electron microscope.

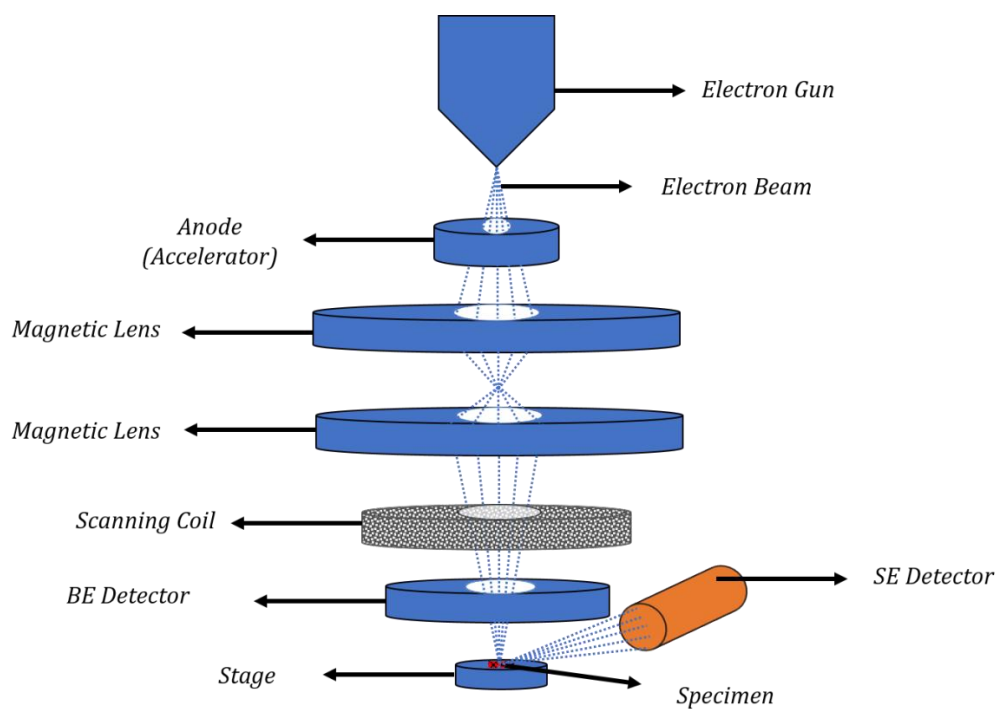


Figure 11. Schematic of a scanning electron microscope. Different components of the electron microscope are shown in this figure.

In this thesis work, electron microscopy was used as a comprehensive method to study the surface quality and chemical composition of the deposited materials, the shape and size of the nanostructures and the nano-scale devices. The FEI Helios NanoLab 650 SEM/FIB (dual electron beam and ion beam microscope) and the FEI

Nova NanoSEM 430 SEM [Figure 12a and 12b], both housed in 4D LABS at SFU, were used to acquire electron microscope images provided in this thesis.

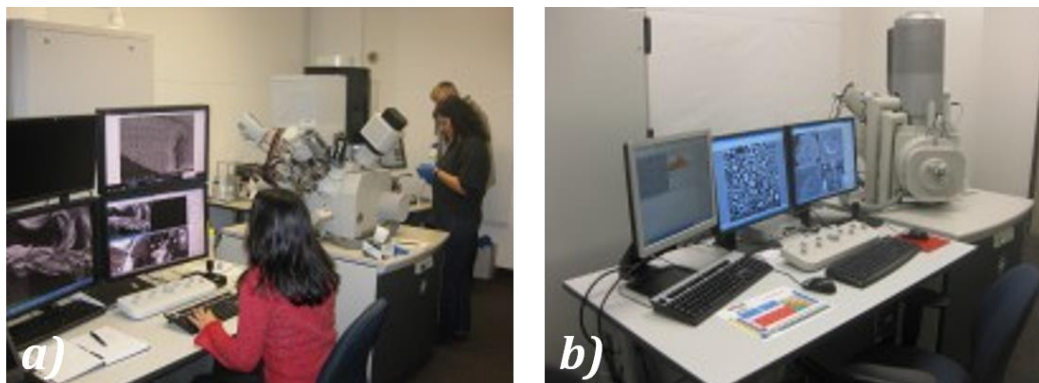


Figure 12. Electron Microscopes located in 4D LABS, a) FEI Helios NanoLab 650³ and b) NanoSEM 430⁴.

2.3. Transmission Electron Microscopy

Transmission electron microscopy (TEM) is a powerful tool to obtain information about the atomic level packing of atoms in materials, at the interfaces between materials, the presence of defects, and even the composition of materials⁸. Similar to SEM, TEM also uses a beam of electrons. However rather than scanning the surface, the generated beam of high energy electrons is transmitting through the sample. TEM was presented initially by Max Knoll and Ernst Ruska in 1931 but it did not become commercially available until 1939 when Siemens developed the first TEM with a resolution superior to any optical microscope that existed at the time⁸. The advantage of electrons to photons (in the visible range) is the smaller wavelength of high energy electrons with which much smaller features can be visualized. The wavelengths of electrons used in transmission electron microscopes usually varies between 0.004-0.00087 nm, depending directly on the acceleration voltage used in the TEM^{8,9}. The

³ <https://users.4D LABS.ca/tools/sem1.html>

⁴ <https://users.4D LABS.ca/tools/sem2.html>

relationship between the wavelength of electrons and the acceleration voltage is shown in equation 19:

$$\lambda_{el} = \frac{h}{\sqrt{2m_0eE\left(\frac{eE}{2m_0c^2}\right)}} \quad (19)$$

where h is plank's constant, m_0 is the rest mass of the electron, e is the charge of the electron, E is the acceleration voltage in volts and m_0c^2 is the rest energy^{8,9}. In general, there are two main classes of imaging considered for the transmission electron microscopy:

1. Conventional TEM (CTEM)
2. Scanning TEM (STEM)

CTEM is based on a stationary beam of electrons passing through an electron transparent sample film, which is the technique originally developed for this type of microscopy. On the other hand, in STEM, a focused beam of electrons scans the electron transparent specimen, which allows for a selective detection and more detailed imaging (mapping) of the sample³.

Electron transparency is one of the main requirements for TEM imaging which is the direct measure of the material thickness⁹. Depending on the type of material, the thickness can vary between approximately 20 nm to 100 nm to achieve sufficient electron transparency^{3,8}. Maintaining such a range of thicknesses of specimen for TEM imaging often requires sophisticated techniques involving specialized tools and skilled personnel, and can take up to several hours of sample preparation. TEM analysis of the specimens in this thesis involved sample preparation processes known broadly as "lift-out", where a small piece of material is removed from a larger sample by focussed ion beam milling and mounted on a TEM grid support. A detailed description of the process is presented in Appendix A.

The electrons that are transmitted through the specimen can undergo electron diffraction and this can be used to obtain additional information about the arrangement of the atoms in the sample (crystallography). By using the selected area electron diffraction (SAED) mode on the TEM, the diffraction of the transmitted beam of electrons

can be mapped onto the detector which leads to the ability to obtain the reciprocal lattice of the crystalline structures^{3,8}. The crystalline structure of solids can be viewed as acting as a diffraction grating, where the symmetry and direction of different crystalline planes can be realized⁸.

Analysis of material composition can also be performed with a TEM. The technique is based on EDAX where the emitted X-ray (like SEM) is collected, and based on the wavelength of the detected X-ray photons, the materials can be identified³. Specimens composed of different elements (or composed of stacked films) can be analyzed and different colors are assigned to the detected species. An elemental map (colored image) of the specimen is then generated that represents the abundance of elements in the specimen³.

The FEI Tecnai Osiris STEM housed in 4D LABS was the system used for transmission electron microscopy work described in this thesis [Figure 13].

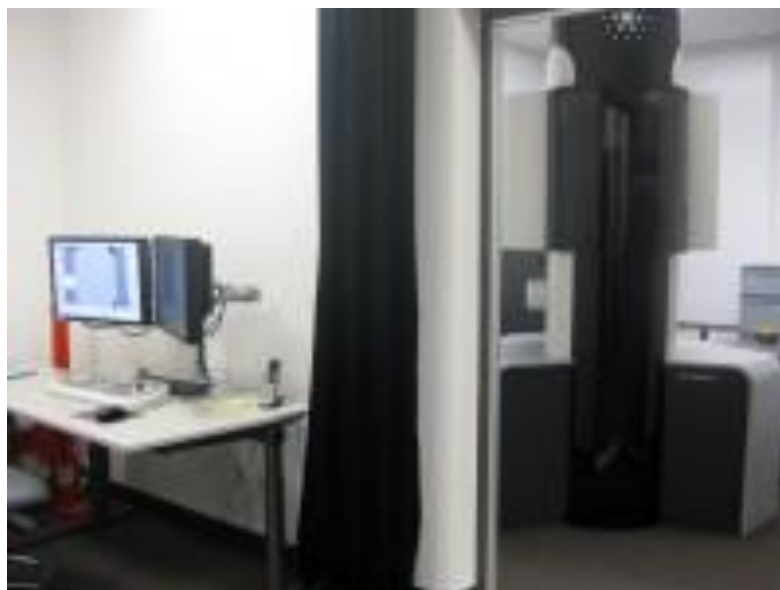


Figure 13. The FEI Tecnai Osiris STEM system located in the center of soft materials (CSM) of 4D LABS facility ⁵.

2.4. Atomic Force Microscopy

Atomic force microscopy (AFM) is an imaging method capable of providing surface information about a sample with nanometer-scale resolution^{10,11}. The idea of using force to gather topographic information from a surface came after the invention of the scanning tunneling microscope (STM), where the surface information was gathered through scanning a conductive sample by electrons tunneling through a barrier into the specimen^{11,12}. In the late 1980's Gerd Binnig, who was one of the inventors of STM, introduced the idea of mapping the surface with forces smaller than those of interatomic bonds, so that the process would not result in displacement of the atoms¹¹. To be able to calculate the required forces, the vibrational frequencies of molecules, typically $\geq 10^{13}$ Hz¹¹, need to be considered. By using atomic masses and typical vibrational

⁵ <https://users.4D LABS.ca/tools/stem1.html>

frequencies, the spring constant of atomic bonds can be calculated ($\omega^2 m$, where m is the mass of an atom) to be on the order of 10 N/m. Therefore, by applying forces smaller than the interatomic interactions, collecting detailed information about a surface can be achieved. Following the work of Christoph Greber, Calvin Quate and Gerd Binnig on the concept of imaging a surface by applying small forces onto the materials, the first AFM became available commercially in 1989^{11,12}. The advantage that AFM provides, compared to STM, is its ability to scan the surface of both conductive and nonconductive materials (as opposed to STM which requires a conductive surface), and soon this became a widely used microscopy technique for obtaining atomic resolution of variety of materials. A typical AFM consists of:

- A cantilever with sharp tip
- A sensing mechanism to detect the deflection of the cantilever upon scanning
- A feedback control system to monitor the force applied to the surface
- A mechanism to enable two dimensional scanning
- A data interpretation system to display the surface information

The cantilevers in today's AFMs are often made of silicon, silicon dioxide or silicon nitrides, and are made using microfabrication techniques. The tip of these cantilevers typically is 1 μm in diameter and 100 μm long with spring constants ranging from 0.1 N/m to 1.0 N/m and resonant frequencies in the range of 10-100 kHz^{11,12}. Scanning a surface using a cantilever can only provide a 2D image with no detail about the roughness of the surface, therefore to obtain such insights, the deflections of the tip of the cantilever needs to be measured. Most AFMs use an optical detection mechanism, typically using laser interferometry or optical deflection, and are capable of measuring the displacement of the tip with 0.1 \AA resolution¹⁰⁻¹². Scanning a surface in an AFM is done by mechanical movement of the tip in the x , y and z axes and is controlled with piezoelectric elements. These actuators provide excellent resolution but have a limited range of motion, restricting scan areas.¹² Like STM, atomic resolution can also be achieved using an AFM, however, this tool is highly sensitive to environmental disturbances and external vibrations which can interfere with the frequency of motion of the tip and its interaction with surface of the sample,

compromising its spatial resolution. For this reason, AFMs are sometimes housed in highly isolated environments to ensure atomic resolution topography can be achieved^{11,12}.

Typically, there are two different modes of atomic force microscopy which are based on the way that the tip interacts with the surface:

- Contact mode
- Oscillating mode

One of the main differences between these two modes is in the shape of the cantilevers and the type of materials that they are made of. The contact mode cantilevers have “V” shape profiles and are commonly made of silicon or silicon oxide, whereas the oscillating mode (also known as tapping mode) cantilevers have high aspect ratios with sharper tips and are often made of silicon¹². Another main difference between these two modes of atomic force microscopy is in the way the tip interacts with the surface. In contact mode, the cantilever scans the surface while maintaining a constant (set point) interaction force with the surface, while in oscillating mode, the tip vibrates at its resonance frequency and as the tip gets closer to the surface, the force field from the sample dampens the frequency and amplitude of its oscillation. This information can be monitored by the feedback control system of the microscope and translates into information about surface topography^{10,12}. In this thesis, the AFM images were obtained using a NaioAFM, manufactured by Nanosurf, in contact mode [Figure 14].



Figure 14. An NaioAFM AFM, which was used to measure surface roughness in this thesis work.

2.5. Electron Beam Lithography

The development of microelectronic devices was directly connected to fabrication techniques with which these micro-scale features were made. One of the commonly used processes, was the use of light sensitive polymers, also referred to as photo resist (PR), where the PR is exposed to light that can alter its local solubility. Illuminating a PR in a patterned way, through a mask for example, can result in regions of the PR with altered solubility, allowing for development of the photo resist in suitable solvents to yield a patterned substrate. This fabrication process is known as optical lithography and the size of the features that can be achieved is ultimately limited by the wavelength dependent diffraction limit of the light employed in the patterning step. In order to achieve nanoscopic size scale patterns, high energy electrons with much smaller wavelengths were employed. Electrons were first used to observe features beyond the capability of optical microscopes in the early 1930s, however it took more than 30 years for scientists and engineers to utilize electrons for the fabrication of nano-

scale structures via electron beam lithography¹³. The implementation is similar to that of SEM, but a more specialized lens system is required for focusing the beam of electrons on the surface while scanning the surface and controlling precisely the exposed regions^{13,14}. Another hurdle was to develop resist materials which are sensitive to electrons and mimic the effect that photons have on PRs, and that led to development of new class of resists sensitive to electrons¹³. The types of materials used as electron beam resists are sometimes polyhydroxystyrene (PHS) based polymers which are also used in the deep UV (285 nm) lithography process¹³. The resolution of electron beam lithography (EBL) is directly related to characteristics of the electron sensitive resists, where the interaction of electrons results in either breaking chemical bonds (positive resist) causing the exposed region to become more soluble, or polymerization of the material (negative resist) which leads to molecules to cross-link, making the exposed region insoluble¹³. It should be noted that the both mechanisms are possible upon electron beam bombardment, depending on the energies and doses required for inducing those effects in the resist¹³.

The most commonly used resist for EBL, is poly(methyl methacrylate) (PMMA) which is a positive tone organic resist developed in the 1960s. This polymer has a high sensitivity to electrons and lithography of features under 10 nm have been achieved, however the low etch resistance of this film has been one of the major drawbacks in use of this material in nanofabrication¹³⁻¹⁶. Hydrogen silsesquioxane (HSQ) is an example of a negative tone electron sensitive resist capable of sub-10 nm feature size resolution. First developed as a dielectric material, HSQ was found to be sensitive to electrons and was employed as an EBL resist in the late 1990s¹³. Electron beam induced chemical changes in resists provide patterning in the development process, in which the films are submerged in a chemical solution and the exposed areas, in the case of a positive resist such as PMMA, will be dissolved in the bath, leaving the rest of the film intact. The development of negative resists will cause the unexposed regions to be dissolved and the exposed regions will remain^{13,16}.

The thickness of the resist also plays an important role in the features that are made through lithography. The electron beam resist is often deposited on the sample by spin-coating to achieve a uniform coverage across the surface, and the viscosity of the resist material is one of the defining factors under which the minimum thickness can be

reached. The thicker the resist, the more energy that is required for a successful exposure of the film, affecting the speed of lithography (more exposure time) and the feature sizes^{14,15}.

The nanofabrication processes used in this thesis involved the use of PMMA resist with different thicknesses. As mentioned, thickness is based on the viscosity of the polymer and they are commercially categorized as PMMA A2 (lower viscosity) for thinner films and PMMA A4 (higher viscosity) to achieve thicker films. The doses used for exposing the PMMA film were developed and optimized specifically matching the thickness of the film and to achieve the smallest feature size possible with respect to the resist type when required. The fabrication processes also involved development of some additional steps, such as the duration under which the film was soft baked (prior to exposure) and hard baked (after development), which are not part of standard procedure for the use of PMMA. The EBL tool used for nanofabrication is a Raith e_LiNE EBL system capable of creating 20 nm features, located in the 4D LABS clean room facility [Figure 15]



Figure 15. The e_LiNE EBL system in 4D LABS clean room facility⁶.

⁶ <https://users.4D LABS.ca/tools/ebl.html>

2.6. Focused Ion Beam

The use of ions in manufacturing of microelectronic devices was a well-known process and widely implemented as early as the 1950s, yet the first specialized tool capable of focusing beams of ions and enabling direct write and fabrication of nano/micro features was not made until 1975¹³. Most ion milling/etching machines made use of Argon (Ar) plasma sources and redirected the ionized gas particles produced in one region towards the material housed in a separate part of the instrument with the help of electric fields. Surface milling was achieved by bombarding the surface with ions to induce mechanical etching of the surface. This process is still a standard technique in the field of micro/nanofabrication and known as dry etching¹³. To be able to use a focussed ion beam for direct milling, a high current density (of order A/cm^2) is required, and a source capable of emitting such high current was yet to be discovered^{13,17,18}.

In 1975, the first focused ion beam (FIB) tool was introduced by Levi-Setti. It used field ionization sources discovered by Erwin Mueller in the 1950s, in which a very sharp tip (with radius of curvature on the order of a few nanometers) was used to ionize a gas below its atmospheric pressure (rarefied gas)¹³. The liquid metal ion source (LMIS) FIB was developed in 1978, enabling highly focused ion beams and is the basis of the current FIB systems used commercially^{13,18-20}. A FIB system operation mechanism is very similar to a SEM, but rather than using electrons, ions are used to interact with the surface of the materials. Most FIBs use Gallium (Ga) as their source with a tungsten needle to generate ions. Ions, like electrons, can be used to image the surface, however the interaction of ions with matter, is rather destructive which leads to removal of the materials from the surface through elastic collision of the ions with the atoms of the target materials. This interaction, if the ions are energetic enough, can eject atoms from the target material while a portion of the incident ions can scatter from the surface and be collected by the detector to form an image^{17,18,20,21}. Figure 16 illustrates how the FIB etches away the atoms from the target material.

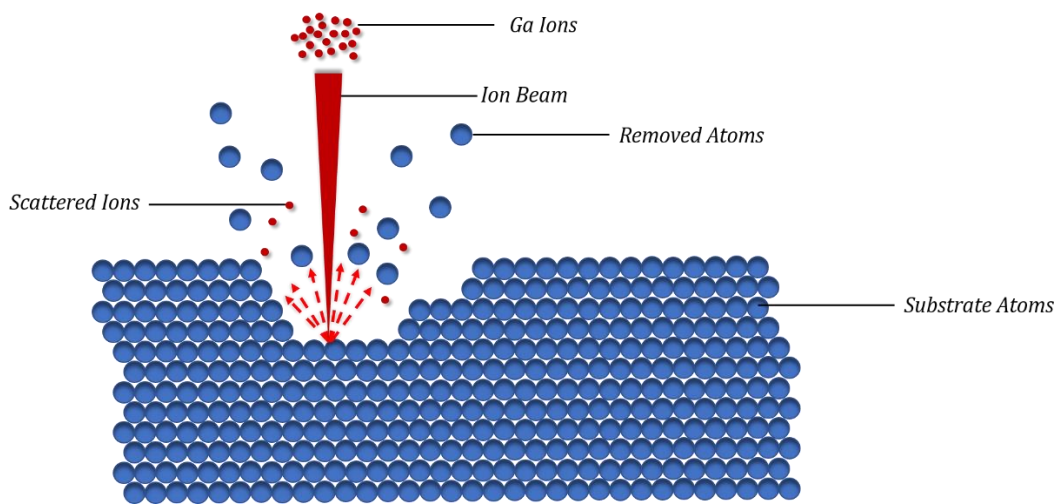


Figure 16. Schematic of a beam of focused ions used to remove atoms from the surface. The scattered ions can be used to form an image of the specimen, similar to electron imaging in SEM.

The current used for milling varies from one material to another and that defines how well and effective the atoms are removed. Most current FIBs have pre-determined doses for various materials which have been experimentally achieved and can be selected on the tool's user interface. The new generation of FIB tools often are equipped with an electron column (dual beam) offering SEM capability which is useful for imaging the surface during the milling without destructively interacting with the material. In the dual beam tools, the electron beam and the ion beam columns are placed at 52° angle from one another. The milling ability of a FIB is widely utilized in sample preparation for other types of microscopy such as TEM, where the specimen is carefully extracted from the surface and is mounted onto a TEM grid, a process in which the ion beam is used both for material removal and material deposition. Deposition of material, typically platinum (Pt), from an organic based gas with the help of ions from the FIB is used to cover and protect certain regions of the specimen while other regions are milled (see Appendix A for more detail).

The FIB in this work was used for both fabrication of nanoscale devices on the metallic materials and for lift-out processes as part of sample preparation for transmission electron microscopy. The FIB was a FEI Helios NanoLab 650 SEM/FIB, a

dual beam tool, that is housed in the CSM in 4D LABS facility at Simon Fraser University, Burnaby campus [Figure 17].

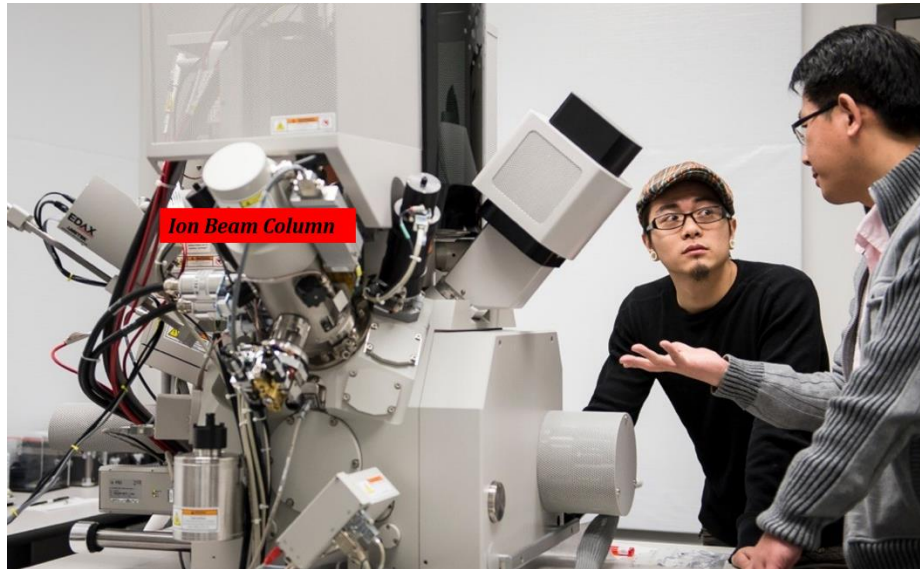


Figure 17. The Helios dual beam microscope located at CSM in 4D LABS facility⁷.

2.7. Physical Vapour Deposition

Physical vapour deposition (PVD) is a technique in which films of materials can be deposited on a substrate under vacuum to achieve thicknesses ranging from a few angstroms to microns,²². The process requires a source to be heated to temperatures at which the materials get vaporized and a substrate on which the material is deposited, usually maintained at a temperature at which the material vapor remains in the solid state following collision with the substrate²²⁻²⁴. In general elemental films, alloys, metal oxides and some polymeric materials can be deposited using this technique²². One

⁷ https://www.sfu.ca/sfunews/stories/2014/sfu_s-new-centre-for-soft-materials-a-boon-to-researchers.html

major advantage of this process is the environment in which the material deposition takes place. The vacuum maintained in the deposition chamber, provides a high level of purity for the deposited film. The low-pressure condition (typically 10^{-4} Torr) minimizes the collision of the vaporized materials with the gas molecules during the deposition which improves the quality of the film and the uniformity of the deposition²³.

The first evaporation deposition of metal under vacuum was done by Nahrwold (1887) to measure the refractive indices of the thin films. However, this technique did not become a popular approach for the deposition of metallic films until the 1920s, and since then the vacuum evaporation of materials is a commonly used process in many industries²²⁻²⁴. There are three general categories under which the physical evaporation is recognized:

- Vacuum evaporation
- Sputter deposition (Ion plating)
- Arc vapour deposition

Vacuum evaporation typically refers to processes where the source material is heated to a temperature at which it readily vaporizes either through resistive heating of a boat that houses the material to be deposited, or in the case of high melting point materials, by electron beam evaporation, in which an incident electron beam is used to vaporize the material (see below). Since there is nothing in between the source and the substrate, the evaporated particles will reach the substrate without any interference; this is a common technique for depositing metal and some metal oxides²². The sputter deposition mechanism involves ignition of plasma in the chamber and uses the charged particle collisions with the source to remove atoms which then will be deposited on the substrate^{22,23}. This process often provides a better material coverage and higher uniformity compared to vacuum evaporation. In arc vapour deposition, the source is being heated under high current with a low-voltage electric arc at low gas pressure to the point at which the material gets evaporated, which then will be deposited on the substrate that is located above the source^{22,23}.

Beam of electrons can also be used to vaporized metallic films. In this technique, electrons are generated by the electron gun which is capable of providing powers

ranging from 0.030-1.2 MW at high voltages (20-50 kV) and by steering the electron beam towards the source material using electromagnets, the metal in the ceramic crucible will be bombarded by the electrons²⁵. The electron beam (e-beam) and metal interaction causing the metal to melt and evaporate and consequently the vaporized metal will be deposited on the substrate which is placed above the source. One of the main differences between thermally evaporated films and the e-beam evaporated films is the quality of the deposited metal. The metallic films deposited by thermal PVD tools are often grainy with metal crystallites that are large. However the size of the grains also depends on the rate at which the metal is deposited (slower rate = finer grain sizes). Electron-beam evaporated films are often deposited with much smaller grains and better uniformity is typically achieved.

The deposited films described in this thesis are of metallic nature and thin layers of these metals were obtained using the thermal evaporation technique. The PVD tools used for depositing metals in this thesis work, are housed in 4D LABS at the clean room facility. The deposited gold (Au) nanostructures on polycrystalline Au surfaces were obtained by using a dual source PVD tool capable of evaporating metals both thermally and with an e-beam. The thermal source was used for depositing chromium (Cr) which is a common metal to improve adhesion of Au film on the substrate. The e-beam is used in this tool to deposit titanium (Ti), Au, Pt and palladium (Pd). The tool is a PVD75 model Kurt J. Lesker PVD with base pressure of 5E-7 Torr [Figure 18].



Figure 18. The e-beam/thermal PVD at 4D LABS clean room which is listed as PVD 3⁸.

The single crystal silver (Ag) used in this work was deposited thermally by a PVD75 model Kurt J. Lesker PVD which is capable of depositing metals by both sputtering or thermal evaporation. The process under which the Ag was deposited will be described briefly in later chapters. The polycrystalline Au films were deposited using a custom built thermal evaporator with two thermal sources and co-deposition capability. This tool is located outside of clean room at the 4D LABS facility and is used to deposit Cr, Au, Al, copper (Cu), Ag, nickel (Ni), indium (In) and Au:Ge (germanium) [Figure 19].

⁸ <https://users.4D LABS.ca/tools/pvd3.html>



Figure 19. The custom build PVD at the 4D LABS facility which is listed as PVD 5⁹.

2.8. Integrating Sphere Absorption Measurements

An integrating sphere is an optical tool used for measuring the reflectance, transmittance and absorbance of UV, visible and NIR photons from specular type surfaces and from samples that scatter incoming photons^{26–29}. To study the coupling of incident light to the nanostructured metallic surfaces described in this thesis, an integrating sphere-based absorption measurement system was established to collect reflected and scattered photons following interaction of the incident radiation with the plasmonic surface. Comparison of the light collected following interaction with a nanostructured surface to that of a highly reflecting planar surface of the same material

⁹ <https://users.4D LABS.ca/tools/pvd5.html>

(a reference sample), allows one to infer the magnitude of light absorbed by the nanostructured sample. The inner part of an integrating sphere is made of materials such as barium sulfate, that are highly reflective and that allow photons to be collected after numerous reflections off of the walls of the integrating sphere. Light that undergoes multiple reflections from the inner walls of the integrating sphere is captured through a small opening (port) in the sphere and light is collected via a fiber optic cable and directed to a spectral detector²⁶. This device is often used for measuring the optical flux or the attenuation of the radiation which is externally guided towards to the sample located at the center of the sphere^{28,29}. The output of the sphere is an integration of all reflected photons which is directly proportional to the incident beam from the source. This can be shown by²⁷:

$$L = \frac{\Phi}{\pi \cdot A_s} \cdot M \quad (20)$$

where L is radiance of the wall of the sphere, Φ is the optical flux, A_s is the area of the interior of the sphere and M is the sphere multiplier which in fact is the average numbers of reflection taking place inside the integrating sphere²⁷:

$$M = \frac{1}{1 - \bar{\rho}} \quad (21)$$

where $\bar{\rho}$ is the average reflectance from the wall of the sphere.

The position of the sample at the center of the sphere can be used to study the interaction of the light at different polarizations with the nanostructures by rotating the sample holder. In the setup used for this thesis work, the beam of light is introduced to the sample via the optical entrance of the integrating sphere after being focused by sets concave lenses. An iris was placed at the optical path of the beam of light to control the amount of light entering the sphere and a polarizer was used to control the polarization of the incident light. To avoid zero-degree reflection from the sample which would lead to the incident light to leave the sphere through the optical entrance, the holder was held at 5° angle which was the minimum angle used to study the plasmonic nanostructured surfaces. The integrating sphere used in this work is manufactured by Labsphere (6" in diameter) and connected to an Oriel Instruments Newport spectrometer via a fiber optic

cable with 20 μm diameter. Figure 20 illustrates the setup used for the characterize the plasmonic nanostructures.

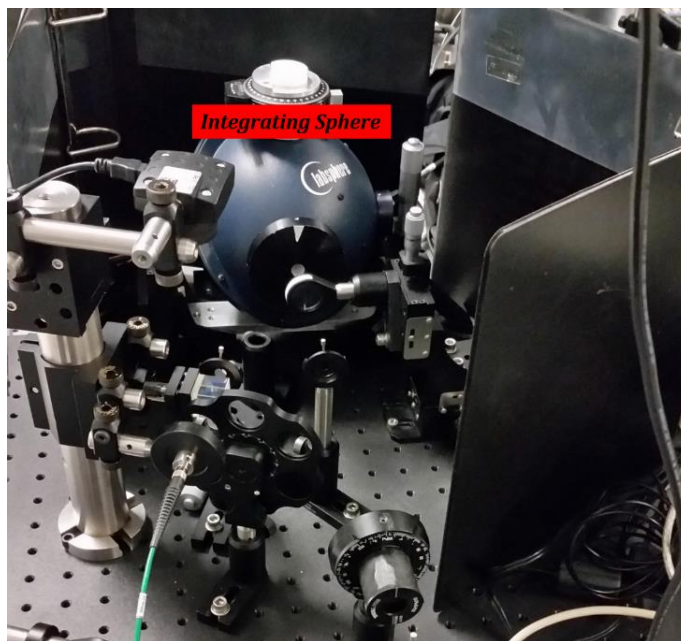


Figure 20. *The integrating sphere and the optical components for directing the light into the sphere that were used for the absorption measurements.*

2.9. Multiphoton Photoluminescence Analysis

The photoluminescence of the noble metals was first reported by Mooradian in 1969 when he demonstrated the photon emission from Cu and Au films upon single photon excitation³⁰. He speculated that this process is due to excitation of *d*-band electrons to the *sp*-band followed by electron-hole recombination^{30–32}. The emission from nanostructured surfaces demonstrated a slight shift in the emitted spectral peak compared to planar films which was attributed to excitation of locally excited plasmons³¹. The photoluminescence from noble metals can also be achieved through a multiphoton absorption-emission process. This mechanism, however does not produce any photoemission in smooth surfaces, which suggests that the luminescence is strongly related to the local plasmon excitation on the nanostructures. The theory behind this

process is thought to be governed by both the *d*-band and *sp*-band electrons and the plasmon excitation which then enables routes for electron-hole recombination from the *sp*-band to the *d*-band enhanced by the generated plasmons. The process will also be determined by radiative decay of the locally excited plasmons occurring within the *sp*-band of the metal (intraband transitions) which leads to emission of longer wavelength photons in the NIR and IR region³¹⁻³³. It was observed that the luminescence intensity significantly decreases for photons emitted from the nanostructures at higher energy (400-500 nm) and this is attributed to the lack of influence of excited plasmons on the electrons located at the lower *d*-band³¹⁻³⁴. The emission characteristic depends mainly on the interband transition which is directly related to crystalline direction of the nanostructure and the position of the *d*-band energy and its density of the states within the symmetry points of the crystal at the first Brillouin zone (a defined primitive cell in the reciprocal space of a lattice structure)^{33,34}.

The multiphoton luminescence (MPL) process is often used for imaging biological molecules, but in recent years, has become a widely used technique for analysis of plasmonic nanostructures and plasmonic devices. The emission spectra contain information on the plasmonic characteristics of the materials and the devices. The luminescence and the enhancement imparted by the local plasmonic field are directly influenced by the shape, size, crystalline orientation, material quality, and the efficiency of the plasmonic devices³³⁻³⁸. The MPL requires an ultrafast laser with pulse durations of order picoseconds (ps) or faster for inducing plasmon mediated photoemission from the nanostructures of noble metals. For MPL measurements, a laser scanning microscope (LSM) is typically used which is equipped with an ultrafast laser source (fs pulse duration) with the capability of tuning the laser wavelength. The detector used for imaging takes advantage of a filter which blocks the wavelength with which the materials are excited, but also imposes a limitation for detecting longer wavelength emission. Despite the limitation on the spectral detection, LSMs can still provide useful information on the plasmonic characteristics of the nanostructures and plasmonic devices as will be demonstrated in later chapters of this thesis.

The MPL analysis of this work was done at the Laboratory for Advanced Spectroscopy and Imaging Research (LASIR), a shared facility between SFU and University of British Columbia (UBC). The measurements at UBC were performed with a

Zeiss LSM510 two photon scanning confocal microscope equipped with a Coherent Chameleon XR femtosecond laser with 700-1000 nm tuning range [Figure 21a]. The MPL analysis at SFU was carried out using a Leica SP5 laser scanning confocal two photon microscope using a Coherent Chameleon Vision II with 680-1080 nm spectral range tuning capability [Figure 21b].

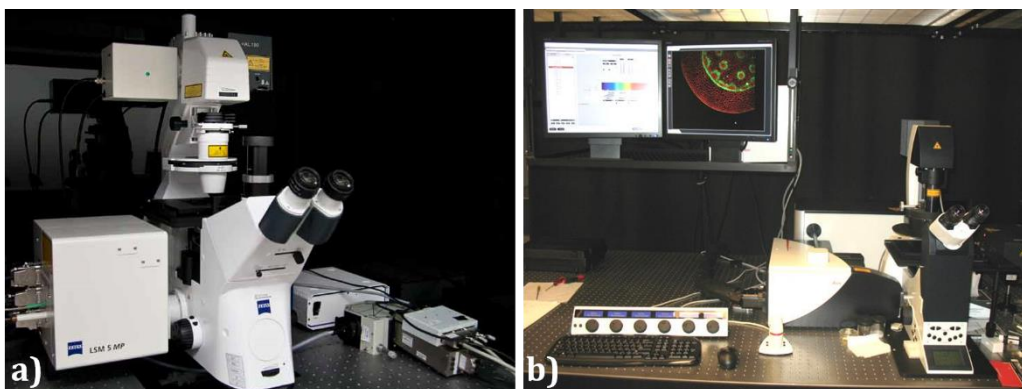


Figure 21. Multi-photon fluorescence microscopes available in LASIR facility, a) is a Zeiss LSM510 two photon scanning confocal microscope housed in LASIR facility at UBC and b) is Leica SP5 laser scanning confocal two photon microscope located at LASIR at SFU.

2.10. Raman and Surface Enhanced Raman Spectroscopy

Raman spectroscopy is based on the process of inelastic light scattering, first discovered by Sir C. V. Raman in 1928 for which he was awarded the Nobel prize for physics in 1930^{39,40}. Raman scattering describes an inelastic process in which incident photons ($E_0=h\nu$) interact with a material and scatter from the material with a different energy ($E_1=h\nu'$)³⁹⁻⁴¹. The difference in the energies ($\Delta E= E_1-E_0$) of the scattered photons and the incident photons is due to the interaction of the photons with the vibrational states of the material, which can lead to scattered photons from the material at lower energy (known as Stokes Raman scattering), or at higher energy (known as Anti-Stokes Raman scattering)³⁹⁻⁴². In the case of Stokes Raman scattering, the scattered photons leave the material vibrationally excited and the energy difference between the incident photons and the scattered photons are equal to the energy of the

vibrational state that had interacted with the incoming photons³⁹⁻⁴². Anti-Stokes Raman scattering results from scattering of incident photons from a vibrationally excited material. The resulting scattered photons have higher energy than the incident photons and leave behind a material in a lower vibrational³⁹⁻⁴².

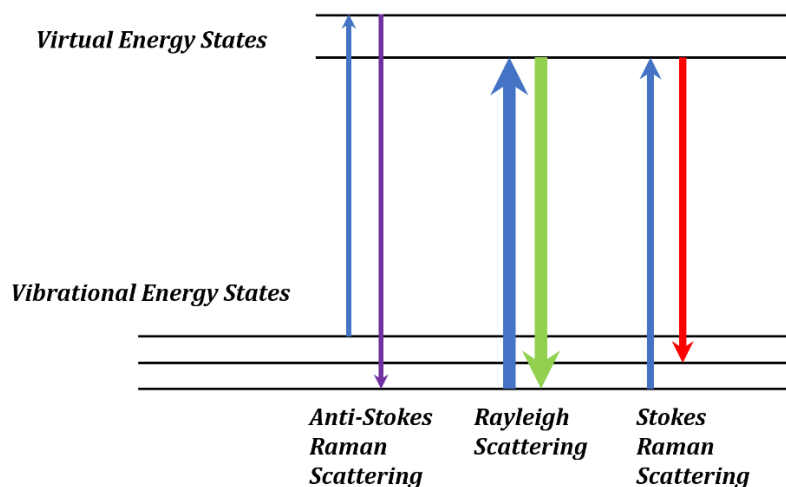


Figure 22. Illustration of energy levels in a Raman scattering process.

Since the Raman scattered photons contain information about the chemical bonds and the material composition, this approach has become a widely used spectroscopic technique to study properties of materials. One major difference between IR spectroscopy and Raman spectroscopy is in what the collected photons represent. In Raman spectroscopy the intensity of the detected photons is representing the change of the polarizability of the molecules by vibrations whereas, in IR spectroscopy, it is the change in the dipole moment of the molecule with vibration that contributes to the intensity of IR lines⁴³. One main hurdle in Raman spectroscopy is low Raman scattering efficiency and the detection of the Raman scattered photons. The Rayleigh scattered photons have much higher intensity compared to Raman scattered photons making the detection and separation of Raman spectra difficult and requiring additional steps to eliminate the Rayleigh lines from the collected spectra. Before the invention of the laser, Raman spectroscopy was carried out by using polychromatic light sources (mainly mercury arc lamps) and photographic filters to produce a monochromatic spectrum⁴⁴. The popularity of Raman spectroscopy increased in the 1960s when lasers became a

reliable and more widely available monochromatic light source. This trend has continued with improvement in detector sensitivity, optical filter technology and instrument design and has led to the common use Raman spectrometers and microscopes⁴⁴⁻⁴⁶. In Raman microscopes, a laser is used as the primary monochromatic light source which is being directed and focused onto the sample by the objective lens at normal incidence⁴⁶. The scattered photons pass through a filter to remove the wavelengths corresponding to the laser Rayleigh scattering and are then directed to an optical detector, often a charge-couple device (CCD) for further analysis⁴⁶.

In 1978 it was discovered that the Raman scattering of the adsorbed molecules to Ag surfaces undergoes a 10^6 fold enhancement^{47,48}. Initial observation was reported by Fleischmann in 1974 where he used a roughened Ag electrode, to improve the surface area for adsorption of pyridine molecules in an aqueous solution for an *in situ* chemical spectroscopy. However, it was shown by Van Duyne and Creighton that the intense Raman signal is due to the locally excited surface plasmons from the textured Ag surface which led to foundation of the surface-enhanced Raman spectroscopy (SERS)^{47,48}. The excitation of surface plasmons on nanostructured surfaces by light at the plasmon resonance or near resonance frequency of the metallic nanostructures will generate an electric field at the vicinity of the metal surface which then results in an enhancement in the molecule's polarizability followed by an amplification in the intensity of Raman scattered photons⁴⁷⁻⁵⁰. The area of SERS has come a long way since it was first discovered. Today, the surface enhanced Raman spectroscopy is widely used in different areas of science and substrates are commercially available for variety of applications such as cancer research and early cancer detection, biological sciences, material science, biomedical and molecular imaging, pharmaceutical, etc⁵⁰⁻⁵³.

The Raman measurements obtained in this thesis, was carried out by an inVia confocal Raman microscope manufactured by Renishaw equipped with both 514 nm Argon ion laser and 785 nm diode laser [Figure 23].



Figure 23. A Renishaw inVia Raman microscope used for Raman spectroscopy and demonstrating the SERS from the substrates made in this thesis work.

2.11. Finite-Difference Time-Domain

Fabrication of devices that can interact with light and exhibit plasmonic response can be very costly, especially when they are comprised of features at the nanometer size scale. Therefore special care needs to be taken in order to minimize the number of iterations required for making such devices by predicting the behaviour of these systems before hand. The common approach is to use numerical calculation to simulate the interaction of incident electromagnetic radiation with the designed device, incorporating the materials' physical and optical properties. Solving Maxwell's equations with finite-difference time-domain (FDTD) methods is one approach to model the wave-matter interactions for optical devices. This method was first introduced in 1966 by Kane S. Yee where he proposed a discrete solution to the Maxwell's equations in the time domain^{54,55}. It almost took a decade for Yee's method to gain interest when Taflove and Brodwin simulated light scattering by dielectric cylinders and biological heating and later on by Holland where he made a prediction on the effect of electromagnetic pulses in inducing current on an aircraft⁵⁵.

Since then, FDTD has matured to the point that it has become a standard method for simulating devices in a variety of industries and there are highly

sophisticated software packages developed to address the needs for simulating photonic and opto-electronic devices accurately. In most FDTD simulation tools, the designed device will be confined within a closed environment with appropriate boundary conditions which defines how the propagating electromagnetic wave should be treated once it reaches those boundaries. Often these tools contain a library of materials with existing information on their properties, such as the permittivity and the refractive index, which are used (by default) for the device under simulation⁵⁵. Once the materials are defined, the simulated region will be broken down into smaller grids, with the smaller the grid size the higher the accuracy of the simulation. Maxwell's equations are solved at each point on the grid and the overall wave-matter interaction can then be plotted in terms of the local or scattered wavelength dependent electric and magnetic fields. Alternatively, an image in which the intensity of the local fields both in 2D and 3D in all planes can be rendered⁵⁵.

The numerical simulations presented in this work were performed by Lumerical Solutions software package, where the interaction of electromagnetic radiation with the designed plasmonic nano-antennas were predicted using the FDTD method. The design of the antennas, the plasmonic devices and the simulation of their activities were performed solely by the author of this thesis.

References

1. Ryland, A. L. X-ray diffraction. *J. Chem. Educ.* **35**, 80 (1958).
2. Seeck, S. & Seeck, O. H. *X-Ray Diffraction*. (20150210).
3. Padua, G. W. & Wang, Q. *Nanotechnology Research Methods for Food and Bioproducts*. (Wiley, 2012).
4. Storey, R. A., YmÃ©n, I. & YmÃ©n, I. *Solid State Characterization of Pharmaceuticals*. (John Wiley & Sons, Incorporated, 2011).
5. Lehmann, C. W. Two-Dimensional X-Ray Diffraction , *Angew. Chem. Int. Ed.* **49**, 4858–4859 (2010).

6. Reichelt, R. Scanning Electron Microscopy. in *Science of Microscopy* 133–272 (Springer, New York, NY, 2007). doi:10.1007/978-0-387-49762-4_3
7. Wang, Y. & Petrova, V. Scanning Electron Microscopy. in *Nanotechnology Research Methods for Foods and Bioproducts* (eds. Padua, G. W. & Wang, Q.) 103–126 (Wiley-Blackwell, 2012). doi:10.1002/9781118229347.ch6
8. Schäfer, R., Schmidt, P. C., Schäfer, R., Schfer, R. & Schfer, R. *Methods in Physical Chemistry*. (John Wiley & Sons, Incorporated, 2012).
9. van Tendeloo, G., van Dyck, D. & Pennycook, S. J. *Handbook of Nanoscopy*. (John Wiley & Sons, Incorporated, 2012).
10. Bruce, D. W., O'Hare, D. & Walton, R. I. *Multi Length-Scale Characterisation: Inorganic Materials Series*. (Wiley, 2013).
11. Rugar, D. & Hansma, P. Atomic Force Microscopy. *Phys. Today* **43**, 23 (2008).
12. *Atomic Force Microscopy*. (Oxford University Press, 2010).
13. Landis, L. Electron Beam Lithography. in *Lithography* 101–182 (20130307).
14. Broers, A. N., Hoole, A. C. F. & Ryan, J. M. Electron beam lithography—Resolution limits. *Microelectron. Eng.* **32**, 131–142 (1996).
15. Vieu, C. *et al.* Electron beam lithography: resolution limits and applications. *Appl. Surf. Sci.* **164**, 111–117 (2000).
16. Tseng, A. A., Chen, K., Chen, C. D. & Ma, K. J. Electron beam lithography in nanoscale fabrication: recent development. *IEEE Trans. Electron. Packag. Manuf.* **26**, 141–149 (2003).
17. Giannuzzi, L. A., Prenitzer, B. I. & Kempshall, B. W. Ion - Solid Interactions. in *Introduction to Focused Ion Beams* 13–52 (Springer, Boston, MA, 2005). doi:10.1007/0-387-23313-X_2
18. Stevie, F. A., Giannuzzi, L. A. & Prenitzer, B. I. The Focused Ion Beam Instrument. in *Introduction to Focused Ion Beams* 1–12 (Springer, Boston, MA, 2005). doi:10.1007/0-387-23313-X_1
19. Stevie, F. A., Griffis, D. P. & Russell, P. E. Focused Ion Beam Gases for Deposition and Enhanced Etch. in *Introduction to Focused Ion Beams* 53–72 (Springer, Boston, MA, 2005). doi:10.1007/0-387-23313-X_3
20. Young, R. J. & Moore, M. V. Dual-Beam (FIB-SEM) Systems. in *Introduction to Focused Ion Beams* 247–268 (Springer, Boston, MA, 2005). doi:10.1007/0-387-23313-X_12

21. Principe, E. L. Application of FIB in Combination with Auger Electron Spectroscopy. in *Introduction to Focused Ion Beams* 301–327 (Springer, Boston, MA, 2005). doi:10.1007/0-387-23313-X_15
22. Mattox, D. M. Physical vapor deposition (PVD) processes. *Met. Finish.* **99**, 409–423 (2001).
23. Mattox, D. M. Chapter 6 - Vacuum Evaporation and Vacuum Deposition. in *Handbook of Physical Vapor Deposition (PVD) Processing (Second Edition)* 195–235 (William Andrew Publishing, 2010). doi:10.1016/B978-0-8155-2037-5.00006-X
24. Bishop, C. A. 16 - Thermal Evaporation. in *Vacuum Deposition onto Webs, Films and Foils (Second Edition)* 273–303 (William Andrew Publishing, 2011). doi:10.1016/B978-1-4377-7867-0.00016-7
25. Bishop, C. A. 15 - Electron Beam (E-beam) Evaporation. in *Vacuum Deposition onto Webs, Films and Foils (Second Edition)* 261–272 (William Andrew Publishing, 2011). doi:10.1016/B978-1-4377-7867-0.00015-5
26. Hanssen, L. Integrating-sphere system and method for absolute measurement of transmittance, reflectance, and absorptance of specular samples. *Appl. Opt.* **40**, 3196–3204 (2001).
27. Arecchi, A. V., Messadi, T. & Koshel, R. J. Integrating Sphere. (2007). doi:10.1117/3.764682.p67
28. 47. Jacquez, J. A. & Kuppenheim, H. F. Theory of the Integrating Sphere. *JOSA* **45**, 460–470 (1955).
29. Grant, B. G. The Integrating Sphere. 25–26 (2011). doi:10.1117/3.903926.ch25
30. Mooradian, A. Photoluminescence of Metals. *Phys. Rev. Lett.* **22**, 185–187 (1969).
31. Boyd, G. T., Yu, Z. H. & Shen, Y. R. Photoinduced luminescence from the noble metals and its enhancement on roughened surfaces. *Phys. Rev. B* **33**, 7923–7936 (1986).
32. Shahbazyan, T. V. Theory of Plasmon-Enhanced Metal Photoluminescence. *Nano Lett.* **13**, 194–198 (2013).
33. Ngoc, L. L. T., Wiedemair, J., Berg, A. van den & Carlen, E. T. Plasmon-modulated photoluminescence from gold nanostructures and its dependence on plasmon resonance, excitation energy, and band structure. *Opt. Express* **23**, 5547–5564 (2015).
34. Beversluis, M. R., Bouhelier, A. & Novotny, L. Continuum generation from single gold nanostructures through near-field mediated intraband transitions. *Phys. Rev. B* **68**, 115433 (2003).

35. Wang, D.-S., Hsu, F.-Y. & Lin, C.-W. Surface plasmon effects on two photon luminescence of gold nanorods. *Opt. Express* **17**, 11350–11359 (2009).
36. Bouhelier, A. *et al.* Surface Plasmon Characteristics of Tunable Photoluminescence in Single Gold Nanorods. *Phys. Rev. Lett.* **95**, 267405 (2005).
37. Mühlischlegel, P., Eisler, H.-J., Martin, O. J. F., Hecht, B. & Pohl, D. W. Resonant Optical Antennas. *Science* **308**, 1607–1609 (2005).
38. Huang, J.-S. *et al.* Atomically flat single-crystalline gold nanostructures for plasmonic nanocircuitry. *Nat. Commun.* **1**, 150 (2010).
39. Andrews, D. L. Rayleigh Scattering and Raman Effect, Theory*. in *Encyclopedia of Spectroscopy and Spectrometry (Second Edition)* (ed. Lindon, J. C.) 2413–2419 (Academic Press, 1999). doi:10.1016/B978-0-12-374413-5.00269-4
40. Linne, M. A. *Spectroscopic Measurement: An Introduction to the Fundamentals*. (Elsevier Science, 2002).
41. Amer, M. *Raman Spectroscopy for Soft Matter Applications*. (Wiley, 2009).
42. Nafie, L. A. Raman Optical Activity, Theory*. in *Encyclopedia of Spectroscopy and Spectrometry (Second Edition)* (ed. Lindon, J. C.) 2397–2405 (Academic Press, 2010). doi:10.1016/B978-0-12-374413-5.00267-0
43. Schrader, B. Raman Spectrometers*. in *Encyclopedia of Spectroscopy and Spectrometry (Second Edition)* (ed. Lindon, J. C.) 2406–2412 (Academic Press, 1999). doi:10.1016/B978-0-12-374413-5.00268-2
44. Gerrard, D. L. & Bowley, H. J. Instrumentation for Raman Spectroscopy. in *Practical Raman Spectroscopy* 55–76 (Springer, Berlin, Heidelberg, 1989). doi:10.1007/978-3-642-74040-4_3
45. Turrell, G. Raman Sampling. in *Practical Raman Spectroscopy* 13–54 (Springer, Berlin, Heidelberg, 1989). doi:10.1007/978-3-642-74040-4_2
46. Loudon, J. D. Raman Microscopy. in *Practical Raman Spectroscopy* 119–151 (Springer, Berlin, Heidelberg, 1989). doi:10.1007/978-3-642-74040-4_6
47. Moskovits, M. Surface-Enhanced Spectroscopy. *Rev. Mod. Phys.* **57**, 783–826 (1985).
48. Campion, A. & Kambhampati, P. Surface-Enhanced Raman Scattering. *Chem. Soc. Rev.* **27**, 241–250 (1998).
49. Stockman, M. I. Electromagnetic Theory of SERS. in *Surface-Enhanced Raman Scattering* 47–65 (Springer, Berlin, Heidelberg, 2006). doi:10.1007/3-540-33567-6_3

50. Moskovits, M. Surface-Enhanced Raman Spectroscopy: a Brief Perspective. in *Surface-Enhanced Raman Scattering* 1–17 (Springer, Berlin, Heidelberg, 2006). doi:10.1007/3-540-33567-6_1
51. Drachev, V. P. & Shalaev, V. M. Biomolecule Sensing with Adaptive Plasmonic Nanostructures. in *Surface-Enhanced Raman Scattering* 351–366 (Springer, Berlin, Heidelberg, 2006). doi:10.1007/3-540-33567-6_18
52. Tian, Z.-Q., Yang, Z.-L., Ren, B. & Wu, D.-Y. SERS From Transition Metals and Excited by Ultraviolet Light. in *Surface-Enhanced Raman Scattering* 125–146 (Springer, Berlin, Heidelberg, 2006). doi:10.1007/3-540-33567-6_7
53. Kneipp, J. Nanosensors Based on SERS for Applications in Living Cells. in *Surface-Enhanced Raman Scattering* 335–349 (Springer, Berlin, Heidelberg, 2006). doi:10.1007/3-540-33567-6_17
54. Taflove, A. Review of the Formulation and Applications of the Finite-Difference Time-Domain Method for Numerical Modeling of Electromagnetic Wave Interactions with Arbitrary Structures. *Wave Motion* **10**, 547–582 (1988).
55. Gedney, S. D. Introduction to the Finite-Difference Time-Domain (FDTD) Method for Electromagnetics. *Synth. Lect. Comput. Electromagn.* **6**, 1–250 (2011).

3. Electrochemical Reduction of Metal Ions from Hydroxide Ion Oxidation

The reduction potential of a species is a measure of its tendency to acquire electrons and thereby be reduced. The standard reduction potentials, measured against the standard hydrogen electrode, describe half reactions in which species present under standard conditions, are reduced. These values can help to predict thermodynamically favourable oxidation and reduction processes and to indicate whether particular redox processes are expected to occur spontaneously, however the rates at which species are reduced or oxidized are determined by kinetics and depend on the detailed mechanism of the reduction or oxidation process. These rates are determined empirically for a given electrochemical system under the prevailing experimental conditions.

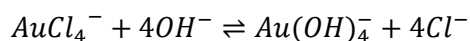
The deposition of metals through the reduction of metal ions without any external potential is known as electroless deposition, where the required electrons for the reduction of solvated metal ions in the electrolyte solution are provided by reducing agents. In the electroless deposition process, the reducing agents are compounds that have a lower reduction potential than the metal ions, resulting in an overall positive cell potential and enabling the spontaneous reduction of metal ions at the expense of oxidation of the reducing agent. Therefore care must be taken in choosing the appropriate reducing agents that favor this route¹. Surfaces made of materials with lower oxidation potential than the ionic metal species in an electrochemical bath can also act as reducing agents. These surfaces will undergo oxidation when placed in a bath containing solvated ions with higher reduction potential. This spontaneous electrochemical process is known as galvanic replacement and results in the displacement of surface atoms by the reduced ionic metal species.

Dissolved metal ions in aqueous electrolyte solutions often form complexes with water molecules or other soluble ligands that can influence the reduction potential of the ions. This mechanism can be used to influence the redox potential of the metal ions to

make the process more compatible with the substrates on which the metal is to be deposited.

The focus of this research is to introduce a new and novel deposition technique to form single crystal and ultra-smooth plasmonic metal surfaces. These films can then be used to fabricate metasurfaces and plasmonic surface nanostructures with control over their crystalline orientation. The process offers a platform for deposition of both plasmonic and non-plasmonic metals and their alloys through electroless deposition chemistry. Furthermore, this chemistry can be readily carried out in non-cleanroom conditions and coupled with various patterning methods to provide a new and cost-effective approach to the fabrication of nanostructured plasmonic-based devices. In this approach, a solution with a high level of alkalinity is used as a deposition bath to reduce gold (Au) from its ionic form onto a single crystal (100) silver (Ag) substrate which was utilized as the template. The Ag metal was chosen due to the closeness of the lattice constants of Ag and Au ($a_{\text{Ag}} = 4.08 \text{ \AA}$ and $a_{\text{Au}} = 4.07 \text{ \AA}$)² with the idea that the gold may grow epitaxially, with the metallic adlayer film following the same crystalline orientation of the supporting Ag substrate.

The presence of hydroxide ions (OH^-) in a deposition bath containing Au^{3+} ions allows for the formation of Au^{3+} -based hydroxide complexes whose nature and number will be determined by the concentration of species in solution and the equilibrium stability constants for these complexes^{3,4}. The stabilities and reduction potentials of Au cations can be predicted by the Pourbaix stability diagram under different pH levels³. The deposition baths employed in this work primarily contain 1 M sodium hydroxide (NaOH), which is prepared by dissolving an appropriate amount of NaOH in de-ionized water (DI-water). The gold compound used for electroless deposition was the strong monoprotic acid HAuCl_4 (chloroauric acid), which forms H^+ and AuCl_4^- once dissolved in DI-water. The presence of excess OH^- in the bath forces the gold chloride anions to undergo ligand exchange to form⁵ $\text{Au}(\text{OH})_4^-$:



From the Pourbaix diagram, it can also be seen that under such highly alkaline conditions (pH=14), the most stable Au complex is in form of $\text{Au}(\text{OH})_4^-$ ^{3,4}.

Under non-alkaline conditions (pH≈6), the presence of a Ag film in a solution containing AuCl_4^- ions leads to galvanic replacement of Ag atoms by AuCl_4^- ions in which the reduction of Au^{3+} cations occurs through oxidation of silver atoms that comprise the film [Figure 24]:

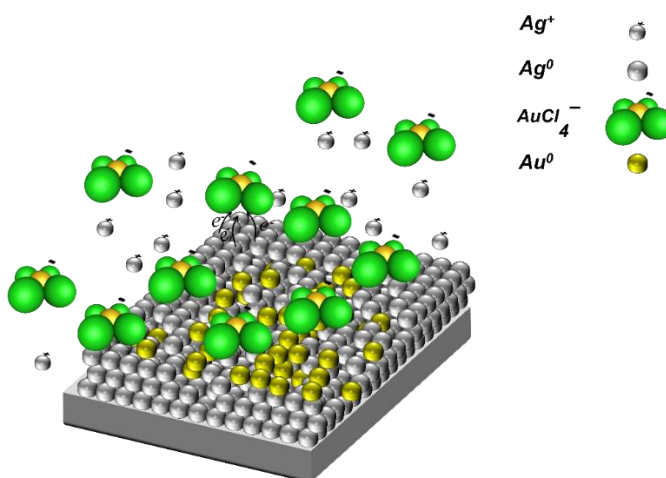
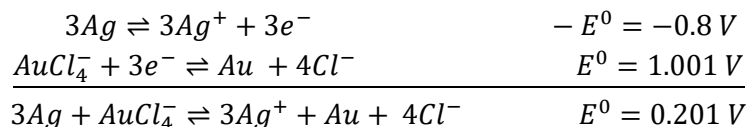


Figure 24. Illustration of galvanic replacement of Ag atoms by Au^{3+} ions that leads to formation of a porous and polycrystalline gold film.

The cell potential associated with the above redox reaction suggests that the reduction of every Au^{3+} ion is through oxidation of three Ag atoms and that it should occur spontaneously. It is observed that this is indeed the case as almost immediately after the Ag film is placed inside a solution containing Au ions, the result is the formation of a poor quality, porous, oxidized film containing Ag and Au, as shown in Figure 25.

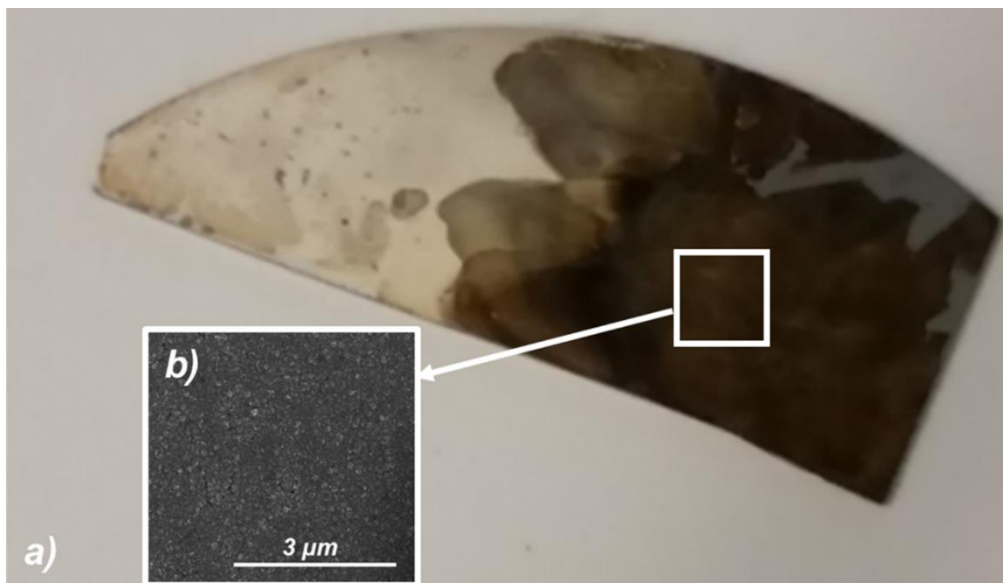


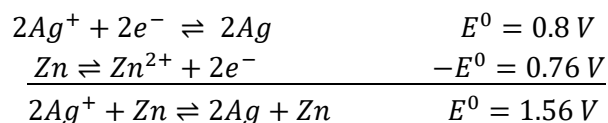
Figure 25. Single crystal Ag(100) film which has undergone galvanic replacement by Au cations obtained by dissolving H₂AuCl₄ in deionized water; a) shows the macroscopic appearance of the Ag(100) film and b) shows the SEM image of the galvanically replaced region.

Galvanic replacement has been used as a strategy to metallize semiconductor substrates such as silicon (Si), or to create porous surface bi-metallic films and their alloys for catalysis applications⁶⁻¹². However, in the work described in this thesis, it is not a desired process. It was intended to develop an electrochemical bath that shuts off all routes for oxidation of the substrate. This goal was achieved by the use of a highly alkaline electrolyte bath in which the etch-free deposition of gold onto single crystal silver substrates was demonstrated. Consequently gold films were grown epitaxially on Ag(100) substrates forming monocrystalline Au(100) films. The detailed film characterization is presented in the next chapter.

The suppression of galvanic replacement in an alkaline deposition bath is due to the presence of OH⁻ ions in large concentration which leads not only to the formation of Au(OH)₄⁻ complexes, as discussed, but also shifts the energy barrier to silver oxidation. The redox potential of Au(OH)₄⁻ under standard conditions has been reported to be E⁰ = 0.488 ± 0.003 V⁵. In order to determine whether this value is correct, the standard

reduction potential of the $\text{Au}(\text{OH})_4^-$ complexes in the deposition bath was measured by constructing a galvanic cell. Such a cell allows for the direct measurement of the galvanic potential resulting from differences in the reduction potentials between two (reduction and oxidation) half cell reactions. The galvanic potential reflects the electrical free energy of the spontaneous redox process. The galvanic cell was constructed by immersing a zinc (Zn) electrode into 10 mL of a 1 M ZnSO_4 solution to form one half cell. The other half cell was comprised of a polished Pt wire immersed in a pH=14 electrolyte containing $\text{Au}(\text{OH})_4^-$, obtained by the addition of 250 μL of HAuCl_4 (0.025M) to 10 mL of a concentrated NaOH bath. The two half cells were connected with a salt bridge to enable ion flow between them, and the galvanic potential was measured between the two electrodes with a high impedance digital volt meter.

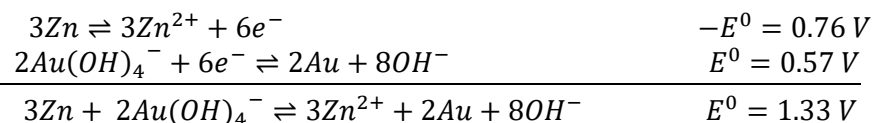
Prior to this measurement, control experiments were carried out to verify the experimental methodology. As a control experiment, the cell potential of two half cell reactions comprised of a silver wire immersed in 10 mL of 1 M AgNO_3 and a zinc electrode in 10 mL of 1 M ZnSO_4 was measured with the same apparatus and yielded a galvanic potential of $E=1.56$ V. The expected redox half reactions of silver and zinc are:



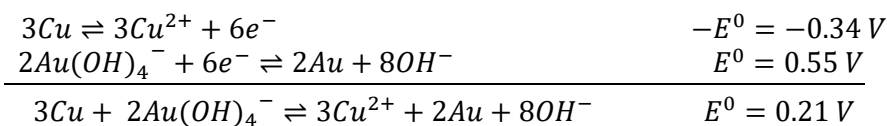
From the measured cell potential, and assuming the oxidation potential of Zn is 0.76 V under the standard experimental conditions employed for the measurement, the redox potential of Ag^+/Ag^0 is calculated to be 0.8 V, in agreement with the standard reduction potential of silver ions to silver metal. The reduction potential of silver ions was also measured by replacing ZnSO_4 with a Cu electrode immersed in 1M CuSO_4 and the same result was obtained. Finally, galvanic cells made from two half-cells with $\text{Au}(\text{OH})_4^-$ - ZnSO_4 and $\text{Au}(\text{OH})_4^-$ - CuSO_4 were built and the cell potentials of 1.33 V and 0.21 V were recorded respectively. The redox potential of the gold hydroxide complex $\text{Au}(\text{OH})_4^-$ was calculated after considering the shifts of the cell potential due to the concentration of $\text{Au}(\text{OH})_4^-$ ($[\text{Au}(\text{OH})_4^-] = 625 \mu\text{M}$) through the Nernst equation:

$$E = E^0 - \frac{0.059}{n} \log Q$$

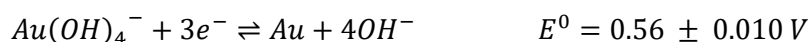
where E is the cell potential, E^0 is the cell potential under standard conditions, n is the number electrons transferred, and Q is the redox reaction quotient. The calculated redox potential of $Au(OH)_4^-$ was measured to be 0.57 V for the galvanic cell comprised of $Au(OH)_4^-$ - $ZnSO_4$ half-reactions:



and 0.55 V for the galvanic cell operating with $Au(OH)_4^-$ - $CuSO_4$ half-reactions:



These results yield a standard reduction potential



demonstrating that under high alkalinity conditions, the formation of $Au(OH)_4^-$ complexes leads to a dramatic decrease of the Au^{3+} complex ion reduction potential. While this is, in principle, a sufficient decrease in reduction potential to prevent galvanic replacement, the effects of the alkaline environment on oxidation of the silver substrate must also be considered. Determination of the oxidation potential of the Ag substrate in high alkalinity environments by the standard methods employed above are prevented by the oxidation of hydroxide ions



which occurs at lower potentials than that required to oxidize the substrate.

We have investigated the effect of OH^- ions on the oxidation of Ag, by constructing a 3 electrode cell made from a monocrystalline Ag(100) working electrode (WE), a Pt wire counter electrode (CE), and a Ag/AgCl reference electrode (RF). Cyclic voltammetry (CV) of the Ag(100) substrate was performed in a 1 M NaOH solution at room

temperature [Figure 26]. On the positive scan, two anodic peaks labelled A_1 and A_2 appear and during the negative scan, the cathodic peaks labelled C_1 and C_2 are observed.

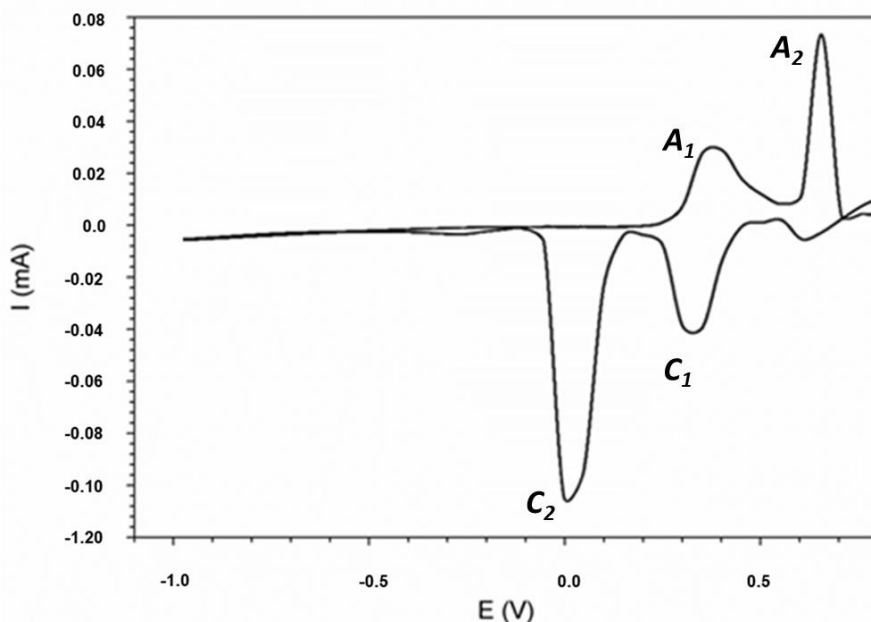
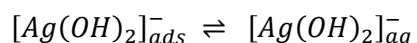
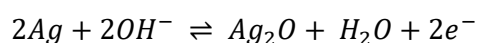


Figure 26. CV scan of Ag(100) WE in 1 M NaOH solution (scan rate 50 mV/s) measured with respect to a Ag/AgCl reference electrode.

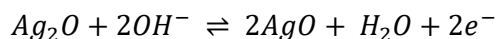
The appearance of anodic peaks in the forward CV scan have also been reported by M. A. Amin and co-workers, who have investigated the redox behaviour of polycrystalline Ag substrates in alkaline electrolytes.¹³ The lowest potential oxidation process (a low potential oxidation shoulder on A_1) has been assigned to the electroformation of soluble $Ag(OH)_2^-$ complex species:¹³



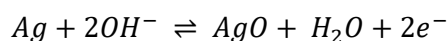
The anodic oxidation peak A_1 is thought to result from electroformation of Ag_2O resulting initially from the precipitation of $[Ag(OH)_2]_{aq}^-$ and subsequently from nucleation and growth via:



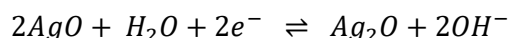
The anodic peak A_2 has been attributed to the electrooxidation of Ag_2O and the formation of AgO :



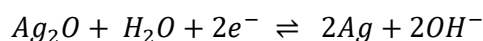
and/or the direct oxidation of Ag to AgO :



The cathodic peak C_1 is ascribed to the electroreduction of AgO to Ag_2O according to



while C_2 is attributed to reduction of Ag_2O to Ag :



The CV measurements demonstrate a quasi-reversible voltammogram. On this basis, the redox potential of silver can be estimated by:

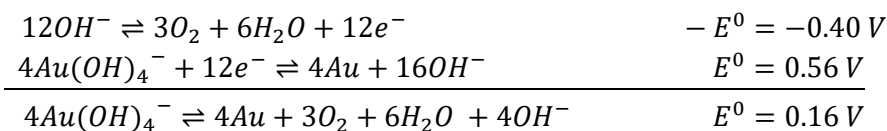
$$E_{1/2} = \frac{A_1 + C_1}{2}$$

Once corrected for the $Ag/AgCl$ reference electrode (0.200 V relative to RHE) and for the pH dependence of the RHE, the oxidation potential of Ag under pH 14 conditions with respect to the reversible hydrogen electrode is:

$$E_{1/2} + 0.059 \times pH + 0.200 V_{Ag/AgCl \rightarrow SHE} = 1.40V$$

Thus, in addition to producing a significant decrease in the reduction potential of Au^{3+} complex ions, the highly alkaline environment also introduces an additional barrier to oxidation of the silver substrate, making galvanic replacement an unlikely process in the highly alkaline electroless deposition bath.

In addition to providing a method to halt galvanic replacement, hydroxide ions also play another key role in the electroless deposition process: they provide a source of electrons to act as a reducing agent. The high concentration of hydroxide ions provide a readily available and uniformly distributed source of electrons capable of reducing $Au(OH)_4^-$, leading to the spontaneous formation of high quality Au thin films:



To gain a better understanding of how the Au growth proceeds and to determine when the surface of the Ag(100) substrate was completely covered with a uniform layer Au metal, a series of Ag(100) substrates were used as substrates for the electroless deposition of Au deposited over a range of deposition times ranging from 60 minutes to 30 seconds. The thickness of the deposited Au films was also measured for every deposition time using the cross-sectional SEM method, where an area of the substrate was removed using FIB milling to expose the different layers of materials. The SEM images of Au deposited at 30 s are shown in Figure 27. The thickness of the Au film at this short deposition time could not be measured accurately with the described technique due to the limited resolution of the SEM, however estimation was made by measuring the height of regions where Au layers appeared to merge (Figure 27d).

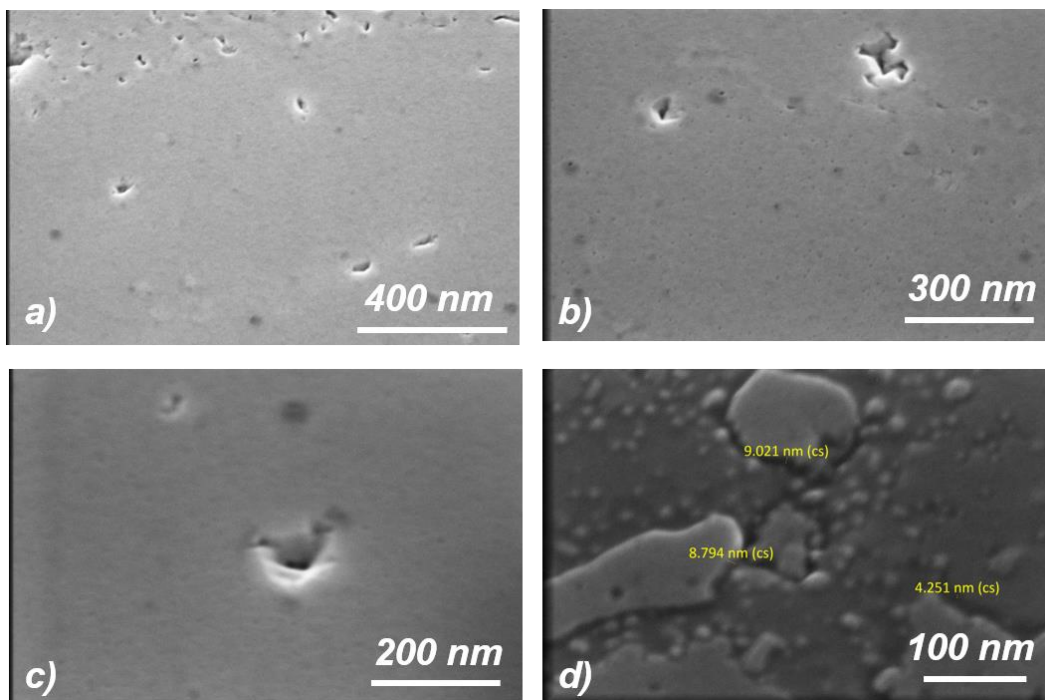


Figure 27. Electroless deposition of Au for 30 s. a)-c) are SEM images at different magnifications and d) is a tilt view SEM image showing Au nucleation at many positions on the growing film taken at 40° tilt angle.

The SEM images shown in Figure 27 suggest that the nucleation of Au takes place everywhere on the surface of the Ag(100) substrate, leading to uniform growth even at deposition times as short as 30 s. Note that this type of nucleation and growth is not observed for Au deposited via physical vapour deposition on typical substrates such as silicon, where Au does not wet the substrate well, and where polycrystalline island formation and coalescence yield nonuniform film growth. In contrast, the electroless deposition method described here appears to benefit from relatively rapid film growth in the plane of the substrate relative to that normal to the substrate, presumably due to effective surface wetting and access to readily available reducing agent (OH^-).

The nature and quality of Au deposition is also expected to be governed by the rates of growth on different crystalline facets of the growing crystalline film, determined by the availability of surface sites and the rate of reduction of the $\text{Au}(\text{OH})_4^-$ ions on the different facets. Thermodynamic arguments would suggest that growth of Au should be fastest in the $\langle 111 \rangle$ direction since it has the lowest surface energy ($E_{\langle 111 \rangle} < E_{\langle 100 \rangle} < E_{\langle 110 \rangle}$)¹⁴. However, our observations indicate that the lateral growth of Au (along the $\langle 110 \rangle$ direction) appears to dominate, giving rise to ultrasmooth films with uniform coverage even after relatively short deposition times (Figure 28).

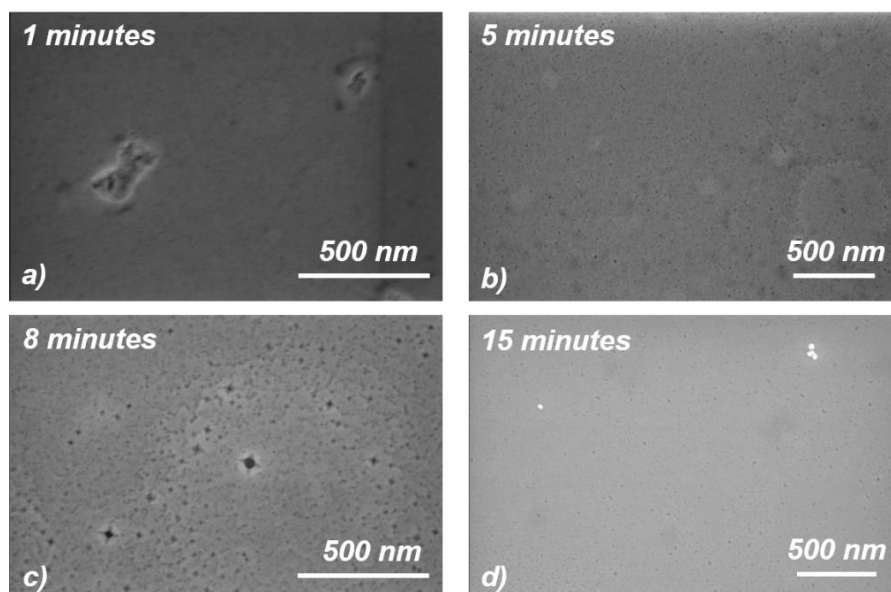


Figure 28. SEM images of deposited Au after a) 1 minute, b) 5 minutes, c) 8 minutes and d) 15 minutes of deposition.

One possible explanation for the most rapid growth rate being in the family of $\langle 110 \rangle$ directions (*i.e.* lateral to the surface) is the favourable interaction between hydroxide ions that comprise the $\text{Au}(\text{OH})_4^-$ and the (110) facets (step edges) of the growing film. DFT calculations of the energies of interaction of various ions with the low index facets of Au show OH^- adsorption affinities that are largest for (110) facets ((110) \rangle (100) \rangle (111)), resulting in the stabilization of Au-containing hydroxide ion complexes on those surfaces¹⁵. This preferential adsorption of OH^- on Au (hkl) surfaces may explain why the growth rate tends to favour the $\langle 110 \rangle$ direction, and would imply that the rate limiting step in the growth process is surface adsorption of the $\text{Au}(\text{OH})_4^-$ complex to the underlying substrate. More discussion on Au growth behaviour is provided in later chapters where the shapes of Au nanostructures is shown to be governed by the relative kinetics of growth on different facets. A deeper understanding of the growth mechanism of Au is important and of great interest to our research group, however it falls outside of the scope of this thesis. Further insight into the Au growth mechanisms could be provided by experiments involving *in situ* STM with a fast frame camera to record the growth of the Au crystalline facets in real time. Further additional work could involve measuring the reduction potential of Au on Au(111) and Au(110) surfaces in a hydroxide rich deposition bath to help shed light on this observed growth behaviour.

The thickness of Au for nine different samples deposited at three different deposition times was measured by cross-sectional SEM, as described above, and is shown in Figure 29. These Au films were all deposited on a $1 \times 1 \text{ cm}^2$ Ag(100) substrates where the sample was submerged in 10 mL of 1.0 M NaOH solution containing $625 \mu\text{M}$ HAuCl_4 while the temperature was maintained at 70°C by a water bath. The purpose of this experiment was to determine the reproducibility of film quality and thickness.

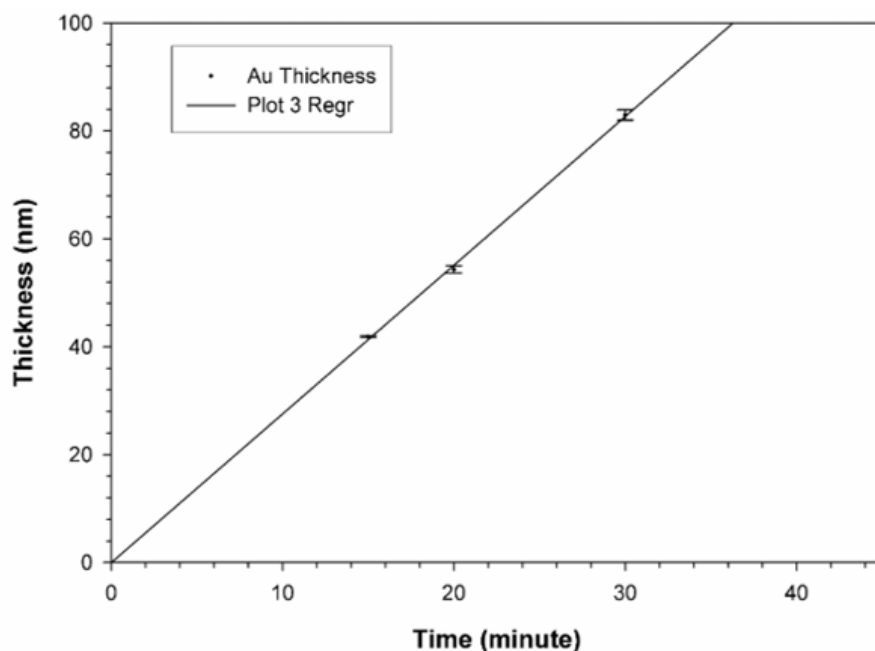


Figure 29. Thickness of the Au film as a function time for 15 minutes, 20 minutes and 30 minutes was shown.

The results in Figure 29 illustrate that the growth of Au on Ag(100) shows high reproducibility for each deposition time and that a linear correlation between deposition time and film thickness may be used to produce films of desired thickness. It should be noted that this correlation is only relevant for the given deposition conditions specified above and that by changing the temperature and/or the concentration of the species in the deposition bath, a new thickness calibration curve must be generated.

To determine the limits of the correlation displayed in Figure 29, seven additional Au samples were prepared as described, each with a different deposition time. The thickness of the films was measured using the cross-sectional SEM method [Figure 30]. Film thickness measurements for films deposited for shorter periods (such as those described above in Figures 27 and 28) are not included in this comparison because of the limited resolution of the SEM measurement method. Alternative methods such as HRTEM and STM could be used to determine film thickness accurately at short deposition times. Nevertheless, the rapid lateral growth behaviour described earlier leads one to believe that this correlation should persist down to the few monolayer limit.

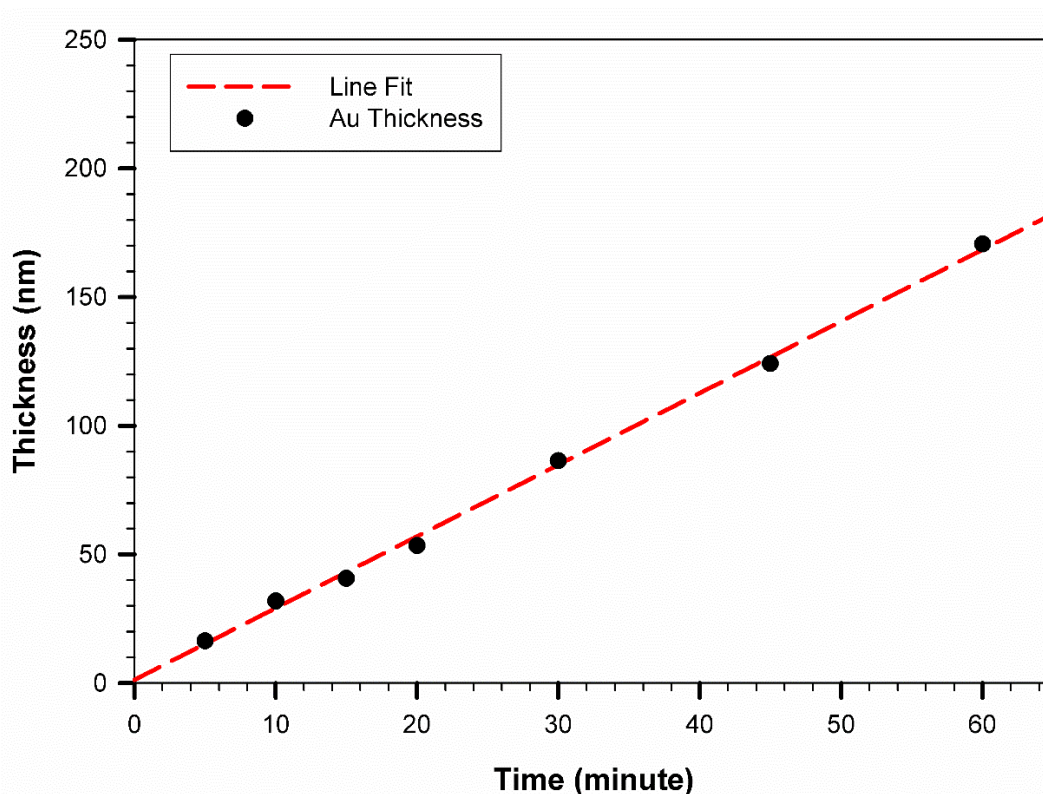


Figure 30. Measured Au film thickness versus deposition time for films deposited under the same conditions.

In this Chapter, we have described a novel approach to deposit Au films from an electroless deposition bath. The chemistry involved with this deposition process can be extended to the deposition of other metals (noble and otherwise). As part of the development of this chemistry, we have also demonstrated that metals such as Platinum (Pt), Palladium (Pd), Iridium (Ir), Copper (Cu), Ag, Ruthenium (Ru), Cobalt (Co) and Mercury (Hg) can be reduced using this or similar electrochemical bath compositions. In cases where single crystal Ag is used as a substrate, the deposited film shows preference for growth with the same crystalline orientation as the underlying Ag film. Due to the similarity of lattice constants to Ag, metals such as Pt, Pd, Ir and Ru, can be grown as epitaxial, single crystal films, whereas Cu and Co demonstrate oriented growth with the appearance of grain boundaries on the deposited films. This chemistry has also led to the deposition of some single crystal bi-metallic and ternary alloys through the co-reduction of two or more types of metal ions contained in the alkaline deposition bath. It

is envisioned that this chemistry can and will be extended to many such systems in order to enable new electrical, optical, catalytic and other properties of the deposited films. The detailed study of these new films is beyond the scope of this thesis, but will benefit from the studies described herein.

The next three chapters of this thesis describe studies carried out on the electrodeless deposition of Au and are presented in the format of manuscripts that have been prepared for submission to Nature Nanotechnology, JACS and ACS Photonics, respectively.

References

1. Schlesinger, M., Paunovic, M. & Paunovic, M. *Modern Electroplating*. (Wiley, 2011).
2. Davey, W. P. Precision Measurements of the Lattice Constants of Twelve Common Metals. *Phys. Rev.* **25**, 753–761 (1925).
3. Finkelstein, N. P. & Hancock, R. D. A new approach to the chemistry of gold. *Gold Bull* **7**, 72–77 (1974).
4. Baes, C. F. *The hydrolysis of cations / Charles F. Baes, Jr., Robert E. Mesmer*. (Wiley, 1976).
5. Mironov, I. Properties of Gold(III) Hydroxide and Aquahydroxogold(III) Complexes in Aqueous Solution. *Russian Journal of Inorganic Chemistry* **50**, 1115 (2005).
6. Cherevko, S., Kulyk, N. & Chung, C.-H. Nanoporous Pt@AuxCu100–x by Hydrogen Evolution Assisted Electrodeposition of AuxCu100–x and Galvanic Replacement of Cu with Pt: Electrocatalytic Properties. *Langmuir* **28**, 3306–3315 (2012).
7. Tsuji, M. *et al.* Synthesis of Pt–Ag alloy triangular nanoframes by galvanic replacement reactions followed by saturated NaCl treatment in an aqueous solution. *Materials Letters* **121**, 113–117 (2014).
8. Li, W., Kuai, L., Chen, L. & Geng, B. “Re-growth Etching” to Large-sized Porous Gold Nanostructures. *Scientific Reports* **3**, 2377 (2013).

9. Djokić, S. S. & Cadien, K. Galvanic Deposition of Silver on Silicon Surfaces from Fluoride Free Aqueous Solutions. *ECS Electrochem. Lett.* **4**, D11–D13 (2015).
10. Djokić, S. S., Antić, Ž., Djokić, N. S., Cadien, K. & Thundat, T. Galvanic Processes on Silicon Surfaces in Cu(II) Alkaline Fluoride-Free Solutions. *J. Electrochem. Soc.* **163**, D651–D654 (2016).
11. Djokić, S. S., Antić, Ž., Djokić, N. S. & Thundat, T. Communication—Galvanic Deposition of Gold on Silicon from Au(I) Alkaline Fluoride-Free Solutions. *J. Electrochem. Soc.* **163**, D818–D820 (2016).
12. Sayed, S. Y. *et al.* Heteroepitaxial Growth of Gold Nanostructures on Silicon by Galvanic Displacement. *ACS Nano* **3**, 2809–2817 (2009).
13. Rehim, S. S. A. E., Hassan, H. H., Ibrahim, M. A. M. & Amin, M. A. Electrochemical Behaviour of a Silver Electrode in NaOH Solutions. *Monatshefte fuer Chemie* **129**, 1103–1117 (1998).
14. Xia, Y., Xiong, Y., Lim, B. & Skrabalak, S. E. Shape-Controlled Synthesis of Metal Nanocrystals: Simple Chemistry Meets Complex Physics? *Angew. Chem. Int. Ed.* **48**, 60–103 (2009).
15. Pessoa, A. M., Fajín, J. L. C., Gomes, J. R. B. & Cordeiro, M. N. D. S. Ionic and radical adsorption on the Au(hkl) surfaces: A DFT study. *Surface Science* **606**, 69–77 (2012).

Scalable Green Synthesis of Monocrystalline Noble Metal Nanostructures for Low-Loss Plasmonic and Nanophotonic Applications

Authors' contributions:

S.V.G. and G.W.L conceived and designed the experiments, S.V.G. performed all film deposition, characterization, and nanofabrication experiments, F.C.M. developed the methodology and fabricated single crystal silver substrates, X.Z. performed the TEM experiment and analysis, S.K. performed laser scanning 2PPL microscopy experiments and analyses, G.W.L. wrote the manuscript with input from all.

4. Scalable Green Synthesis of Monocrystalline Noble Metal Nanostructures for Low-Loss Plasmonic and Nanophotonic Applications

Sasan V. Grayli, Xin Zhang, Finlay C. MacNab, Saeid Kamal, Gary W. Leach*

Department of Chemistry, Laboratory for Advanced Spectroscopy and Imaging Research, and 4D LABS, Simon Fraser University, 8888 University Dr., Burnaby, BC V5A 1S6 Canada

The confinement of spatially extended electromagnetic waves to nanometer-scale metal structures can be harnessed for application in information processing and energy harvesting, enable negative refractive index and subwavelength resolution through engineered metamaterials, and promises new technologies that will operate in the quantum plasmonics limit. However, the deposition of high-definition single crystal subwavelength metal nanostructures required for the practical realization of these promising applications remains a significant hurdle. Here, we introduce a new scalable, green, wet chemical approach to monocrystalline noble metals that enables the fabrication of ultrasmooth, epitaxial, single crystal films ideal for the *subtractive* manufacture of nanostructure through ion beam milling, and *additive* crystalline nanostructure via lithographic patterning to enable large area, single crystal metamaterial arrays and high aspect ratio nanowires. Our single crystal nanostructures display significantly improved feature quality, highly tailored localized fields, and greatly improved stability compared to polycrystalline structures, enabling new practical advances at the nanoscale.

High quality monocrystalline metal thin films and nanostructures are critical building blocks for next generation nanotechnologies.¹ The immense and growing

interest in nanostructured metal surfaces results from their ability to support surface plasmons (SPs) that concentrate light below the diffraction limit providing a bridge between high bandwidth photonic fiber-based technology and the nanometer-scale structures that comprise current integrated circuitry.² SPs are characterized by ultrafast response and can mediate rapid photon-to-hot electron conversion which can be exploited for new solar energy, photosensor, and photocatalyst applications.³⁻⁶ Engineered metamaterials can provide negative refractive index^{7,8}, subwavelength resolution^{9,10}, and field manipulation,¹¹⁻¹³ enabling diffraction-free imaging and pattern transfer. Improvements in nanoscale fabrication methods, in principle, now offer design flexibility and structure generation with the ability to manipulate the local photonic density of states and to control light–matter interactions at the quantum level¹⁴⁻¹⁶. Plasmonic near fields can significantly enhance light–matter interactions with quantum emitters, providing the opportunity to engineer radiative rates and enhance scattering efficiencies. Quantum emitters confined to metallic nanocavities display strong dipole coupling, with the prospects of single-molecule sensing, nanoscale light sources, single-photon emitters, and all-optical transistors.^{17,18}

These applications place stringent requirements on surface quality in defining local fields and field enhancements, as well as the nanometer-level positional and orientational control of emitters with respect to surface features. In practice, plasmonic metals deposited by conventional methods (e.g. physical vapour deposition) are characterized by polycrystalline morphologies comprised of grain boundaries, defects, and other material imperfections that act as local scattering sites, sources of increased optical absorption loss, dissipative damping, and positional uncertainty. They compromise pattern transfer fidelity and limit functional performance.^{19,20} Likewise, strategies that employ the synthesis of solution-grown nanocrystals suffer from the major challenge of placing them in desired locations onto substrates with high fidelity, and the additional barrier associated with surfactants and nanocrystal capping agents necessary to prevent particle aggregation and agglomeration, but that prevent direct electrical contact to the nanoscale structures. In order to exploit the local electromagnetic fields of noble metal nanostructures fully, improved control over surface quality and chemistry is imperative. While this has remained a significant challenge in the field and has led to growing efforts to identify alternative low-loss materials for

plasmonic and metamaterial applications²¹, their high carrier concentrations with visible and near infrared optical responses remain extremely attractive and continue to foster new strategies to exploit noble metal-based plasmonics. Here we describe a new, green approach to monocrystalline noble metal plasmonic structures that is based on the deposition of noble metals from solutions of their commonly available salts (Fig. 31).

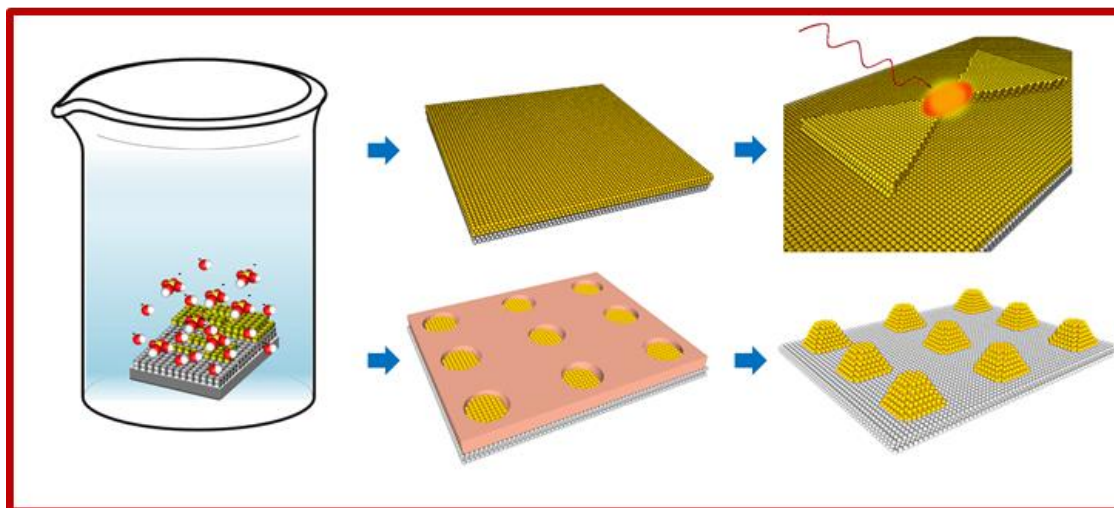
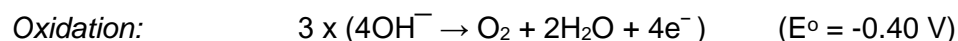
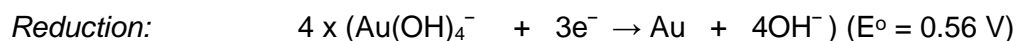


Figure 31. Epitaxial electrochemical deposition of monocrystalline noble metals for low-loss plasmonic, nanophotonic, and nanoelectronics applications. Left: Solution phase reduction of $\text{Au}(\text{OH})_4^-$ ions to Au atoms at the Ag(100)/aqueous alkaline electrolyte interface. Upper Central: Deposition of a uniform, ultrasmooth, epitaxial, single crystal Au(100) film of controlled thickness. Upper Right: Excitation of a bowtie nanoantenna fabricated via FIB milling of the single crystal Au film. Lower Central: Solution phase deposition of Au into pores formed by patterning a PMMA resist layer provides an oriented crystalline nanostructured metamaterial array.

Aqueous solutions of gold salts (e.g. HAuCl_4) contain hydrated Au(III)-based complex ions (e.g. AuCl_4^-) whose standard reduction potentials ($\text{AuCl}_4^- + 3\text{e}^- \rightarrow \text{Au} + 4\text{Cl}^-$; $E^\circ = 1.00$ V) are greater than that of silver ($\text{Ag}^+ + \text{e}^- \rightarrow \text{Ag}$; $E^\circ = 0.80$ V). Reduction of Au^{3+} to Au in the presence of silver typically proceeds spontaneously by galvanic replacement, in which Au^{3+} ions are reduced, but at the expense of silver atom oxidation, resulting in porous, polycrystalline gold and gold/silver alloy materials. This chemistry has been exploited to yield hollow colloidal nanostructures with tunable and controlled properties for application in plasmonics, photocatalysis, and nano-medicine,²²

and more recently it has been demonstrated that control over the relative rates of galvanic replacement and Au³⁺-complex ion reduction in the presence of organic acid reducing agents can provide core-shell colloidal nanocrystals containing thin epitaxial layers of gold.^{23,24} However, the ability to affect noble metal ion reduction without galvanic replacement, over large surface areas, with thickness control, and with nanometer-scale patterning capability, would provide a new level of control over surface nanostructure and open new opportunities for practical implementation of novel nanometer-scale technologies.

Here we describe the reduction of Au³⁺-complex ions in highly alkaline environments in the absence of other reducing agents to yield the controlled epitaxial deposition of Au onto large area single crystal Ag(100) substrates. Under strongly alkaline conditions, two important effects suppress galvanic replacement. At high pH, OH⁻ ions displace the Cl⁻ ligands of the AuCl₄⁻ complexes leading to the formation of Au(OH)₄⁻ ions²⁵, whose redox potentials are lowered to 0.56 V (supplementary materials). This is considerably lower than the silver reduction potential under non-alkaline conditions. Simultaneously, surface hydroxide residing at the Ag/electrolyte interface under highly alkaline conditions presents a significant additional barrier to surface oxidation, arresting galvanic replacement. The available low energy surface oxidation processes under these alkaline conditions have been attributed²⁶ to the electroformation of soluble [Ag(OH)₂]⁻ and the growth of Ag₂O which appears at redox potentials of 1.40 V (supplementary materials). In the absence of silver substrate oxidation, gold ion reduction can then proceed spontaneously through readily available hydroxide ions in the absence of other reducing agents:



The highly alkaline conditions provide a high concentration and uniform distribution of hydroxide ions that leads to uniform noble metal ion reduction, affording large area metal deposition. Note that electrochemical deposition of noble metals typically involves electrolyte baths that contain highly toxic complexing agents and bath

additives designed to improve metal deposition characteristics.²⁷ In contrast, our chemistry affords large area uniform gold deposition without the use of toxic additives, employing only alkaline conditions which can later be removed through bath neutralization to yield water. Metal deposition rates and film thickness can be tuned by control over reduction kinetic parameters including metal salt concentration, deposition temperature, and deposition time. Further, the chemistry can be carried out at the wafer level, and therefore represents a scalable pathway to single crystal noble metal nanostructure.

Solution phase Au deposition from *uncontrolled* pH H₂AuCl₄ solutions onto single crystal Ag(100)/Si(100) substrates leads to the deposition polycrystalline gold and concomitant silver film oxidation, consistent with the AuCl₄⁻-induced galvanic replacement mechanism. Two-dimensional X-ray diffraction (2D-XRD) patterns display (111), (200), and (220) Au diffraction arcs characteristic of polycrystalline metal deposition (Fig. 32a). In contrast, electroless Au deposition from high alkalinity (pH 14) H₂AuCl₄ solutions onto Ag(100)/Si(100) substrates display well-defined Au(200) diffraction spots and an absence of diffraction arcs, characteristic of oriented, substrate-aligned crystalline metal deposition (Fig 32b). Solution-deposition onto (Ag(100)/Si(100)) single crystal silver substrates under high alkalinity conditions results in uniform, large area, ultra-smooth Au surfaces (Fig 32c). Physical vapor deposition (PVD) of gold onto Si(100) substrates with a 5nm Cr adhesion layer (a typical PVD-based deposition method) results in polycrystalline gold island growth and coalescence into thin gold films that are far less uniform by comparison (Fig. 32d). Transmission electron microscopy (TEM) provides evidence of the nature of the gold deposition from solution. Elemental mapping (Fig. 32(e)-(h)) reveals the deposition of a well-defined, dense, uniform gold layer atop the Ag(100)/Si(100) single crystal substrate rather than a porous Au/Ag alloy film, confirming that under high alkalinity conditions, gold ion reduction does not occur through Ag substrate oxidation and galvanic replacement. High resolution transmission electron microscopy (HRTEM) and selected area electron diffraction (SAED) images of the Ag/Au interface region (Fig 32(i)-(l)) demonstrate that under these high alkalinity conditions, gold deposition occurs epitaxially, resulting in a well-defined interface region with alignment of the deposited Au film atoms with those of the underlying single crystal silver substrate.

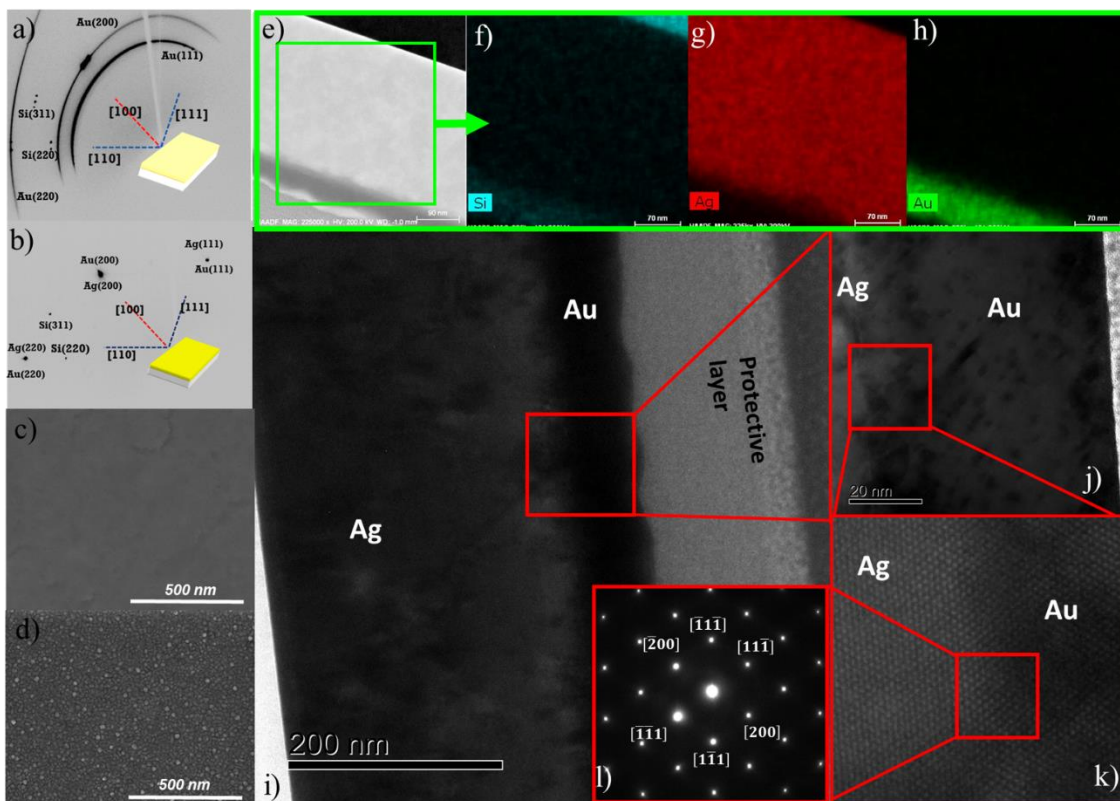


Figure 32. (a) 2D-XRD of gold deposited from an uncontrolled pH HAuCl_4 solution onto a $\text{Ag}(100)/\text{Si}(100)$ single crystal substrate. (b) 2D-XRD of gold deposited from a pH 14 HAuCl_4 solution onto a $\text{Ag}(100)/\text{Si}(100)$ single crystal substrate. (c) Top view SEM of a 100 nm thick gold film deposited from pH 14 HAuCl_4 solution onto a $\text{Ag}(100)/\text{Si}(100)$ single crystal substrate. (d) Top view SEM of a 100 nm thick Au film evaporated onto an atomically flat $\text{Si}(100)$ substrate with a 5nm Cr adhesion layer. High resolution transmission electron microscopy of pH 14 solution-deposited, 70 nm thick Au film onto a $\text{Ag}(100)/\text{Si}(100)$ single crystal substrate: (e) TEM cross section image of protective Pt-overlayer/ $\text{Au}(100)/\text{Ag}(100)/\text{Si}(100)$ with Pt appearing in the lower left and silicon wafer appearing dark in the upper right hand region of the image. (f)-(h) Elemental mapping of the $\text{Au}(100)/\text{Ag}(100)/\text{Si}(100)$ structure (silicon upper right). (i) Cross-sectional TEM image of the Pt / $\text{Au}(100)/\text{Ag}(100)$ interface region. (j) Expanded view of the $\text{Au}(100)/\text{Ag}(100)$ interface. (k) The $\text{Au}(100)/\text{Ag}(100)$ interface showing alignment of atomic planes across the interface. (l) Selected area electron diffraction from the region highlighted in (k) viewed along the $[011]$ zone axis.

The utility of this chemistry and some of its advantages over conventional physical vapor deposition-based methods are demonstrated in Figure 33. Focused ion beam (FIB) milling has been used to fabricate Au nanostructures from solution-deposited single crystal epitaxial films and from the polycrystalline PVD-deposited Au films described above. Without exception, the pattern transfer fidelity and structure definition of our solution-deposited single crystal films are far superior to conventional polycrystalline PVD-deposited films. Anisotropic, crystal direction-dependent ion milling rates in polycrystalline films yield non-uniform structures that reduce pattern transfer quality and that act as local scattering centers for electronic, photonic and plasmonic excitations. Four point probe transport measurements of these 100 nm-thick gold films show that single crystal solution-deposited films yield sheet resistances greater than 20 times below those of PVD-deposited polycrystalline films of the same thickness (supplementary materials). Spectroscopic ellipsometry performed on 100 nm thick Au films show that optical absorption losses in the single crystal films are significantly reduced compared to those of the polycrystalline PVD-deposited films (supplementary materials).

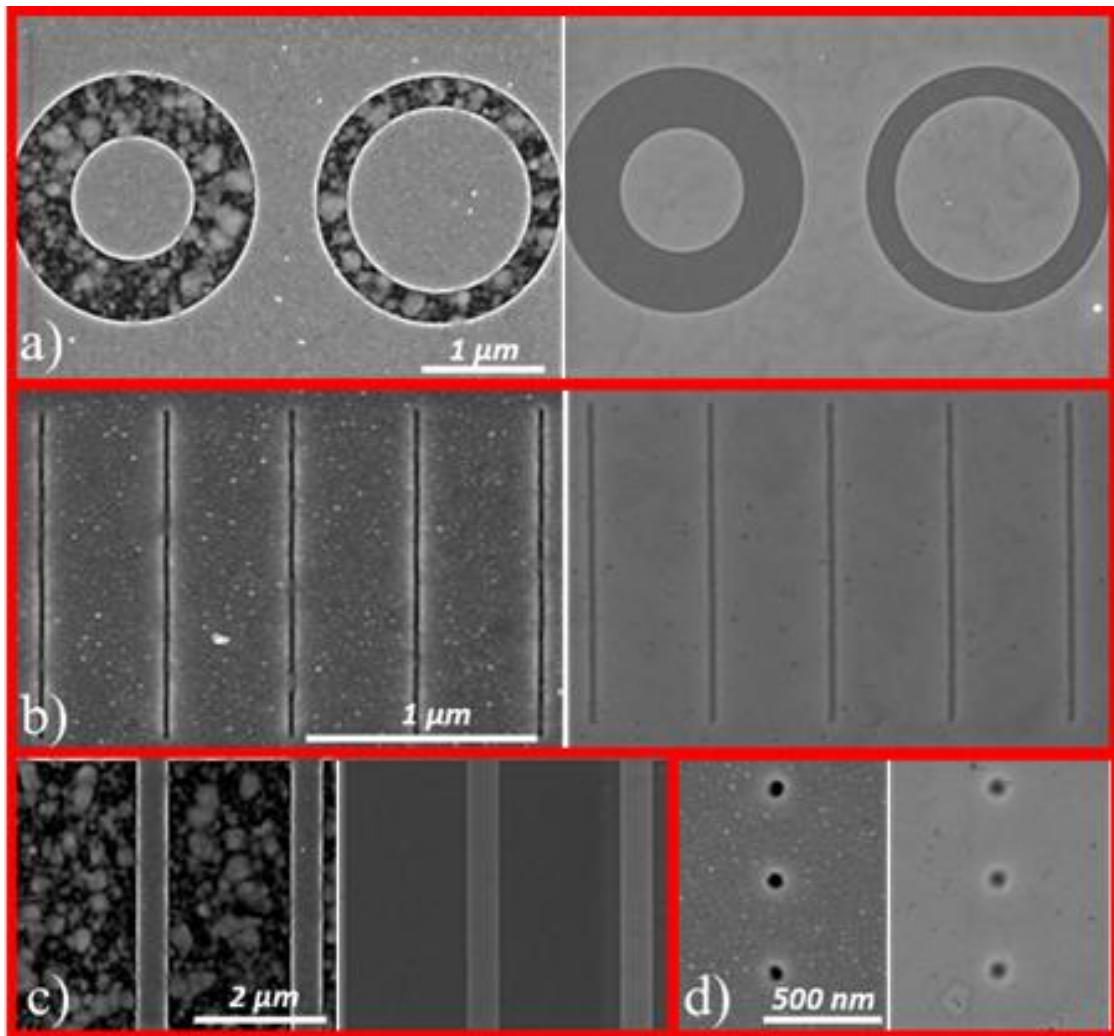


Figure 33. Focused ion beam milling of 100 nm thick, polycrystalline, PVD-deposited Au nanostructures and monocrystalline, solution-deposited Au nanostructures. SEM images of (a) ring resonator structures from polycrystalline, PVD-deposited Au (left) and solution-deposited Au (right), (b) 30 nm wide lines in PVD-deposited Au (left) and solution-deposited Au (right), (c) patterned windows in PVD-deposited Au (left) and solution-deposited Au (right), (d) 90 nm diameter holes patterned in PVD-deposited Au (left) and solution-deposited Au (right).

We compare directly bowtie nanoantenna devices manufactured through FIB milling of monocrystalline and polycrystalline films (Fig. 34). These structures have stringent deposition and patterning requirements to yield precision structures that display uniform and reproducible local gap fields at the antenna's feed points. The

bowtie nanoantenna features were patterned with sequential FIB milling steps of rectangular and square features to yield bow tie gaps of 20 nm. This method of fabrication also highlights regions of the bowtie structures where there are metal step edges that result from this pattern generation scheme. SEM images of the structures show significantly higher quality pattern transfer and structure definition of the single crystal bowtie nanoantennas compared to polycrystalline devices fabricated identically (Figs 34(a)-(b)). Two-photon photoluminescence (2PPL) imaging has been used extensively to characterize the resonant behaviour of plasmonic nanostructures²⁸⁻³² and is used here (Fig. 34(c)-(g)) to provide insight into the nanoantenna plasmonic response and local field generation from the bowtie nanoantennas. The 2PPL maps of 3 x 3 bowtie arrays demonstrate that the fabrication yield of functional devices is greatly impacted by the material quality and associated pattern transfer characteristics. The yield of monocrystalline antennas is close to 100% as measured by the appearance of an enhanced local near-field resulting in 2PPL intensity at the antenna feed points and the uniformity of this 2PPL intensity for all nanoantennas (Fig 34c). Structures fabricated identically but with polycrystalline-deposited gold, show poor fabrication yield with fewer than 50% of the devices showing near-field intensity enhancements at the antenna feed points, and of these, no uniformity in 2PPL intensity (Fig 34d).

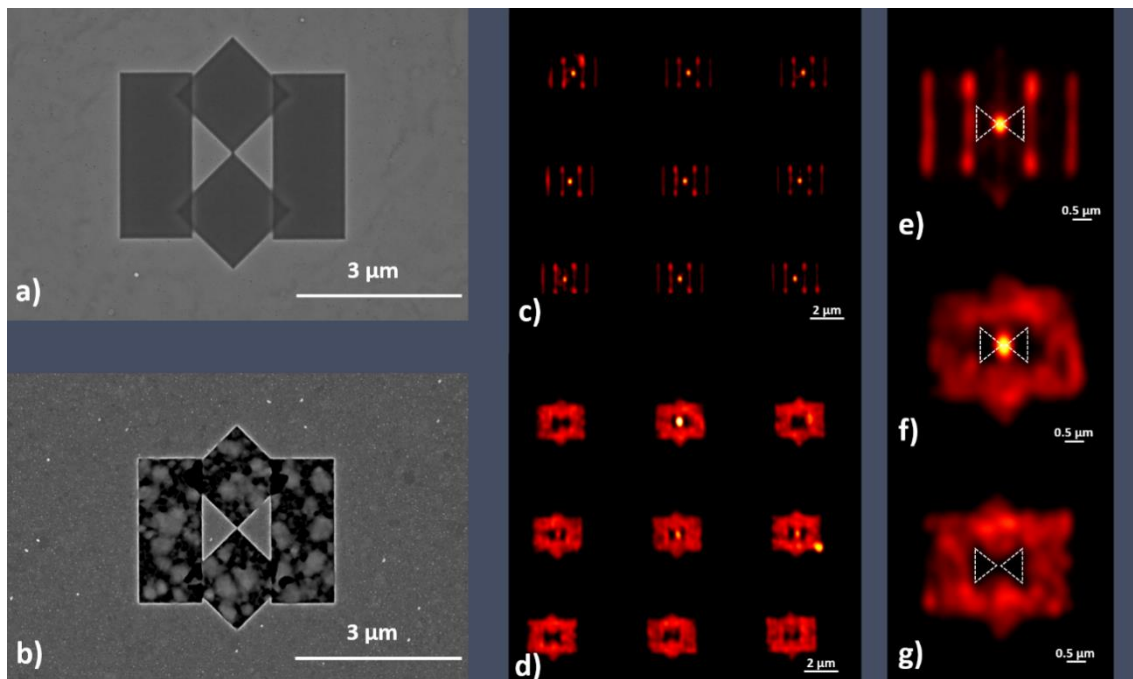


Figure 34. Single crystal versus polycrystalline bowtie nanoantenna fabrication and performance. SEM image of bowtie nanoantenna patterned by FIB milling of (a) solution-deposited Au(100) and (b) PVD-deposited polycrystalline Au films. Scanning laser microscope image of 2PPL (horizontally-polarized, 780 nm excitation, 120 fs pulse duration) of 3 x 3 bowtie nanoantenna arrays fabricated from (c) solution-deposited Au(100) and (d) PVD-deposited polycrystalline Au films. 2PPL image of (e) individual solution-deposited Au(100) nanoantenna and (f)-(g) individual PVD-deposited polycrystalline Au nanoantennas.

Our single crystal structures also afford superior ability to control and tailor local fields. The single crystal bowties show relatively uniform 2PPL intensity across all nanoantennas at the antenna feed points and in regions of the fabricated structure (Fig 34e) where sharp gold edges and discontinuities are formed due to the FIB pattern generation scheme. Polycrystalline bowties (Fig. 34(d),(f)-(g)), in contrast, show that two photon photoexcitation results in non-uniform plasmonic excitation over the entire milled area of the bowties due to structural inhomogeneity and grain boundary induced plasmon excitation and dissipation. In few cases do the polycrystalline structures yield enhanced near-fields at the antenna's feed points. Finally, our single crystal solution-deposited bowtie antennas demonstrate superior thermal and mechanical stabilities compared to their polycrystalline counterparts. Illumination of the bowtie antennas with

increasing incident illumination intensities results in higher intensity 2PPL emission (2PPL intensity is proportional to I^2 , where I is the local near-field intensity enhancement^{29,30}) until they are catastrophically damaged through photothermal-induced structural modification and rupture. Intensity dependent studies of the 2PPL from the bowtie structures indicate that the single crystal bowties can support more than one order of magnitude more incident illumination intensity (and therefore 10^4 local field enhancement) than the polycrystalline bowties before irreversible and catastrophic loss. We assert that this is a direct result of less local heat dissipation through grain boundary loss and increased thermal and mechanical stability of the single crystal structures compared to polycrystalline bowtie antennas.

Solution-deposited Au(100) bowtie devices fabricated through FIB milling demonstrate multiple advantages over their polycrystalline counterparts. Nevertheless, the broader integration of nanostructured elements into useful device structures requires cost effective, manufacturable strategies that provide large area patterning capability. Here we demonstrate the utility of this green chemistry with the use of electron beam lithography (EBL) to deposit large area arrays of single crystal noble metal nanostructures through additive patterning. Figure 35(a) shows a top view SEM image of a gold nanopillar array solution-deposited onto an e-beam patterned, solution-deposited Au(100) substrate: A 100 nm thick layer of PMMA A2 electron-beam resist is spin cast onto a solution-deposited Au(100) top surface. Following electron beam patterning and resist development, Au is deposited from solution into the 120 nm diameter, 550 nm period, cylindrical pores of the patterned resist layer by immersion into the noble metal salt-containing electrolyte used to obtain the underlying ultrasmooth Au(100) films. Following metal deposition, subsequent resist removal yields the patterned nanopillar array, demonstrating high quality pattern transfer. Single pillars (Fig. 35b) display octagonal side walls and top facets consistent with monocrystalline pillar deposition. 2PPL from the plasmonic Au(100) metamaterial array (Fig. 35(c)) shows pillar-resolved emission and demonstrates near-field plasmonic enhancement associated with each of the gold nanopillars. Fig. 35(d) demonstrates the compatibility of this chemistry with silver deposition. The top-view SEM image shows a faceted single silver nanopillar from a Ag nanopillar array deposited onto a Au(100) substrate

from a 1.0 M OH⁻ ion containing electrolyte bath prepared from AgNO₃, in a manner similar to that described for gold nanopillar deposition.

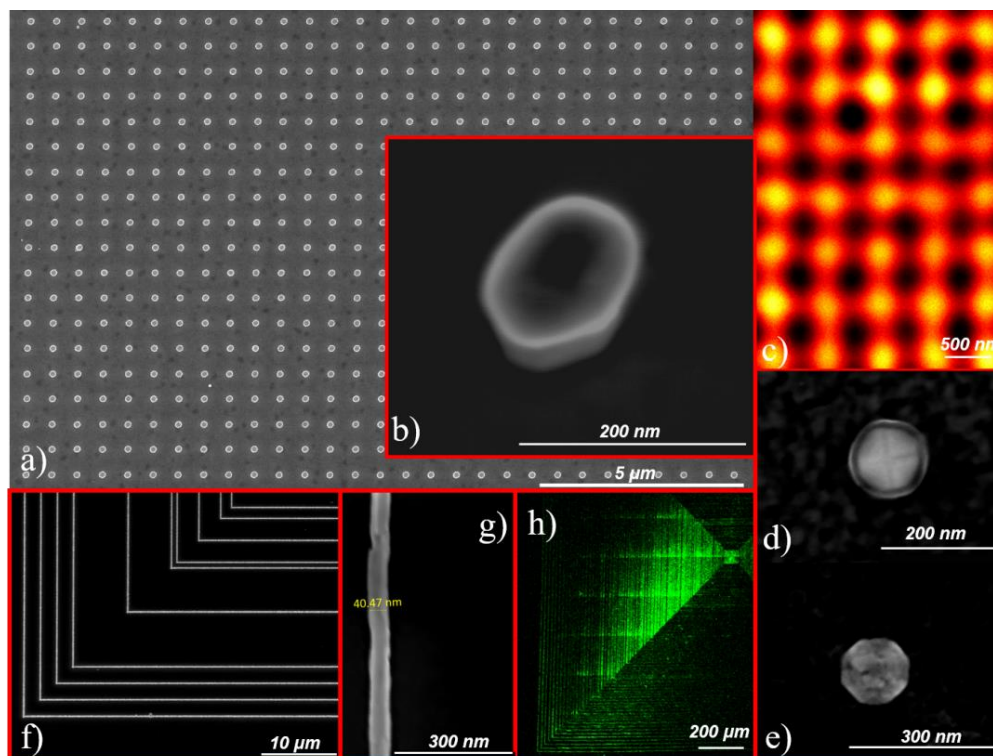


Figure 35. Additive patterning of single crystal metals through solution-deposition on EBL-patterned substrates. (a) SEM top view image of a large area crystalline Au nanopillar array with pillar diameter of 120 nm and period 550 nm, solution-deposited on an EBL-patterned, solution-deposited Au(100) substrate. (b) SEM 30° tilt view image of an individual gold nanopillar exhibiting crystalline facets. (c) Pillar-resolved 2PPL from the Au plasmonic metamaterial array. (d) SEM top view image of a crystalline silver nanopillar solution-deposited onto a solution-deposited Au(100) substrate, exhibiting well defined top facets. (e) SEM top view image of a faceted gold-capped silver nanopillar obtained by solution-deposition of 10 nm of Au onto a Ag(100) nanopillar array. (f) SEM top view image of high aspect ratio concentric square Au nanowire structures EBL-deposited from solution onto a Ag(100) substrate. (g) The wires appear continuous and are characterized by widths of 40 nm and lengths of 2 mm, limited by e-beam exposure and pattern dimension, respectively. (h) 2PPL image of the concentric square nanowire structure described in (f) excited by 800 nm light polarized horizontally, perpendicular to the vertical nanowire axes.

The high definition faceted structure implies successful silver-on-gold heteroepitaxial solution phase deposition. While silver structures are known to possess superior plasmonic properties to those comprised of gold, they suffer from chemical instability and ready oxidation under ambient conditions. Deposition of a thin, oxidation-resistant, gold overlayer can provide chemical resistance without significant perturbation to the plasmonic properties of the underlying silver structures. Figure 35(e) shows a top-view SEM image of a silver nanopillar with a thin (~10 nm) overlayer of gold. The image shows that the resulting core-shell nanopillar displays octagonal faceted structure suggesting epitaxial deposition and conformal gold coating of the silver pillar. We have also investigated the utility of this chemistry for the deposition of high aspect ratio gold nanowires. Shrinking feature size and increasing density of nanoscale circuit elements will benefit from low resistance monocrystalline structure to assist in the management of thermal budgets. Figure 35(f) shows the top-view SEM image of a portion of a concentric square Au nanowire array deposited onto a Ag(100) substrate by EBL patterning and solution phase deposition of Au, as described. Figure 35(g) shows the pattern transfer of these continuous nanowire structures with nominal widths of 40 nm. Together with typical lengths of 2mm, these features yield an aspect ratio $> 10^4$, with further improvements anticipated by electron beam dose optimization. The concentric square nanowire array also displays broadband plasmonic response. Figure 35(h) shows a 2PPL scanning laser microscope image of a portion of the nanowire array illuminated with horizontally polarized 800 nm light, perpendicular to the vertically oriented nanowire long axes. The image shows preferential emission from vertically oriented nanowires, consistent with short-axis polarized plasmonic excitation and two-photon photoluminescence. Likewise, excitation with vertically-polarized light preferentially excites horizontally oriented nanowires and results in polarized emission from regions containing horizontally oriented nanowires. Overall, the structure displays polarization-independent broadband absorption and emission characteristics.

In summary, we have developed a new scalable, green chemistry that enables the deposition of epitaxial, single crystal noble metal thin films and nanostructures from solution. The chemistry is compatible with both subtractive and additive patterning methods and shows high fidelity pattern transfer to generate single crystal structures over extended geometries. We demonstrate that single crystal bowtie nanoantennas

fabricated with this chemistry and focused ion beam milling show improved fabrication yield, greater control over local fields, and improved thermal and mechanical stability compared with polycrystalline structures patterned identically. The utility of this chemistry with additive lithographic patterning methods provide large area single crystal metamaterial arrays and high aspect ratio nanowire structures. We anticipate that this accessible and cost-effective approach will be broadly exploited to fabricate new single crystal structures with limited optical and resistive losses and unrivaled homogeneity over extended geometries, enabling new practical advances at the nanoscale.

References

- 1) A. I. Fernández-Domínguez, F. J. García-Vidal, & L. Martín-Moreno, Unrelenting plasmons, *Nat. Photon.* **11**, 8–10 (2017).
- 2) E. Ozbay, Plasmonics: Merging photonics and electronics at nanoscale dimensions, *Science* **311**, 189-193 (2006).
- 3) M. Moskovits, The case for plasmon-derived hot carrier devices, *Nat. Nanotechnol.* **10**, 6-8, (2010).
- 4) S. Linic, P. Christopher, & D. B. Ingram, Plasmonic-metal nanostructures for efficient conversion of solar to chemical energy. *Nat. Mater.* **10**, 911–921 (2011).
- 5) C. Clavero, Plasmon-induced hot-electron generation at nanoparticle/metal-oxide interfaces for photovoltaic and photocatalytic devices. *Nat. Photon.* **8**, 95–103 (2014).
- 6) M. L. Brongersma, N. J. Halas, & P. Nordlander, Plasmon-induced hot carrier science and technology, *Nat. Nanotechnol.* **10**, 25–34 (2015).
- 7) D. R. Smith, J. B. Pendry, & M. C. K. Wiltshire, Metamaterials and Negative Refractive Index, *Science* **305**, 788-792 (2004).

- 8) V. M. Shalaev, W. Cai, U. K. Chettiar, H.-K. Yuan, A. K. Sarychev, V. P. Drachev, & A. V. Kildishev, Negative index of refraction in optical metamaterials, *Opt. Lett.* **30**, 3356-3358, (2005).
- 9) X.Zhang, & Z. Liu, Superlenses to overcome the diffraction limit, *Nat. Mat.* **7**, 435-441 (2008).
- 10) D. Lu, & Z. Liu, Hyperlenses and metalenses for far-field super-resolution imaging, *Nat. Comm.*, DOI: 10.1038/ncomms2176 (2012).
- 11) J.B. Pendry, D. Schurig, & D.R. Smith, Controlling Electromagnetic Fields, *Science* **312**, 1780-1782, (2006).
- 12) U. Leonhardt, Optical conformal mapping. *Science* **312**, 1777–1780 (2006).
- 13) V. M. Shalaev, Transforming light. *Science* **322**, 384–386 (2008).
- 14) E. Altewischer, M. P. van Exter, & J. P. Woerdman, Plasmon-assisted transmission of entangled photons. *Nature* **418**, 304–306 (2002).
- 15) Z. Jacob, & V. M. Salaev, Plasmonics goes quantum. *Science* **334**, 463-464 (2011).
- 16) M.S. Tame, *et. al.* Quantum Plasmonics. *Nature Physics* **9**, 329-340 (2013).
- 17) R. Chikkaraddy, B. de Nijs, F. Benz1, S.J. Barrow, O.A. Scherman, E. Rosta, A. Demetriadou,
P. Fox, O. Hess, & J. J. Baumberg, Single-molecule strong coupling at room temperature in plasmonic nanocavities, *Nature*, **535**, 127-130 (2016).
- 18) P. Vasa, & C. Lienau, Strong Light–Matter Interaction in Quantum Emitter/Metal Hybrid Nanostructures, *ACS Photonics* **5**, 2–23 (2018).
- 19) J. B. Khurgin, How to deal with the loss in plasmonics and metamaterials. *Nat. Nanotechnol.* **10**, 2–6 (2015).
- 20) J. Krenn, Perspective on Plasmonics, *Nature Photonics* **6**, 714–715 (2012).

- 21) A. Boltasseva, & H. A. Atwater, Low-loss plasmonic metamaterials. *Science* **331**, 290–291 (2011).
- 22) X. Xia, Y. Wang, A. Ruditskiy, Y. Xia, 25th Anniversary Article: Galvanic Replacement: A Simple and Versatile Route to Hollow Nanostructures with Tunable and Well-Controlled Properties. *Adv. Mater.*, **25** 6313-6333 (2013).
- 23) H. Liu, T. Liu, L. Zhang, L. Han, C. Gao, Y. Yin, Etching-Free Epitaxial Growth of Gold on Silver Nanostructures for High Chemical Stability and Plasmonic Activity. *Adv. Func. Mater.*, **25**, 5435-5443 (2015).
- 24) Y. Yang, J. Liu, Z.-W. Fu, D. Qin, Galvanic Replacement-Free Deposition of Au on Ag for Core–Shell Nanocubes with Enhanced Chemical Stability and SERS Activity, *J. Am. Chem. Soc.*, **136**, 8153–8156 (2014).
- 25) S. Wang, K. Qian, X. Bi, W. Huang, Influence of Speciation of Aqueous HAuCl₄ on the Synthesis, Structure, and Property of Au Colloids, *J. Phys. Chem. C.*, **113**, 6505–6510 (2009).
- 26) S. S. Abd El Rehim, H. H. Hassan, M. A. M. Ibrahim, & M. A. Amin, Electrochemical behaviour of a silver electrode in NaOH solutions, *Monatshefte fuer Chemie*, **129** 1103-1117 (1998).
- 27) T. A. Green, Gold electrodeposition for microelectronic, optoelectronic and microsystem applications, *Gold Bull.* **40**, 105 (2007).
- 28) M. R. Beversluis, A. Bouhelier, & L. Novotny, Continuum generation from single gold nanostructures through near-field mediated intraband transitions. *Phys. Rev. B* **68**, 115433 (2003).
- 29) K. Imura, T. Nagahara, & H. Okamoto, Plasmon mode imaging of single gold nanorods. *J. Am. Chem. Soc.* **126**, 12730–12731 (2004).
- 30) P. Mühlischlegel, H.-J. Eisler, O. J. F. Martin, B. Hecht, & D. W. Pohl, Resonant optical antennas. *Science* **308**, 1607–1609 (2005).

- 31) P. Ghenuche, S. Cherukulappurath, T. H. Taminiau, N. F. van Hulst, & R. Quidant, Spectroscopic mode mapping of resonant plasmon nanoantennas. *Phys. Rev. Lett.* **101**, 116805 (2008).
- 32) J-S. Huang, *et al.* Atomically flat single-crystalline gold nanostructures for plasmonic nanocircuitry, *Nat. Comm.*, DOI: 10.1038/ncomms1143 (2010).

ACKNOWLEDGMENTS

X. Yuan is thanked for technical assistance with ellipsometry data (supplementary materials). Funding: This work is supported by the Natural Sciences and Engineering Research Council of Canada (Project number: RGPIN-2017-06882) and CMC Microsystems (MNT Financial Assistance Program). This work made use of 4D LABS and the Laboratory for Advanced Spectroscopy and Imaging Research (LASIR) shared facilities supported by the Canada Foundation for Innovation (CFI), British Columbia Knowledge Development Fund (BCKDF) and Simon Fraser University. Author contributions: S.V.G. and G.W.L. conceived and designed the experiments, S.V.G. performed all film deposition, characterization, and nanofabrication experiments, F.C.M. developed the methodology and fabricated single crystal silver substrates, X.Z. performed the TEM experiment and analysis, S.K. performed laser scanning 2PPL microscopy experiments and analyses, G.W.L. wrote the manuscript with input from all. Competing interests: The authors declare no competing interests. Data and Materials availability: All data are available in the manuscript or the supplementary materials.

Supplementary Materials

Scalable green synthesis of monocrystalline noble metal nanostructures for low-loss plasmonic and nanophotonic applications

*Sasan V. Grayli, Xin Zhang, Finlay C. MacNab, Saeid Kamal, Gary W. Leach**

Single Crystal Ag(100)/Si(100) Substrates

Single crystal Ag(100)/Si(100) substrates were prepared by thermal evaporation of silver onto H-terminated Si(100) substrates. Silver deposition was conducted using a Kurt J. Lesker Company PVD-75 thermal evaporation tool with a base pressure of $< 2 \times 10^{-7}$ Torr. Ag (99.99% Kurt J. Lesker Company) was evaporated from an alumina coated tungsten wire basket. The substrate was heated via a backside quartz lamp and the temperature was monitored with a K-type thermocouple attached to the backside of the sample chuck assembly. Deposition was carried out at a temperature of 340°C and a rate of 3 Å/s to a thickness of 500 nm. Prior to Ag deposition, substrates were immersed in commercial buffered oxide etch solutions (BOE, CMOS Grade, J.T. Baker Inc.), to remove the native oxide layer from the surface of the silicon wafer. All activities, prior to characterization of the films, were carried out under class 100 clean room conditions or better. A more complete description of the deposition characteristics and crystallite evolution of silver evaporated onto silicon substrates will appear in a forthcoming publication.

Physical Vapour Deposition of Gold Films

Thermal evaporation of gold onto Si(100) substrates was carried out to provide a source of thin film gold that would represent the typical polycrystalline film quality, characteristic of PVD deposition. Onto a native oxide covered Si(100) wafer was deposited 5 nm of chromium to act as an adhesion layer. Gold was thermally evaporated at 1 Å/s onto an unheated substrate under substrate rotation. This resulted in gold island growth and coalescence into thin polycrystalline gold films. A top view SEM of a typical film is displayed in Fig. 32d of the manuscript.

Electroless Growth of Noble Metal Films

Gold films were deposited spontaneously from solutions of chloroauric acid (HAuCl₄) onto single crystal Ag(100) substrates prepared as described. Gold films deposited from aqueous HAuCl₄ solutions without pH control resulted in galvanic replacement, in which the monocrystalline silver substrate was quickly oxidized and resulted in a poor quality, dark, film which was later determined to be a porous polycrystalline film of silver and gold (Fig 36a). In contrast, the same deposition from pH 14 solutions led to the deposition of high optical quality gold films (Fig 36b). As discussed in the main text, galvanic replacement was avoided by maintaining a high concentration of hydroxide ions in solution. Single crystal Au(100) film deposition was carried out by immersing a 1 x 1 cm² Ag(100)/Si(100) substrate into a deposition bath maintained at 60°C. The deposition bath was a mixture of 500 μL of 0.0025 M HAuCl₄ in 10 mL of 1.0 M NaOH (all solutions prepared from Millipore purity water of 18.2 MΩ-cm resistivity). After 1 hour, the sample was removed from the deposition bath and rinsed with distilled water for 2 minutes and then air dried. Film thickness and deposition rate were found to be well controlled through control of kinetic parameters such as HAuCl₄ concentration, deposition temperature, and deposition time. Optical images of Au deposited from solution onto single crystal Ag(100)/Si(100) substrates under conditions of galvanic replacement (uncontrolled pH) and highly alkaline conditions (pH 14) are shown in Figure 36.

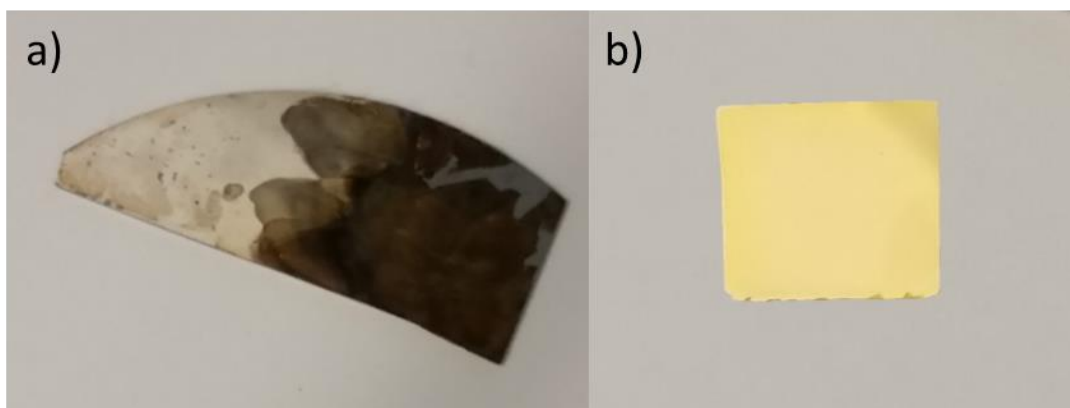


Figure 36. Photo of a Au film following Au deposition onto a single crystal Ag(100)/Si(100) substrate from (a) an electroless deposition bath containing HAuCl_4 at uncontrolled pH and b) an electroless deposition bath containing HAuCl_4 at pH 14 (1 cm x 1 cm substrate).

Cyclic Voltammetry

Cyclic voltammetry study was carried out in order to determine the oxidation potential of Ag under the 1.0 M alkaline condition. Standard three-electrode electrochemical cell conditions comprising a Ag/AgCl (3 M KCl) reference electrode and a platinum wire counter electrode were employed. Figure 37 shows the cyclic voltammogram of a Ag(100)/Si(100) single crystal working electrode immersed in a 1 M OH^- electrolyte. The CV shows the lowest energy oxidation process at 0.375 V versus Ag/AgCl, attributed to electroformation of soluble $[\text{Ag}(\text{OH})_2]^-$ and the growth of Ag_2O . Relative to the standard hydrogen electrode (SHE) under standard (1 M $[\text{H}^+]$) conditions, the measured oxidation potential corresponds to a potential of $E = 0.375 + 0.197 + 0.826 = 1.398$ V. The detailed description of the reduction potential measurement of $\text{Au}(\text{OH})_4^-$ is presented in Chapter 3.

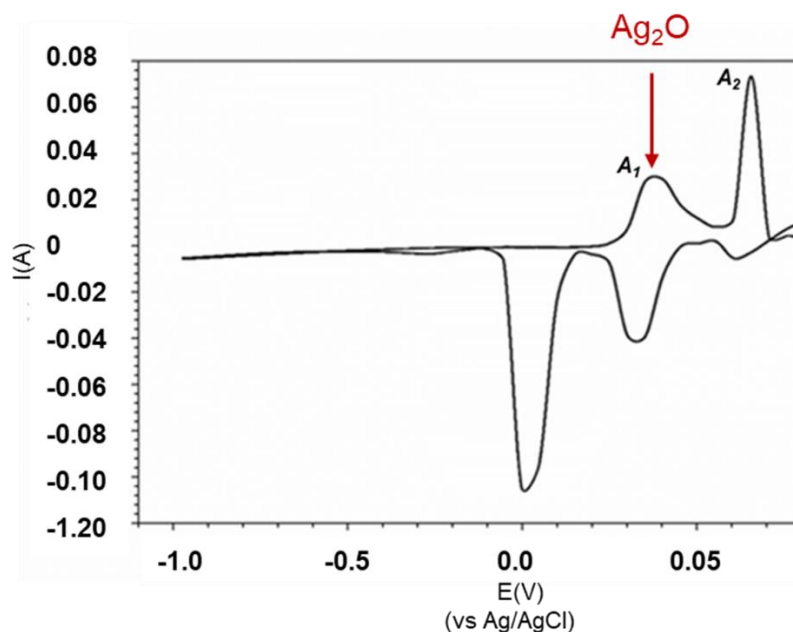


Figure 37. Cyclic Voltammetry of a Ag(100)/Si(100) single crystal working electrode immersed in a 1 M OH⁻ electrolyte. The lowest potential oxidation wave (indicated by the red arrow) appears at 0.375 V versus Ag/AgCl.

Nanopillar Array Fabrication

Nanopillar arrays are formed by electroless deposition of Au and Ag from alkaline solutions of their commonly available salts onto electron-beam patterned thin film masks of poly(methyl methacrylate) (PMMA) spin cast onto single crystal Au(100)/Ag(100)/Si(100) substrates prepared as described above. Nanopillar arrays of small diameter pillars (< 200 nm diameter) (see Fig. 35 of the main text) were formed using 100 nm thick PMMA A2 electron beam resist layers. Nanopillar arrays with larger diameters (see Fig 38 below) were prepared from 200 nm thick PMMA A4 resist layers. The fabrication procedures are described below.

Arrays of nanoholes are formed on an electron-sensitive poly(methyl methacrylate) (PMMA) A2 film used as a mask to grow Au nanopillars on a

single crystal Au film which was grown on a Ag(100)/Si(100) single crystal substrate, as described. The PMMA A2 film was spin-coated at 1000 rpm to achieve 100nm thickness and was soft baked for 4 minutes on a hotplate at 180°C. Electron beam exposure under conditions of 0.178 nA beam current, 0.1 dose factor x 0.15 pC dot dose exposure were employed to irradiate the PMMA with a Raith e-LiNE lithography tool at 30 μm aperture and 10 kV Extra High Tension (EHT). The exposed regions were developed to remove the electron beam-modified resist and expose the Au(100) surface at the base of each exposed region with a solution of developer (MIBK-IPA 3:1) for 120 s, followed by dipping the sample in isopropyl alcohol (IPA) for 120 s (used as an etch stop) and 120 s hard bake at 100°C on a hotplate. Resist development provided a patterned surface of 125 nm diameter cylindrical pores formed on a 2x2 mm² Au(100) substrate with a square lattice of period 550 nm.

The fabricated arrays are then placed in an alkaline bath containing HAuCl₄ (see bath composition employed for planar film deposition above) for 2 minutes at 60°C to yield Au pillars of 70nm height. The sample was then removed, washed for 2 minutes in distilled water, followed by 1 minute in IPA and then placed in acetone for 2 minutes with sonication to remove the PMMA mask. After the PMMA lift-off, the sample was rinsed with water and air dried prior to SEM imaging. An example of such an array appears in Fig. 35 of the manuscript.

Thicker electron beam resist layers were also employed for larger diameter nanohole array masks. Exposure of an electron-sensitive poly(methyl methacrylate) (PMMA) A4 film, deposited at 4000 rpm onto a 1 x 1 cm² single crystal Au(100) substrate, were used to achieve nominal 200 nm thickness patterned films, prior to 4 minutes of soft bake at 180°C, and exposure using the Raith e-LiNE EBL system. The electron beam exposure was performed at 7 mm working distance, with 20 μm aperture, 20kV extra high tension (EHT) and with area dose of 1.0 x 200 $\mu\text{C}/\text{cm}^2$. After the patterning, the PMMA was developed in

MIBK-IPA 3:1 for 120 s followed by 120 s of IPA rinse. Nanostructure growth and resist removal were carried out as previously described. Shown below in Fig. 38 are gold nanopillars grown in a nanohole array of height 200 nm, period 700 nm, and nanohole diameter of 450 nm following Au electroless deposition for 5 mins. The image shows a well-formed array of oriented crystalline nanopillars and the inset shows the top view SEM of a typical faceted single crystal nanopillar with a flat Au(100) top facet.

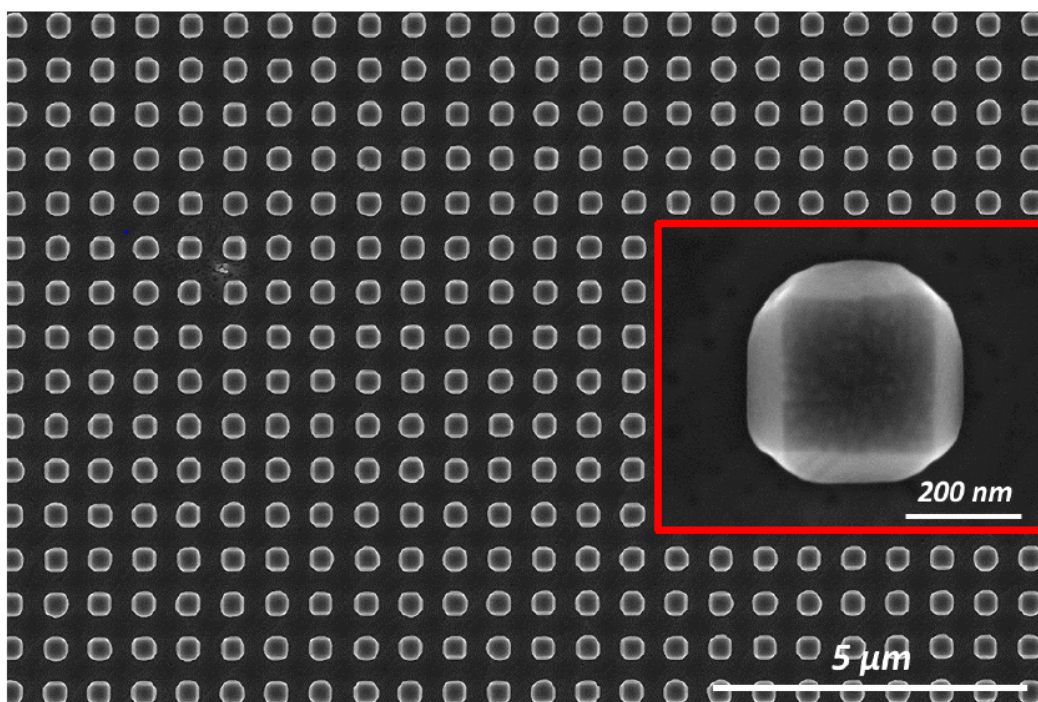


Figure 38. SEM of Au nanopillars (100 nm height, 700 nm period, 450 nm diameter) grown on Au(100) substrate through a nano-electrode array formed with PMMA A4 resist.

Heteroepitaxial deposition of silver nanopillars onto Au(100)/Ag(100)/Si(100) substrates was carried out in a similar manner except that nanopillar deposition was carried out using a deposition bath containing an equivalent concentration of AgNO_3 rather than HAuCl_4 as employed for gold nanopillar deposition. Thin layer Au capping of the resulting silver nanopillar arrays was carried out by immersing the substrate containing the silver

nanopillar array into a HAuCl_4 -containing bath as described above for 1 min. This yielded a Au capping layer of 10 nm nominal thickness, as determined by SEM pillar diameter measurements before and after gold capping layer deposition.

2-Dimensional X-ray Diffraction of Au films

Au film crystallinity was assessed with a Rapid Axis Rigaku X-ray diffractometer equipped with an area plate detector. The X-ray exposure was carried out at 46 kV voltage and 42 mA current using a $\text{Cu K}\alpha$ source incident on the sample through a 500 μm collimator. The sample stage was fixed at 45° angle for the χ axis, 180° rotation of the φ axis, and oscillation from 205° to 215° of the Ω axis. Figure 32a and 32b show the indexed 2D X-ray diffraction pattern from solution-deposited Au onto single crystal $\text{Ag}(100)/\text{Si}(100)$ samples from uncontrolled pH solutions of HAuCl_4 (Fig 32a) and pH 14 HAuCl_4 (Fig 32b) solutions. The diffraction patterns show contributions from the underlying single crystal $\text{Si}(100)$ and 500 nm thick $\text{Ag}(100)$ layers which appear as well localized diffraction spots, in addition to the nominal 120 nm thickness Au overlayers. Deposition from uncontrolled pH deposition baths result from galvanic replacement and are characterized by polycrystalline Au deposition that shows $\text{Au}(111)$ and $\text{Au}(200)$ diffraction arcs at constant 2θ diffraction angles (Fig 32a). In contrast, deposition from pH 14 deposition baths yields oriented and aligned Au deposition resulting in well-defined diffraction spots (Fig 32b). Since the lattice constants of Au and Ag are 4.07 Å and 4.08 Å respectively, their diffraction spots are difficult to resolve and appear as overlapping diffraction signals. Nevertheless, their appearance as diffraction spots as opposed to extended diffraction arcs as observed in the case of polycrystalline Au deposition is consistent with substrate-aligned single crystal deposition.

Cross-sectional SEM and TEM Analysis

Transmission electron microscopy (TEM) was performed using a 200 kV FEI Tecnai Osiris S/TEM to image the crystalline lattice of Au and Ag films. Prior to analysis, a $10 \times 6 \times 5 \mu\text{m}^3$ portion of the sample was lifted-out using a FEI Helios focused-ion beam (FIB) tool and secured on a copper-based TEM grid. The sample was thinned to approximately 30nm prior to TEM analysis. A cross-sectional scanning-electron micrograph of a nominal 70 nm thickness Au film, electrolessly deposited onto the Ag(100)/Si(100) substrate is shown in Fig. 39 below. Also evident from the SEM is a top layer of protective platinum deposited with the FIB instrumentation on top of the Au, in order to protect the gold surface during focussed ion beam milling.

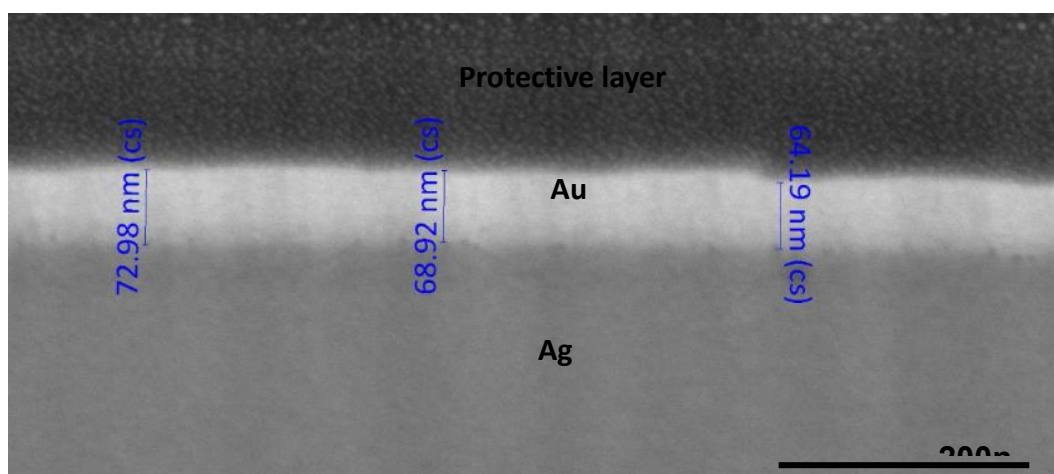


Figure 39. A cross-sectional SEM image of the electrolessly deposited Au film on single crystal Ag(100).

Surface Roughness Analysis

Surface roughness of the solution-deposited, epitaxial gold film was assessed and compared with a thermally evaporated polycrystalline gold surface using a NanoSurface NaioAFM atomic force microscope (AFM). The analysis was carried out over arbitrary $700 \times 700 \text{ nm}^2$ areas at 10 nN force with 0.4 s time/line scanning speed in contact mode with an AFM tip of force constant 0.1 N/m . The results are shown in Figure 40.

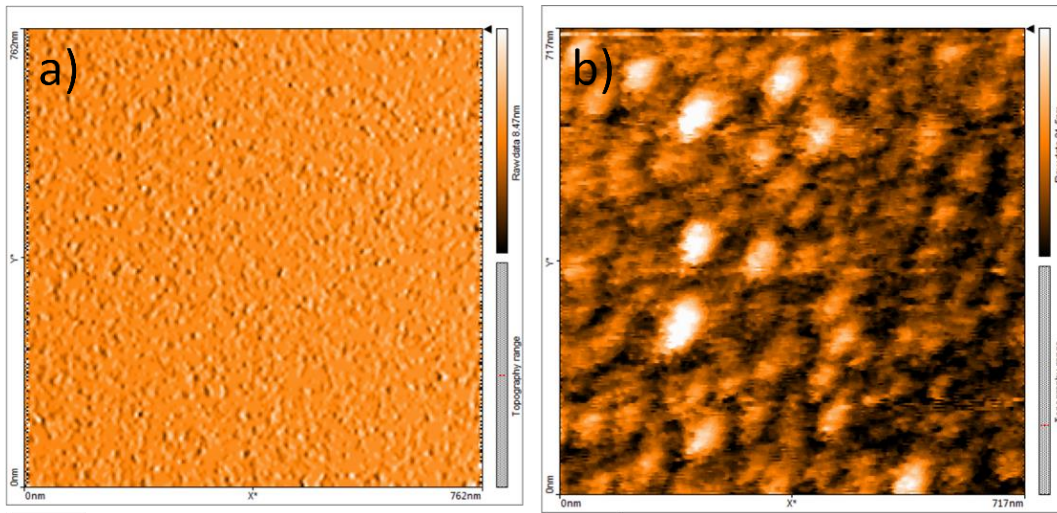


Figure 40. AFM surface topography image of a) solution-deposited, electroless single crystal Au film and b) thermally evaporated, polycrystalline Au film. The area of the scanned regions is approximately 700 x 700 nm².

The area averaged surface roughness (S_A) was assessed by the difference in height of each point compared to the arithmetical mean of the surface ($S_A = \frac{1}{A} \iint |Z_{x,y}| dx dy$) for the imaged regions. S_A was found to be 122.2 pm for the solution-deposited, electroless single crystal Au film and 2.84 nm for the physical vapour deposited polycrystalline Au film.

Using the tool software, three-dimensional topographic images of both the solution-deposited, and PVD-deposited Au films were also constructed and are shown in Fig. 41.

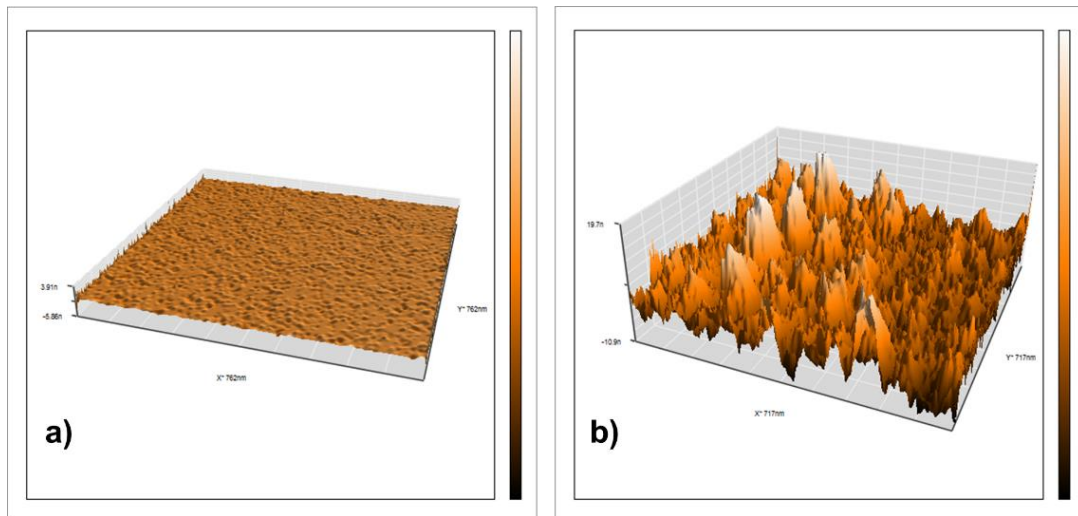


Figure 41. The constructed 3D AFM image of the surface of a) solution-deposited, electroless single crystal Au film and b) thermally evaporated, polycrystalline Au film.

Focused-Ion Beam Nano-Patterning

The FEI Helios NanoLab 650 dual SEM/Focused-Ion beam (FIB) tool was used to fabricate the nanoscale structures and devices presented in Figures 33 and 34 of the manuscript. Subtractive patterning of mono- and polycrystalline gold films were carried out using the focussed gallium ion beam, employing the tool's pre-set conditions for Au. The ion beam current was set to 7.7 pA for the 30 kV source voltage. Under these conditions, 50 nm-depth etching was achieved with a dose of 33 pC/ μm^2 for the evaporated polycrystalline films. These conditions were employed for both the polycrystalline and monocrystalline structures displayed in Fig. 33 of the manuscript. This study revealed that milling rates of the single crystal Au films were significantly lower than for polycrystalline films and that, following a dose study, the dose had to be doubled to achieve equivalent 50 nm-depth milling of the single crystal Au films. These conditions were subsequently employed for the fabrication of the single crystal bowtie nanoantennas described in Fig. 34 of the manuscript. Milling of the evaporated gold films leads to anisotropic, crystal direction-dependent milling rates, resulting in non-uniform milled regions and poor quality pattern transfer. In contrast, FIB milling of single crystal Au deposited from solution leads to a high degree of uniformity in the milled regions and much improved pattern transfer characteristics. Figure 42 shows a

fabricated bowtie antenna of both monocrystalline and polycrystalline Au films under the FIB milling conditions just described.

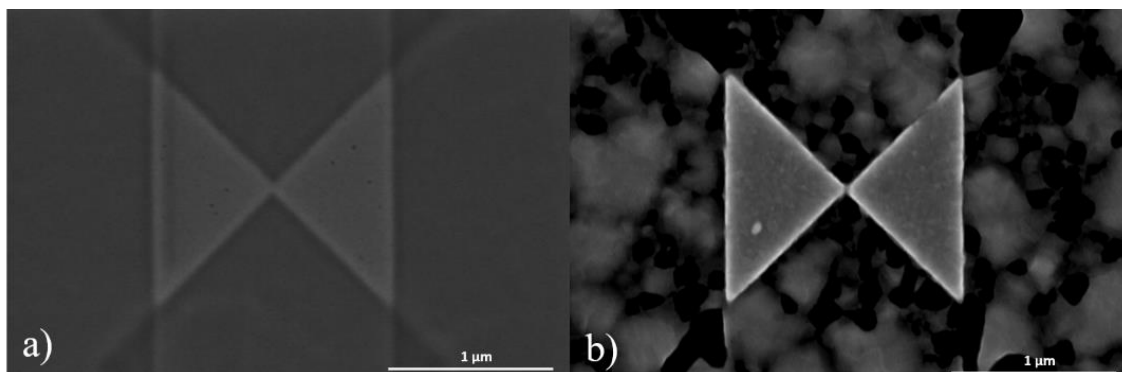


Figure 42. Top view SEM image of a FIB-milled bowtie nanoantenna fabricated with a) epitaxially-grown solution-deposited monocrystalline Au, and b) thermally evaporated polycrystalline Au.

Electron-Beam Lithographed Lines

An e-LiNE Raith EBL system was used to pattern lines to fabricate high aspect ratio, single crystal Au nanowires. A PMMA A2 electron beam resist layer was spin-coated at 4000 rpm to achieve 50nm thickness on a thermally evaporated single crystal Ag(100)/Si(100) substrate prepared as described. The PMMA A2 layer was soft baked for 4 minutes at 180°C on a hotplate prior to electron beam exposure. The PMMA film was irradiated a 20kV EHT source, 20μm aperture with 1.6 x 300 pC/cm line exposure factor with 5nm step size at 0.162 nA write current. After the exposure, the substrate was immersed in MIBK:IPA (3:1) for 120 s, followed by 120s IPA rinse and then hard baked at 100°C for 120 s on a hotplate. The exposed Ag regions were then used to grow epitaxial Au nanowire lines by immersing the patterned substrate in the electroless deposition bath for 5 minutes at 60°C. Figure 43 shows a large area SEM image of a portion of the Au lines which were patterned to form a large area concentric square structure capable of acting as a broadband plasmonic nanoantenna. A detailed discussion of the broadband plasmonic response of these structures is beyond the scope of the current manuscript but will appear in a forthcoming publication.

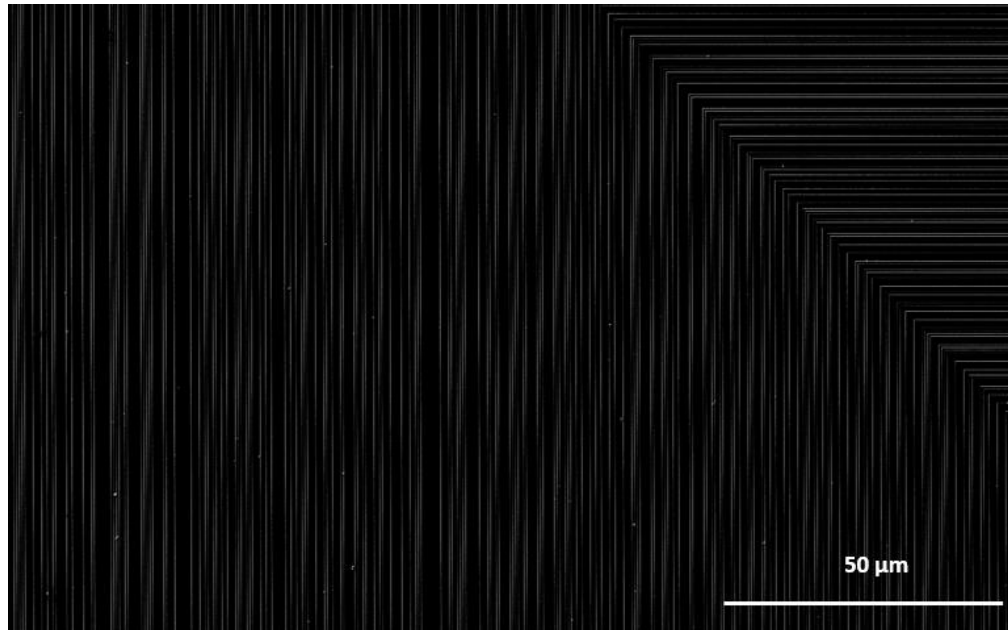


Figure 43. *Top view SEM image of epitaxially grown Au lines on a single crystal Ag(100) substrate patterned by EBL and deposited from an alkaline $\text{Au}(\text{OH})_4^-$ deposition bath as described.*

Laser Scanning Microscopy

Laser scanning microscopy was carried out with Leica and Zeiss scanning laser confocal microscope systems. The 2PPL images (excitation wavelength 800 nm) of the concentric square nanowire structures (Fig. 35h) were obtained with a Leica TCS SP5 II microscope equipped with a HCX PL APO CS 10x/0.4 IMM objective and a 75 MHz repetition rate, dispersion compensated, 140 fsec Chameleon excitation laser (Coherent) tunable from 680-1080 nm with a typical output power of 3.5 W at 800 nm. High resolution 2PPL images of bowtie nanoantennas (Fig. 34 - excitation wavelength 780 nm) and the nanopillar array (Fig. 34c – excitation wavelength 750 nm) were obtained with a Zeiss LSM 510 MP microscope equipped with an LD Plan-Neofluar 63x/0.75 Korr objective lens and a 75MHz repetition rate, 140 fsec Chameleon Ultra excitation laser tunable from 710-980 nm.

Sheet Resistance

The sheet resistance of electroless, solution-deposited epitaxial Au films were measured with a 4P Model 280 4-point probe electrical characterization system and compared with Au films deposited by evaporation, as described. The thickness of films was 100 nm as determined by SEM. At this thickness, the films are expected to display their limiting, bulk resistivity and not be affected by the markedly different electrical properties of the underlying substrates on which they are deposited (see for example, K. L. Chopra, L. C. Bobb, and M. H. Francombe “Electrical Resistivity of Thin Single-Crystal Gold Films”, *Journal of Applied Physics* 34, 1699-1702 (1963)).

The measured sheet resistance for the solution-deposited monocrystalline Au film was determined to be $0.023 \pm 0.001 \text{ } \Omega/\square$ while that of the evaporated polycrystalline gold film was determined to be $0.457 \pm 0.011 \text{ } \Omega/\square$ respectively, indicating a greater than 20 times lower resistivity of the single crystal Au film relative to the evaporated polycrystalline Au film.

Spectroscopic Ellipsometry

Ellipsometry was performed with a Horiba MM-16 Spectroscopic Ellipsometer. Ellipsometry was carried out on 100 nm thick polycrystalline Au films prepared by thermal evaporation, and on 100 nm thick solution-deposited monocrystalline Au films. This thickness is beyond the optical skin depth of gold (approximately 25 nm in the spectral region investigated – see for example, R. L. Olmon, B. Slovick, T. W. Johnson, D. Shelton, S-H. Oh, G. D. Boreman, and M. B. Raschke, Optical dielectric function of gold, *Phys. Rev B*, 86, 235147 (2012)). Plotted in Fig. 44 are the real (n) and imaginary (k) parts of the refractive index measured from the mono- and polycrystalline films. Optical absorption, associated with the imaginary part of the refractive index, is observed to be measurably lower for the monocrystalline Au film compared to the polycrystalline Au film at energies below 2.5 eV, the onset of the well-known visible interband optical transition in gold.

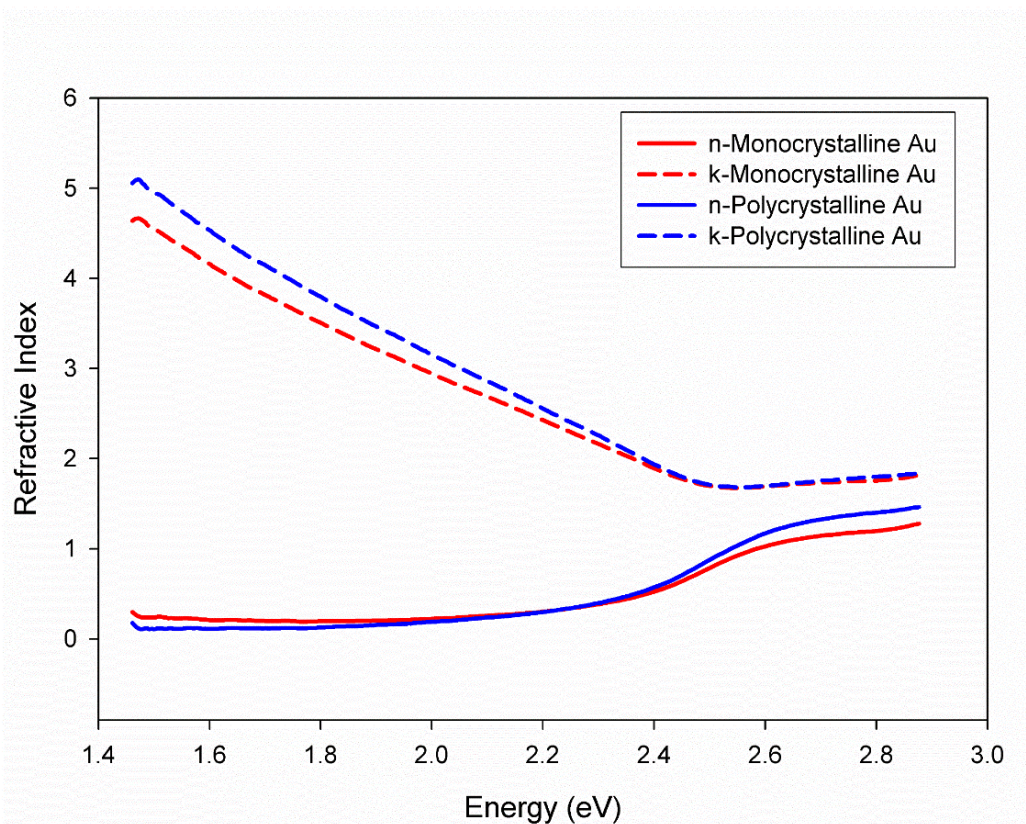


Figure 44. The real (n) and imaginary (k) parts of the refractive index as determined from spectroscopic ellipsometry of a 100 nm thick polycrystalline Au film deposited by thermal evaporation (blue) and a 100 nm thick, electroless, solution-deposited monocrystalline Au(100) film (red).

This chapter was presented here in the same format that was submitted as a manuscript to Nature Nanotechnology as a letter. The detailed description of the chemistry can be found in Chapter 3. The next two chapters are dedicated to demonstrating the possibilities that can be achieved using this electrochemical metal deposition process. Chapter 5 describes how the presence of additives in the solution can lead to surface manipulation and altering the growth of the Au film to the point that it results in formation of surface nanostructures. Such approach has been demonstrated broadly in nanoparticle synthesis, however using similar mechanism to create structures on the surface via an electroless deposition technique can open new and cost effective possibilities for applications where controlling shape and size of crystallites on a surface

in nano-scale is widely desired. Chapter 5 is a manuscript that was prepared for submission to JACS.

Chapter 6 discusses the effect of film quality in activity, durability and efficiency of subtractively fabricated devices that are operating based on the surface plasmon excitation. In this chapter, the quality of a thermally evaporated polycrystalline Au film was compared with a monocrystalline and ultrasmooth Au film that was grown with the EED technique and it is shown how negatively a plasmonic device can be impacted by the quality of the film that it is made on. Chapter 6 is prepared and submitted as a manuscript to ACS Photonics.

Shape-Controlled Growth of Single Crystal Gold Surface Nanostructures

Authors' contributions:

S.V.G. and G.W.L conceived and designed the experiments, S.V.G. performed all film and nanostructure growths, characterization, SERS experiments, SEM imaging, and nanofabrication experiments, X.Z. performed the TEM experiment and analysis, D.S. integrating sphere absorption measurements and analyses, G.W.L. wrote the manuscript with input from all.

5. Shape-Controlled Growth of Single Crystal Gold Surface Nanostructures for Plasmonic and Photonic Applications

Sasan V. Grayli, Xin Zhang, Dmitry Star, and Gary W. Leach*

Department of Chemistry, Laboratory for Advanced Spectroscopy and Imaging Research and 4D LABS, Simon Fraser University, 8888 University Drive, Burnaby, BC, V5A 1S6 Canada.

Abstract: The capture and confinement of free space photons by noble metal nanostructures leads to local near-field enhancements and hot carrier generation that can be exploited for application in energy harvesting, catalysis, and sensory response. While nanostructure size, shape and crystallinity play a critical role in their wavelength-dependent optical response and plasmonic local near-field distributions, the ability to fabricate shape-controlled single crystal noble metal nanostructures and locate them precisely for device applications has remained a significant hurdle that prevents their design and manufacture into practical devices. Here, we describe a novel electroless deposition process in the presence of anionic additives that yields additive-specific shape control effects and allows the deposition of shape-controlled, single crystal plasmonic Au nanostructures on Ag(100) and Au(100) substrates. Deposition of Au in the presence of SO_4^{2-} ions results in the formation of Au(111)-faceted square pyramids that show significant plasmonically-enhanced SERS responses. The use of halide additives that interact strongly with (100) facets produces highly textured hillock-type structures characterized by high index Au faceting and screw-type dislocations (Cl^-), and flat platelet-like deposition characterized by large area Au(100) terraces (Br^-). Use of additive combinations provides structures that comprise characteristics from each additive (SO_4^{2-} and Cl^-), and new square pyramidal structures with dominant Au(110) facets (SO_4^{2-} and Br^-).

Finally, we demonstrate that a combination of bottom-up electroless deposition with top-down lithographic patterning methods can be used to fabricate large area single crystal Au metamaterial arrays, comprised of shape-controlled single crystal Au nanostructures with precise surface locations. We anticipate that this approach will be employed as a powerful new tool to tune the plasmonic characteristics of nanostructures and facilitate their broader integration into device applications.

Nanostructured metals will play a critical role in next generation nanotechnologies. Metal nanostructures support surface plasmons (SPs) that can localize and confine spatially extended electromagnetic waves, enhancing their local fields to enable new chemical and physical phenomena^{1,2}. Metal supported SPs have found application in energy harvesting, photocatalysis, sensors, and engineered metamaterials displaying negative refractive index and sub-wavelength resolution imaging and patterning capability¹⁻³. Nanometer scale metal structures can bridge the disparate length scales of optical fiber technology and the nanoscale electronic circuitry of current electronic devices. The confinement of quantum emitters to nanometer scale plasmonic cavities may also provide a source of single-photon emitters for all-optical transistors and quantum information processing applications³.

Noble metal nanostructures have been a primary focus of many efforts in these areas due to their large charge carrier densities and responses that span the infrared through visible spectral ranges. However, their broader utility for many of these applications is limited by difficulties in precisely controlling the positions, shapes and orientations of noble metal nanostructures into well-defined device geometries that can be readily integrated into manufacturable platforms. Improved control over surface chemistry to overcome these limitations represents a major challenge in the field, with significant potential technological benefit^{3,4}.

The solution phase synthesis of nanocrystals enables the fabrication of nanostructures of well-defined size, shape and composition⁵⁻⁹. The use of specific chemical interactions between solution additives and growing nucleation centers can alter facet-dependent reduction rates to provide specific shape selectivity. The preferential adsorption of these shape control agents leads to facet-dependent

differential growth kinetics^{5,8,10} resulting in structures that display unique, size- and shape-dependent optical and electronic properties^{3,5,8,9,11,12}. However, despite exquisite control in the production of these crystalline nanostructures, they are in solution, isolated from each other by the use of capping agents to enhance their stability and prevent their aggregation into larger structures. In this form, it is difficult to assemble, locate and address these nanoparticles individually with either light or electricity, preventing them from broad incorporation into device structures.

We have recently described an alternative approach to crystalline noble metal nanostructure that is compatible with current device fabrication protocols. The method employs green electroless chemistry that is scalable to the wafer level and enables the fabrication of ultrasmooth, epitaxial, single crystal noble metal films ideal for the subtractive manufacture of nanostructure through ion beam milling, and additive crystalline nanostructure via lithographic patterning to provide single crystal features and large area metamaterial arrays. While noble metals are characterized by inherent optical absorption losses that are exacerbated by their tendency to form polycrystalline structures when deposited by conventional physical vapor deposition methods, our single crystal metal nanostructures limit optical absorption and resistive losses and demonstrate improved thermal and mechanical stability compared to polycrystalline structures. The capability of fabricating nanoscale plasmonic materials with control over size, shape, crystallinity, and substrate location would provide a new level of control to create next generation nanoscale technologies. Here, we describe the use of shape control strategies typically employed in the solution phase synthesis of nanocrystals to impart shape control to surface nanostructure, expanding the toolkit for controlling metal surface texture with nanoscale level precision.

Under highly alkaline conditions, the deposition of Au from aqueous solutions of HAuCl_4 onto Ag(100)/Si(100) single crystal substrates leads to the formation of ultrasmooth, epitaxial, single crystal, thin Au(100) films (Fig 45a). The deposition of gold in the presence of SO_4^{2-} anions alters the resulting Au film morphology significantly (Fig. 45b). Scanning electron microscopy (SEM) of this textured film shows that the film is comprised of small (sub-100 nm) faceted features that show a general square pyramidal shape preference. Attempts to remove or dislodge these structures by repeated sonication and cleaning were unsuccessful, indicating they are an integral component of

the surface structure and have not been formed by nucleation in solution followed by deposition onto the substrate. Closer inspection indicates that the facets are smooth and oriented with respect to the underlying substrate, lending support to this view (Fig 45c).

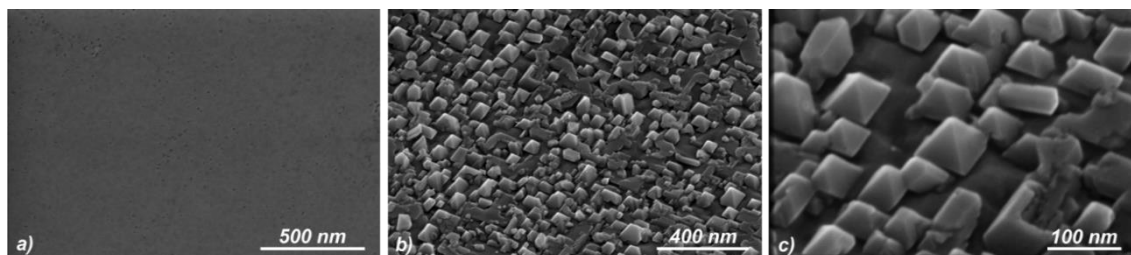


Figure 45. The effect of sulfate anion on single crystal Au deposition. a) Plan view SEM of a smooth, epitaxial, single crystal Au film deposited through alkaline electroless deposition of a HAuCl_4 solution onto a $\text{Ag}(100)/\text{Si}(100)$ single crystal substrate. b) Tilt view SEM of a Au-nanopyramid textured Au film grown as in a) but with the incorporation of 0.25 M NaSO_4 in the deposition bath. c) Expanded view of b) highlighting the strong square pyramidal shape preference, the common orientation of square pyramids with respect to the underlying substrate, and the smooth facets of the nanostructures.

The single crystal $\text{Ag}(100)/\text{Si}(100)$ substrates used in this work are formed by thermal evaporation of Ag onto H-terminated $\text{Si}(100)$ wafers. The wafer is carefully split into smaller $1 \times 1 \text{ cm}^2$ substrates by ready fracture of the wafer along its $\langle 110 \rangle$ directions^{15,16} (M1-0302 SEMI standards). The crystal substrate on which the Au growth begins is $\text{Ag}(100)$ with (110) substrate edges. The orientation preference of the nanopyramids is observed to be such that the square bases of the pyramidal structures are aligned parallel to the edges of the substrate. This orientation preference suggests that the pyramid facets are the $\langle 111 \rangle$ family of crystal planes. The growth of Au films in the presence of higher sulfate concentrations (0.50 M and 0.75 M) was also investigated. The results of these studies (supporting documents) show the same shape preference with modest differences in crystallite size and surface density.

High resolution transmission electron microscopy (HRTEM) reveals that the square pyramidal structures are monocrystalline and oriented as described. Fig 46a shows a TEM image of two adjacent nanostructures of nominal 40 nm dimension that appear triangular in cross-section. Elemental mapping (Fig 46b) shows that the

structures are Au in composition and sit atop a thin layer of Au formed on the Ag(100)/Si(100) single crystal substrate. TEM measurements of the nanocrystallite facet angles relative to the (100) substrate suggests that the observed square pyramidal structures display their (111) facets, consistent with the expected angle of 54.7° between the $\langle 100 \rangle$ and $\langle 111 \rangle$ crystal planes of face-centered-cubic metals (Fig. 46c). This is confirmed through HRTEM measurements (Fig. 46d) that display the single crystal nature of the square pyramidal crystallites as well as their orientation with respect to the underlying single crystal substrate, through direct observation of the crystallite lattice planes.

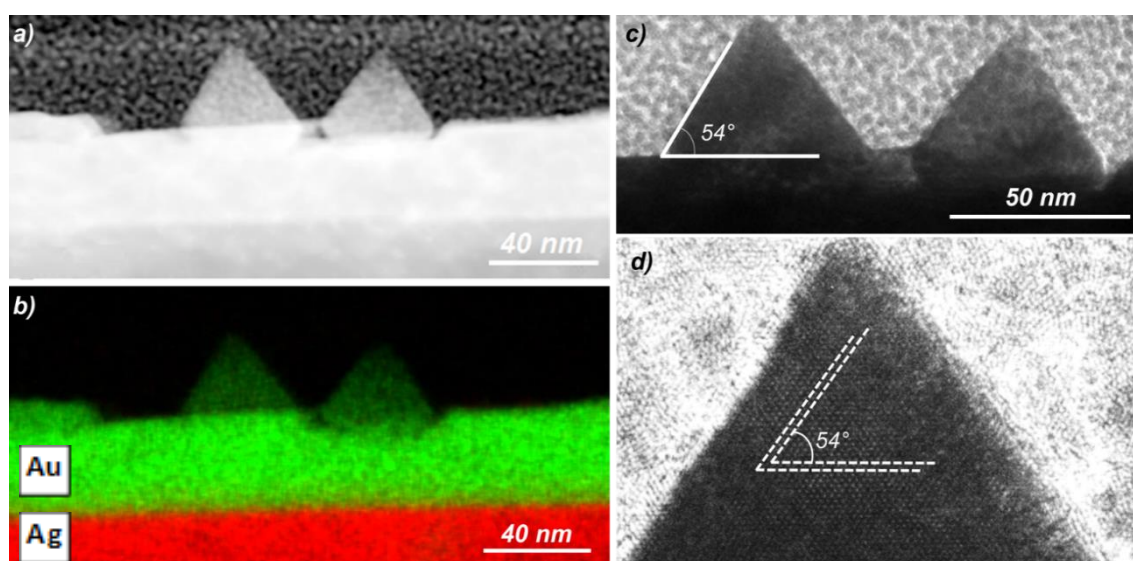


Figure 46. a) and b) are the elemental mapping done by TEM, b) shows the Au film (green) grown on top of Ag film (red), c) is a TEM image in which the angle of the pyramid's facet and the surface is measured and d) is a high-resolution TEM image of side of a nanopyramid in which the angle between the crystalline lattice is measured.

Under the alkaline conditions employed for Au deposition, the silver substrate and subsequent growing gold film are strongly influenced by adsorbed hydroxide species and by anionic additives capable of interacting with the substrate. The growing gold film evolves by the gradual appearance of step edges and the growth of minor facets as deposition proceeds on the original and available (100) substrate facet. The facet-dependent relative reduction rates then determine the resulting film morphology. The growth of Au in highly alkaline conditions gives rise to smooth epitaxial Au films (Fig

45a), implying that lateral growth along the family of $\langle 110 \rangle$ directions is more rapid than growth on other crystal facets (vide infra). However, the presence of SO_4^{2-} anions has a profound effect on the resulting film morphology, giving rise to shape selective growth. The mechanism for square pyramidal shape preference can be understood in terms of an interaction between sulfate anions and the Au(111) facets of the evolving monocrystalline Au film. As step edges and minor (111) facets begin to form, adsorption of SO_4^{2-} anions at these sites stabilize them and reduce the rate of their further growth relative to other low index (e.g. (110) and (100)) facets. As film growth proceeds, larger growth rates on the readily available (100) and minor (110) facets lead eventually to their disappearance, and a film surface structure defined by larger area (111) facets. Thus, strong interaction between SO_4^{2-} anions and Au(111) crystal facets serve as an effective blocking mechanism to lower reduction rates on growing (111) facets. Evidence of growth along other (101), $(01\bar{0})$, $(\bar{0}\bar{0}\bar{1})$, and $(00\bar{1})$ planes, which are parallel and angled 45° with respect to the surface, respectively, can also be observed during film growth and lead to expansion of the nanopyramids from the edges of their square bases leading ultimately to the merging of neighbouring nanostructures and the formation of larger square pyramids.

The interaction between SO_4^{2-} anions and Au(111) facets have previously been investigated via in situ infrared spectroscopy, in situ scanning tunneling microscopy and DFT calculation. While these studies have focused on acidic electrolytes, they provide compelling evidence for SO_4^{2-} anion interaction with the Au(111) facet, displaying well-ordered sulfate adlayers in which sulfates are bound at 3-fold hollow sites of the (111) facets via three oxygen atoms, stabilized by water molecules that bridge adjacent adsorbed sulfate anions.^{32,33,34,35} Similarly ordered adlayers are not frequently observed on Au(100) and Au(110) facets, suggesting less well-defined interaction between the oxoanionic adsorbates and these facets of the Au substrate. However, ordered adlayer structures of sulfate and phosphate on Au(100) surfaces have been reported in in situ STM studies of Au(100) by Kolb and co-workers, but suggest that they require the presence of H_3O^+ ions for their stabilization.^{36,37}

We investigated the plasmonic response of these nanostructured Au films via surface enhanced Raman scattering (SERS). Plasmonic local field enhancements are known to enhance scattering efficiencies nonlinearly and are used here as a measure of

plasmonic activity. Figure 47 illustrates the SERS response of two typical Raman marker molecules, benzoic acid (BA) and Rhodamine 6G (R6G). Films of BA and R6G were prepared by dip coating gold substrates from 20 or 10 mM solutions, respectively, and the SERS responses were obtained from a Renishaw (Invia) Raman microscope/spectrometer using a 785 nm diode laser source. Films were deposited on smooth monocrystalline gold and on the nanostructured gold films described above. Also shown in Fig. 47 is the Raman response of a silicon wafer - typically used as an alignment and signal optimization reference for these tools - under identical illumination and collection conditions. The gold film comprised of nanopyramids demonstrates significant SERS enhancement compared to the monocrystalline gold films, providing signal levels comparable to those obtained from the silicon reference. While it is not the focus of this manuscript and no attempts have been made to optimize the SERS response from these nanostructured films, the nanopyramid substrates provide SERS responses comparable to those reported for Au nanoparticles^{11,12,14,17,18} and may provide an alternative approach to the production of SERS substrates. Integrating sphere absorption measurement of the nanostructured film in the absence of an overlayer (supporting documents) shows broadband (500-1000 nm) absorption ranging from 40-20%, which will be shifted to longer wavelengths in aqueous media or upon adsorption of analyte species. The oxidation-resistant gold nanostructured film is cost-effective, cleanable, reusable, and shows plasmonic response over a wide range of wavelengths, making this approach a new potential broadband SERS platform.

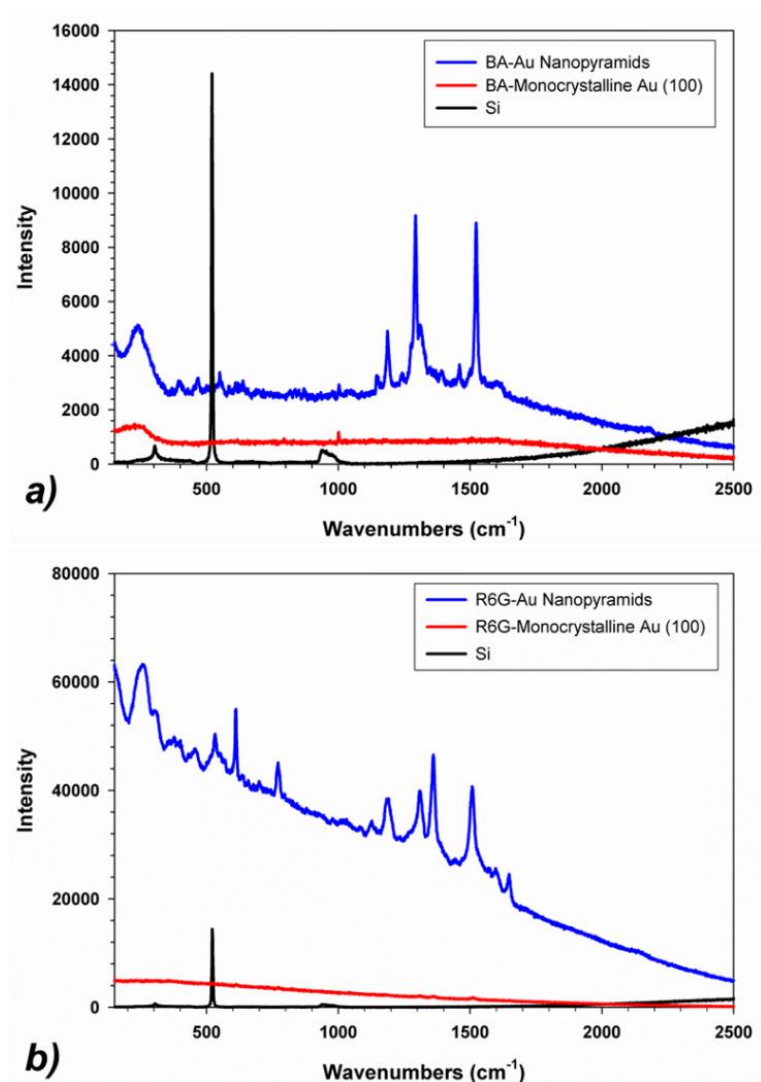


Figure 47. SERS spectra obtained from a) BA-coated Au nanopyramids, BA-coated monocrystalline Au(100) film and a silicon wafer reference sample, b) R6G-coated Au nanopyramids, R6G-coated monocrystalline Au(100) film and a silicon wafer reference sample.

We have also examined the role of other anionic electrolyte additives on the growth of single crystal gold films (Figure 48). The use of chloride anions in the alkaline electroless deposition bath (Fig. 48a-b) gives rise to surface nanostructure reminiscent of that obtained with sulfate anions (Fig. 48d), but with important differences. Fig. 48a shows that the dominant surface features that result from Cl^- addition are also square pyramidal structures with dominant Au(111) features. However, the pyramidal structures appear to be much larger in dimension (typically $\sim 2 \mu\text{m}$) compared to those resulting from SO_4^{2-} addition, and their Au(111) features appear to have a well-developed texture

that is common to all structures, differing dramatically from the smooth facets that result from sulfate addition. Fig 48b shows an enlarged top view SEM image of a single Au pyramid deposited in the presence of chloride anions. The structure is formed with textured facets that appear to result from a platelet-growth morphology in which the edges of smooth growing Au layers possess defects that drive further deposition to occur discontinuously and with slightly skewed orientation with respect to underlying gold layers. The result are structures possessing highly granular facets that display helical character. This morphology can be understood in terms of the formation of edge and screw type lattice dislocations³⁸ induced by chloride ion interaction with the growing gold surface. Such lattice defects often lead to the growth of spiral like structures and can be explained by a kink-limited growth model in which the growth of crystalline layers is affected by the presence of (here Cl^-) additives.²³⁻²⁵ As the kinks and step edges are formed, their growth kinetics are modified through energetically favorable interaction with additive ions, stabilizing these dislocations and limiting further low index facet growth, leading to textured structures comprising higher index Au facets. To the best of our knowledge, this type of growth behavior has not previously been observed through chloride addition, however, the use of chloride ions in conjunction with Ag^+ has been implicated in the growth of concave cubic gold nanocrystals with high-index facets.³⁹

Halide adsorption on the (100) and (110) facets of FCC metals is expected to differ significantly from that on (111) facets, where the hexagonal symmetry of halide adlayers is expected to mimic the underlying surface symmetry. Strong adsorbate-metal interactions between halides and (100) surfaces is thought to arise from their preferred four-fold hollow adsorption sites. Due to weaker relative repulsive interactions between adsorbed ions and the higher coordination of the adsorbed ions with the surface metal atoms, halide adsorbates are more strongly bound in these sites than in the three-fold hollow sites on (111) surfaces⁴⁰. Preferential halide adsorption on Au(100) facets can give rise to slow and/or discontinuous growth on (100) surfaces, impeding the deposition of smoothly faceted structures, explaining, at least in part, the structures resulting through chloride additive deposition.

The use of bromide ions (Br^-) in the solution-phase synthesis of shape-controlled nanocrystals is well known, where strong Br^- ion interaction with the family of (100) crystalline facets leads to their stabilization, and a range of resulting shape-

controlled structures^{5,17,31}. Fig 48c displays the effects of Br^- on the electroless deposition of gold on Ag(100) single crystal substrates. The SEM image displays a largely flat surface collage comprised of (100) terraces with little to no structure normal to the surface. The image displays many step edges indicating film evolution primarily through lateral growth. Closer inspection of the step edges reveals that they are oriented predominantly in the family of $\langle 110 \rangle$ directions. This motif is consistent with strong adsorption of bromide anions to the (100) facets preventing the development of minor (111) facets and driving growth along the $\langle 110 \rangle$ directions, resulting in large (100) platelets characterized by (110) step edges.

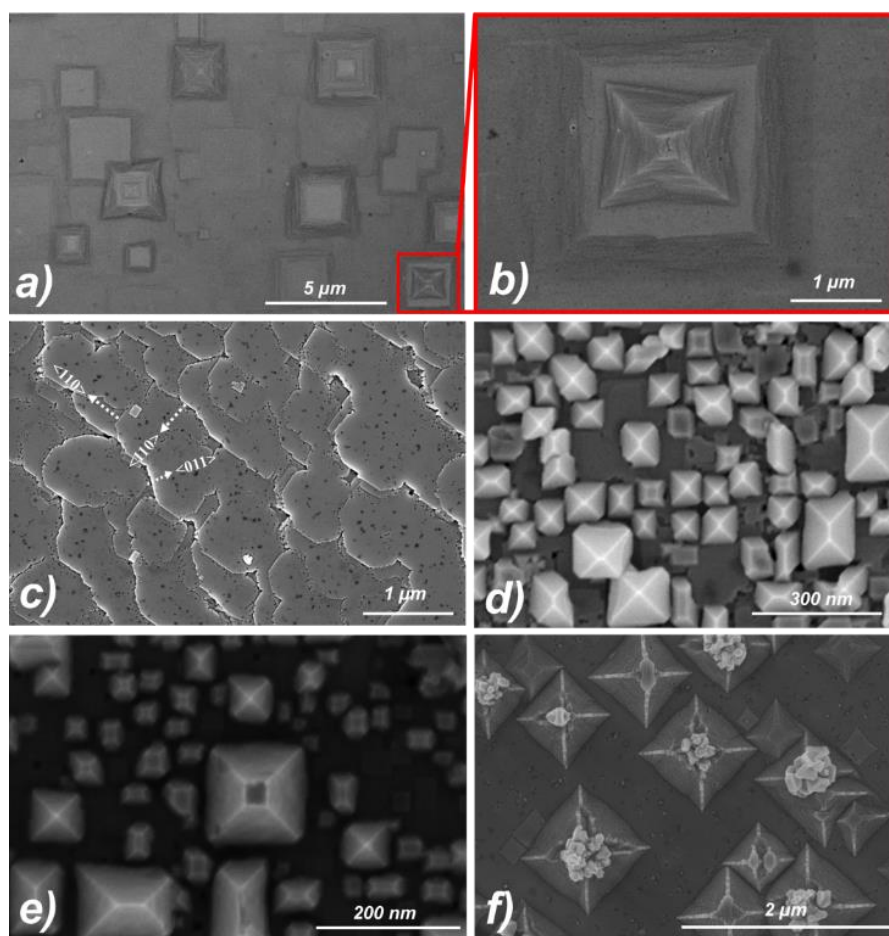


Figure 48. Growth of single crystal Au films under the influence of different anionic additive species. Top-view SEM image of a Au film grown under the influence of a) 0.25 M Cl^- , b) expanded top-view SEM of one of the structures identified in a). Top-view SEM image of a Au film grown under the influence of c) 0.75 M Br^- , d) 0.25 M SO_4^{2-} , e) 0.25 M Cl^- and 0.25 M SO_4^{2-} , and (f) 0.25 M SO_4^{2-} and 0.75 M Br^- .

Gold deposition in the presence of additive mixtures provides an additional means of tailoring surface nanostructure. Figure 48e displays a plan view SEM image of Au film deposition in the presence of both sulfate and chloride anions. Interestingly, the resulting nanostructures display elements of Au deposition observed from each additive. The dominant structural motif is the appearance of square pyramidal structures as observed for sulfate additive-based growth (Fig 48d). However, unlike the pyramids formed from sulfate additives alone which are characterized by smooth (111) facets, the presence of chloride additives appears to impart additional texture to the (111) facets, as one might anticipate based on Figs 48a-b. Further, the use of other additive combinations can provide nanostructure facet selection as illustrated in Fig 48f, where the combination of sulfate and bromide ions are employed during gold deposition. The presence of sulfate anions again favors the appearance of oriented square pyramidal nanostructures. However, the orientation of the pyramidal facets in this case are rotated 45° with respect to those observed from the sulfate additive alone. The additional presence of bromide in the deposition bath gives rise to the growth of square pyramidal nanostructures comprised of (110) facets, consistent with the observation of bromide-induced growth in the <110> directions.

The presence of anionic additives in the deposition bath during alkaline epitaxial electroless deposition represents a new strategy to control single crystal surface nanostructure. The range and complexity of interactions that can affect nanostructure growth in these systems is significant and can include the facet-dependent interactions between anionic additives and the growing single crystal metal, and facet-dependent anion-anion interactions within anionic adlayers. The use of anionic additives can further complicate the deposition chemistry through formation of mixed Au³⁺-based complex ions, whose facet-dependent reduction potentials will differ from those of Au(OH)₄⁻ ions. Other possible complications include the potential for metal ion reduction via additive anions as opposed to OH⁻ ions, as we have previously assumed in the absence of additives. Nevertheless, shape-controlled single crystal surface nanostructure can be achieved through differential growth kinetics on the growing facets of monocrystalline metal substrates, providing the capability of fabricating nanoscale plasmonic materials with control over size, shape, crystallinity, and substrate location.

Here, we demonstrate this control by employing a combination of the “bottom-up” growth of shape-controlled single crystal gold nanostructures with “top-down” electron beam lithography (EBL) patterning methods to yield a single crystal Au nanostructured metamaterial array. Under the prevailing alkaline deposition conditions, hydroxide ions can act as both a shape control agent through facet-dependent Au-hydroxide ion interactions, as well as the reducing agent required to convert the Au(III)-based $\text{Au}(\text{OH})_4^-$ complex ions to Au. Unrestricted growth on planar Ag(100) and Au(100) substrates (Fig 45a) proceeds through a 2-dimensional, rapid in-plane growth mechanism in the family of $\langle 110 \rangle$ directions, to yield ultrasmooth single crystal Au(100) films. Laterally restricted growth results in deposition normal to the surface, dictated by the (much slower) relative rates of deposition on the (111) and (100) facets. Figure 49a shows a top view SEM image of a single crystal Au metamaterial array formed by epitaxial electroless deposition onto an EBL-patterned Au(100) surface containing a 700 nm period, square array of 200 nm diameter cylindrical pores formed by patterning a 200 nm thick film of PMMA electron beam resist. Fig 49b illustrates the faceted, single crystal nature of the individual pillars, comprised of a flat-top (100) facet and (111) faceted side walls. The shape of the resulting structures suggests that the effects of the hydroxide ion are to impart relative facet-dependent growth rates, R_{facet} , such that $R_{110} \gg R_{100} > R_{111}$. With rapid lateral growth within the pores, the nanopillar shape is dictated by growth in the $\langle 100 \rangle$ direction that is more rapid than in the $\langle 111 \rangle$ direction, leading eventually to the disappearance of the (100) facet and the prevalence of (111) facets. Note that the order of facet-dependent growth rates correlates well with the relative order of hydroxide ion adsorption energies on the three low-index Au surfaces $\text{Au}(110) > \text{Au}(100) > \text{Au}(111)$,⁴¹ suggesting that the rate of $\text{Au}(\text{OH})_4^-$ reduction is limited by its adsorption to the gold surface through its hydroxide ligands and/or that surface bound hydroxide plays a key role in the detailed reduction mechanism. Use of other additives or additive combinations provides a mechanism to alter these relative growth rates through blocking mechanisms or modified reduction mechanisms and therefore, to drive alternative crystalline facet structure as demonstrated in Fig. 49.

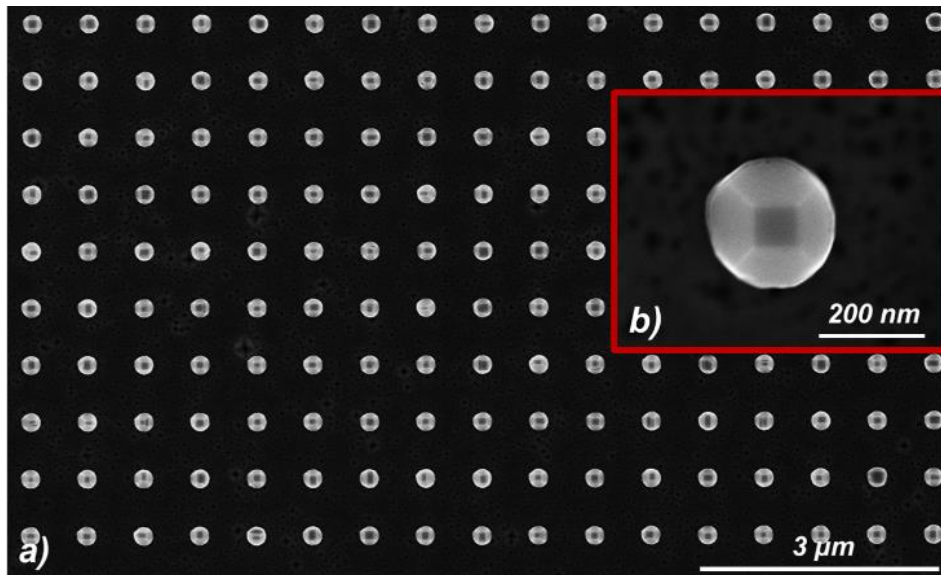


Figure 49. a) Plan view SEM image of an ordered array of shape-controlled Au nanostructures fabricated by electroless deposition and EBL patterning (see text) on a Au(100) substrate (hole diameter of 200 nm, 700 nm periodicity. b) Expanded top-view SEM of an individual single crystal pillar at 500000x magnification, showing a (100) top facet and angled (111) side facets.

In summary, we have demonstrated the deposition of shape-controlled single crystal Au surface nanostructures via solution deposition through the use of anionic additives. The method is scalable and environmentally friendly with appropriate additive choice, offering the potential for integration into manufacturable device platforms. Additive selection determines the facet-dependent Au deposition rates and can be used to tailor surface nanostructure shape and texture. In combination with conventional patterning methods, we have also demonstrated the ability to deposit a large area array of shape-controlled, single crystal Au nanopillars, with precise positioning, demonstrating a new level of control in the design and fabrication of nanometer-scale noble metal-based structures. We anticipate that this approach will be exploited for the fabrication of next generation nanoscale plasmonic, photonic, and electronic structures, where the advantages of shape control, reduced optical absorption and resistive losses, local near-field enhancements, or well-defined nanoscale cavities are desired.

References

- (1) E. Ozbay, Plasmonics: Merging photonics and electronics at nanoscale dimensions, *Science* **311**, 189-193 (2006).
- (2) M. Moskovits, The case for plasmon-derived hot carrier devices, *Nat. Nanotechnol.* **10**, 6-8, (2010).
- (3) Mock, M. & Mock, J. J. Shape effects in plasmon resonance of individual colloidal silver nanoparticles. *J. Chem. Phys.* **116**, 6755–6759 (20020415).
- (4) Zhang, A.-Q., Qian, D.-J. & Chen, M. Simulated optical properties of noble metallic nanopolyhedra with different shapes and structures. *Eur. Phys. J. D* **67**, 231 (2013).
- (5) Xia, Y., Xiong, Y., Lim, B. & Skrabalak, S. E. Shape-Controlled Synthesis of Metal Nanocrystals: Simple Chemistry Meets Complex Physics? *Angew. Chem. Int. Ed.* **48**, 60–103 (2009).
- (6) Wiley, W. & Wiley, B. Maneuvering the surface plasmon resonance of silver nanostructures through shape-controlled synthesis. *J. Phys. Chem. B* **110**, 15666–15675 (20060817).
- (7) Sun, Y., Mayers, B. & Xia, Y. Metal Nanostructures with Hollow Interiors. *Adv. Mater.* **15**, 641–646 (2003).
- (8) Kestell, A. E. & DeLorey, G. T. *Nanoparticles: Properties, Classification, Characterization, and Fabrication.* (Nova Science Publishers, Inc., 2010).
- (9) Guo, I. W., Pekcevik, I. C., Wang, M. C. P., Pilapil, B. K. & Gates, B. D. Colloidal core–shell materials with ‘spiky’ surfaces assembled from gold nanorods. *Chem. Commun.* **50**, 8157–8160 (2014).
- (10) Choi, C. & Choi, K. S. Shape control of inorganic materials via electrodeposition. *Dalton Trans.* 5432–5438 (20081028).
- (11) Leordean, C. et al. Multiscale electromagnetic SERS enhancement on self-assembled micropatterned gold nanoparticle films. *J. Raman Spectrosc.* **45**, 627–635 (2014).
- (12) Tian, F., Bonnier, F., Casey, A., Shanahan, A. E. & Byrne, H. J. Surface enhanced Raman scattering with gold nanoparticles: effect of particle shape. *Anal. Methods* **6**, 9116–9123 (2014).

- (13) Niu, Z. & Li, Y. Removal and Utilization of Capping Agents in Nanocatalysis. *Chem. Mater.* 26, 72–83 (2014).
- (14) Israelsen, N. D., Hanson, C. & Vargis, E. Nanoparticle Properties and Synthesis Effects on Surface-Enhanced Raman Scattering Enhancement Factor: An Introduction. *The Scientific World Journal* (2015).
doi:10.1155/2015/124582
- (15) Tilli, M. et al. *Handbook of Silicon Based MEMS Materials and Technologies.* (Elsevier Science, 2009).
- (16) Schroder, S. & Schroder, D. K. *Semiconductor Material and Device Characterization.* (20050407).
- (17) Kerr, K. & Kerr, M. A. Bromide-Assisted Anisotropic Growth of Gold Nanoparticles as Substrates for Surface-Enhanced Raman Scattering. *J. Spectrosc.* 2016, 8 (2016).
- (18) Zheng, K. H., Chou, Y. C., Wu, Y. J. & Lee, Y. T. Raman spectra of benzoic acid enhanced by the silver nanoparticles of various sizes. *J. Raman Spectrosc.* 41, 632–635 (2010).
- (19) Zhao, Z. et al. Octapod iron oxide nanoparticles as high-performance T2 contrast agents for magnetic resonance imaging. *Nat. Commun.* 4, 2266 (2013).
- (20) Fargašová, A. et al. Influence of various chloride ion concentrations on silver nanoparticle transformations and effectiveness in surface enhanced Raman scattering for different excitation wave-lengths. *RSC Adv.* 5, 9737–9744 (2015).
- (21) Kitchens, C. L., McLeod, M. C. & Roberts, C. B. Chloride Ion Effects on Synthesis and Directed Assembly of Copper Nano-particles in Liquid and Compressed Alkane Microemulsions. *Langmuir* 21, 5166–5173 (2005).
- (22) Zhao, L. et al. Tuning the size of gold nanoparticles in the citrate reduction by chloride ions. *Nanoscale* 4, 5071–5076 (2012).
- (23) Ruiz-Agudo, E., Putnis, C. V., Wang, L. & Putnis, A. Specific effects of background electrolytes on the kinetics of step propagation during calcite growth. *Geochim. Cosmochim. Acta* 75, 3803–3814 (2011).
- (24) Anderson, M. W. et al. Predicting crystal growth via a unified kinetic three-dimensional partition model. *Nature* 544, 456–459 (2017).

- (25) Hazen, R. M. & Sholl, D. S. Chiral selection on inorganic crystalline surfaces. *Nat. Mater.* 2, 367–374 (2003).
- (26) Hutchings, G. J. Catalysis by Gold: Recent Advances in Oxidation Reactions. in *Nanotechnology in Catalysis* 39–54 (Springer, New York, NY, 2007). doi:10.1007/978-0-387-34688-5_4
- (27) Yan, W., Overbury, S. H. & Dai, S. Gold Catalysts Supported on Nanostructured Materials: Support Effects. in *Nanotechnology in Catalysis* 55–71 (Springer, New York, NY, 2007). doi:10.1007/978-0-387-34688-5_5
- (28) Zhong, C.-J. et al. Gold-Based Nanoparticle Catalysts for Fuel Cell Reactions. in *Nanotechnology in Catalysis* 289–307 (Springer, New York, NY, 2007). doi:10.1007/978-0-387-34688-5_14
- (29) Kuralkar, M., Ingle, A., Gaikwad, S., Gade, A. & Rai, M. Gold nanoparticles: novel catalyst for the preparation of direct methanol fuel cell. *IET Nanobiotechnol.* 9, 66–70 (2015).
- (30) Thompson, D. T. Using gold nanoparticles for catalysis. *Nano Today* 2, 40–43 (2007).
- (31) Kitaev, V. & Subedi, T. Synthesis of well-defined pentagonally prismatic silver nanoparticles: role of bromide in (100) stabilization and facet preservation. *Chem. Commun.* 53, 6444–6447 (2017).
- (32) Magnussen, O. M., Hagebock, J., Hotlos, J., & Behm, R. J., In situ Scanning Tunnelling Microscopy Observations of a Disorder-Order Phase Transition in Hydrogensulfate Adlayers on Au(111), *Faraday Discuss.*, 94, 329-338 (1992).
- (33) Edens, G.J., Gao, X., Weaver, M. J., The adsorption of sulfate on gold(111) in acidic aqueous media: adlayer structural inferences from infrared spectroscopy and scanning tunneling microscope, *J. Electroanal. Chem.*, 375, 357-366 (1994).
- (34) Ataka, K. & Osawa, M. In Situ Infrared Study of Water-Sulfate Coadsorption on Gold(111) in Sulfuric Acid Solutions, *Langmuir*, 14, 951-959 (1998).

- (35) Venkatachalam, S. and Jacob, T., DFT Studies on the Nature of Coadsorbates on $\text{SO}_4^{2-}/\text{Au}(111)$, *Z. Phys. Chem.* 221, 1393–1406 (2007).
- (36) Kleinert, M.; Cuesta, A.; Kibler, L. A.; Kolb, D. M. In-situ observation of an ordered sulfate adlayer on Au(100) electrodes, *Surf. Sci.*, 1999, 430, L521.
- (37) Cuesta, A.; Kleinert, M.; Kolb, D. M. The adsorption of sulfate and phosphate on Au(111) and Au(100) electrodes: an in situ STM study, *Phys. Chem. Chem. Phys.* 2000, 2, 5690.
- (38) Woodruff D. P. How does your crystal grow? A commentary on Burton, Cabrera and Frank (1951) 'The growth of crystals and the equilibrium structure of their surfaces'. *Philos Trans A Math Phys Eng Sci.* 2015;373(2039):20140230.
- (39) Jian Zhang, Mark R. Langille, Michelle L. Personick, Ke Zhang, Shuyou Li, and Chad A. Mirkin, 'Concave Cubic Gold Nanocrystals with High-Index Facets', *Journal of the American Chemical Society* 2010 132 (40), 14012-14014.
- (40) O. M. Magnussen, Ordered Anion Adlayers on Metal Electrode Surfaces, *Chem. Rev.* 2002, 102, 679–725.
- (41) Pessoa, et al. "Ionic and Radical Adsorption on the Au(Hkl) Surfaces: A DFT Study." *Surface Science*, vol. 606, no. 1 2, 2011, pp. 69–77.

Supplementary Materials

Shape-Controlled Growth of Single Crystal Gold Surface Nanostructures

*Sasan V. Grayli, Xin Zhang, Dmitry Star, Gary W. Leach**

Single crystal silver Ag(100) substrate preparation: Ag(100) deposition was carried out using a Kurt J. Lesker Company PVD-75 thermal

evaporation tool with a base pressure of $<2 \times 10^{-7}$ Torr. Ag (99.99% Kurt J. Lesker Company) was evaporated from an alumina coated tungsten wire basket. The substrate was heated via a backside quartz lamp and the temperature was monitored with a K type thermocouple attached to the backside of the sample chuck assembly. Deposition was carried out at a substrate temperature of 360 °C and a rate of 3 \AA s^{-1} . Prior to Ag deposition, substrates were immersed in either dilute HF acid solutions (10:1 with de-ionized water), or similarly diluted commercial buffered oxide etch solutions (BOE, CMOS Grade, J.T. Baker Inc.), to remove the native oxide layer from the surface of the silicon wafer. All activities, prior to characterization of the films, were carried out under class 100 clean room conditions or better.

Gold (Au) nanopyramid synthesis with sulphate ion (SO_4^{2-}):

The deposition bath was comprised of 0.355 g of NaSO_4 salt is dissolved in 10 ml of 1.0 M pre-made NaOH solution to achieve a 0.25 M SO_4^{2-} concentration. A $1 \times 1 \text{ cm}^2$ Ag(100) substrate is placed in a beaker containing the NaOH- SO_4^{2-} solution. 500 μL of a 0.0025 M HAuCl_4 solution is pipetted into the mixture and then the beaker is placed in a water bath. The temperature of the water bath is kept constant at 60°C for the duration of the deposition (typically 2 hours). The sample is washed thoroughly by distilled water for 2 minutes followed by sonication in isopropanol alcohol (IPA) for 1 minute and rinsed again with water for 1 minute and then air dried.

The growth of Au at higher concentrations of SO_4^{2-} (0.5 M and 0.75 M) was also investigated with the same duration and deposition temperature. Figure 50 illustrates the top view SEM of the Au nanocrystallites grown under the influence of 0.5 M and 0.75 M SO_4^{2-} , respectively.

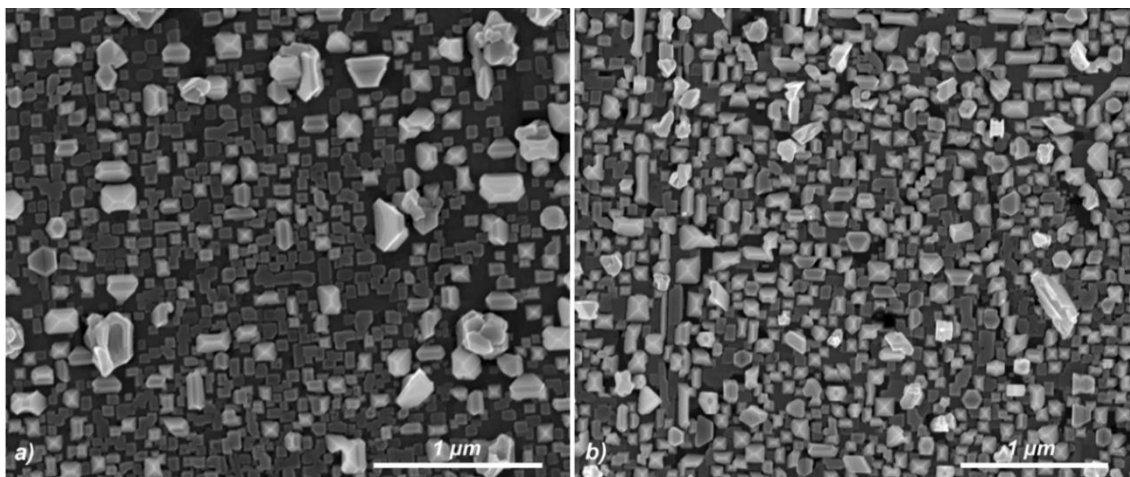


Figure 50. Top-view SEM images of Au grown under the influence of SO_4^{2-} at a) 0.5 M concentration and b) 0.75 M concentration.

Au growth under influence of chloride ion (Cl^-): A 0.25 M Cl^- containing bath is prepared by dissolving 0.146 g of NaCl in 10 ml of 1.0 M NaOH. The Ag(100) substrate (1 x 1 cm² in dimension) is placed in the solution and then 500 μL of HAuCl_4 with 0.0025 M concentration is pipetted into the bath. The beaker containing the Au^{3+} -NaOH- Cl^- mixture is then placed in a water bath at a temperature of 50°C. The duration of the deposition is 3 hours, during which the temperature is kept constant at 50°C. The sample is then removed from the solution, washed for 2 minutes in distilled water, sonicated in IPA for 1 minute, rinsed with distilled water for 1 minute and then air dried.

Au growth under influence of bromide ion (Br^-): A 0.75 M Br^- containing bath is prepared by dissolving 0.771 g of NaBr in 10 ml of 1.0 M NaOH. The Ag(100) substrate (1 x 1 cm² in dimension) is placed in the solution and then 500 μL of HAuCl_4 with 0.0025 M concentration is pipetted into the bath. The beaker containing the Au^{3+} -NaOH- Br^- mixture is placed in a water bath that has been heated to 60°C and is maintained at this temperature during the 2 hour deposition period. Finally, the sample is washed for 2 minutes in distilled water,

sonicated in IPA for 1 minute, rinsed with distilled water for 1 minute and then air dried.

Au growth under influence of Cl^- and SO_4^{2-} ions: A bath containing 0.25 M Cl^- ions and 0.25 M of SO_4^{2-} ions is prepared by dissolving 0.146 g of NaCl and 0.355 g of NaSO_4 in 10 ml of 1.0 M NaOH. The Ag(100) substrate ($1 \times 1 \text{ cm}^2$ in dimension) is placed in the solution and then 500 μL of HAuCl_4 with 0.0025 M concentration is pipetted into the bath. The duration of deposition is 3 hours which is carried out by placing the beaker containing the ionic mixtures in a water bath maintained at 50°C . The sample is then removed from the solution, washed for 2 minutes in distilled water, sonicated in IPA for 1 minute, rinsed with distilled water for 1 minute and then air dried.

Au growth under influence of Br^- and SO_4^{2-} ions: A bath containing 0.75 M of Br^- ions and 0.25 M of SO_4^{2-} ions is prepared by dissolving 0.771 g of NaBr and 0.355 g of NaSO_4 in 10 ml of 1.0 M NaOH. The Ag(100) substrate ($1 \times 1 \text{ cm}^2$ in dimension) is placed in the solution and then 500 μL of HAuCl_4 with 0.0025 M concentration is pipetted into the bath. The beaker containing the solvated ions is then placed in a water bath at a temperature of 60°C . The duration of the deposition is 2 hours during which the temperature is kept constant at 60°C . The sample is then removed from the solution, washed for 2 minutes in distilled water, sonicated in IPA for 1 minute, rinsed with distilled water for 1 minute and then air dried. This process led to the formation of surface nanostructures with Au(110) facets. Figure 51 shows a top-view SEM image of the nanostructures grown in proximity to the edge of the substrate (known with respect to the [110] direction of the Si(100) wafer). On the basis of this image, we are able to assign unambiguously the orientation of the nanostructure angled side walls to be the family of (110) crystalline facets

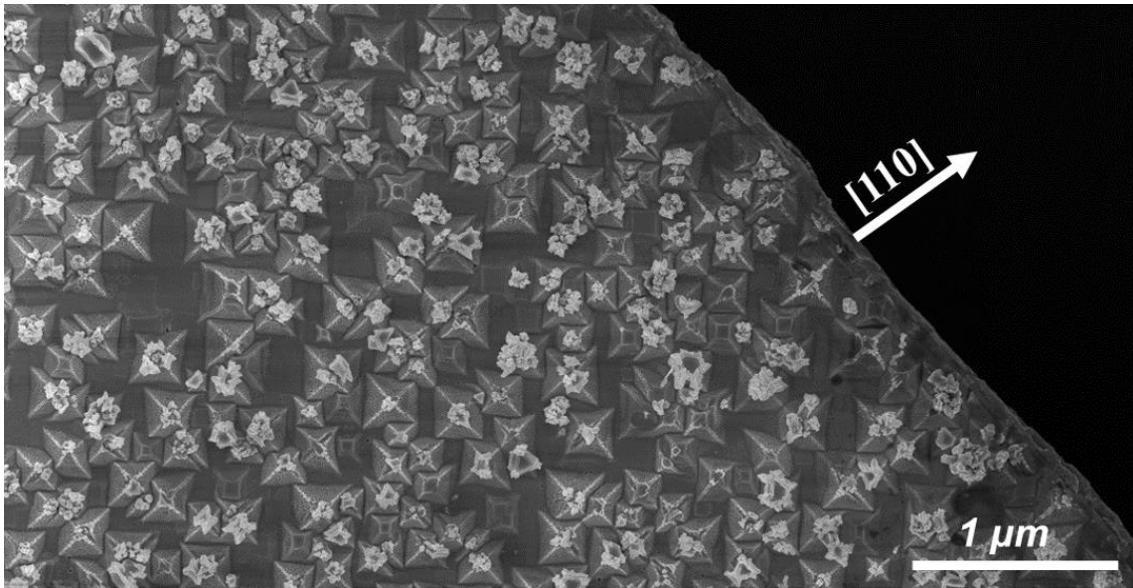


Figure 51. *The growth of Au under the influence of Br^- and SO_4^{2-} leads to the formation of 3-D square pyramidal surface nanostructures with primary (110) facets. Their orientation can be assigned based on the orientation that they have with respect to the edge of the Si(100) substrate which is cut along the 4-fold [110] directions.*

Single crystal Au(100) substrate preparation: A $1 \times 1 \text{ cm}^2$ Ag(100) was used as a substrate to grow 200 nm thick single crystal Au(100) electrolessly. The Ag substrate was submerged in 10 mL of 1 M NaOH which acted as the deposition bath. Then, 250 μL of 0.025 M of HAuCl_4 solution was added to the deposition bath (10 mL NaOH). A beaker containing the solution was placed in a water bath where its temperature was kept at 70°C for 60 minutes undisturbed to grow 200 nm thick single crystal Au(100) film on the Ag(100) substrate. The sample was then washed with distilled water and sonicated in isopropanol alcohol for 60 s and air dried. Single crystal deposition was confirmed through 2D-XRD and high resolution TEM analysis.

Nano-electrode array patterning using electron-beam lithography (EBL): The nano-electrode arrays were made by patterning $500 \times 500 \mu\text{m}^2$ areas on an electron-sensitive poly(methyl methacrylate) (PMMA) A4, which was deposited at 4000 rpm onto a $1 \times 1 \text{ cm}^2$ single crystal Au(100) substrate to achieve 200 nm thickness followed by 4 minutes of soft bake at

180°C, using a Raith e-LiNE EBL system. The electron exposure was done at 7 mm working distance, with 20 μm aperture, 20kV extra high tension (EHT) and with area dose of $1.0 \times 200 \mu\text{C}/\text{cm}^2$. After the patterning, the PMMA was developed in MIBK-IPA 3:1 for 120 s followed by 120 s of IPA rinse [Figure 52].

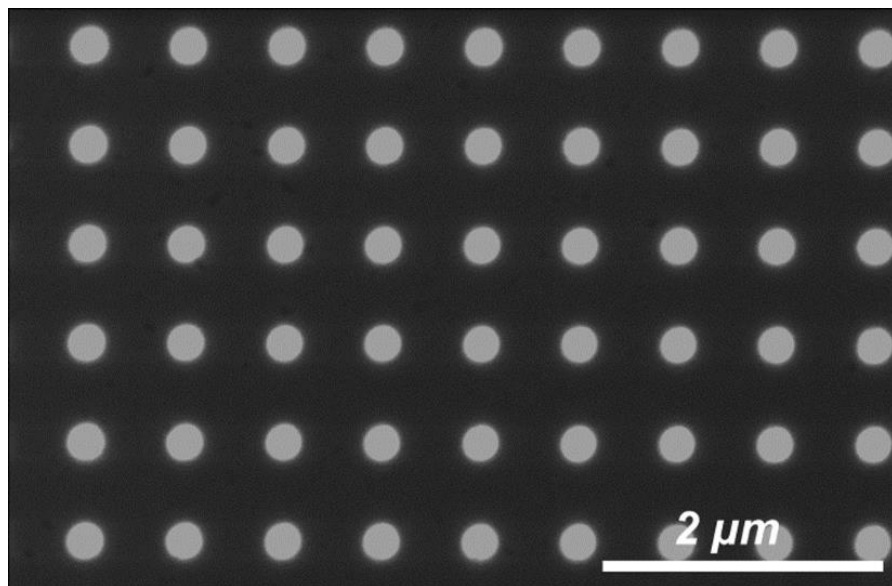


Figure 52. Top-view SEM image of nano-electrode array on PMMA A4 after development with 250 nm hole diameter.

Au growth in nano-electrode arrays: Growth of periodic crystalline nanostructures was carried out by pipetting 250 μL of 0.025 M HAuCl_4 into 10 ml of NaOH (1.0 M) to prepare the deposition bath and inserting the nano-electrode array into the solution. The beaker containing the nano-electrode array was then placed in the 60°C hot water bath for 5 minutes. The sample was then removed, washed for 2 minutes in distilled water, 1 minute with IPA and then placed in acetone for 2 minutes while being sonicated to remove the PMMA mask. After the PMMA lift-off, the sample was rinsed with water and air dried.

Rhodamine 6G (R6G) preparation for surface enhanced Raman spectroscopy (SERS): A R6G solution was prepared by dissolving 0.0470 g of the powdered dye (Eastman) in 10 mL of methanol to achieve 0.01 M concentration.

Benzoic acid (BA) preparation for SERS: The BA solution was prepared by dissolving 0.0488 g of BA solid powder (Coleman & Bell) in 20 mL of methanol to achieve 0.02 M concentration.

Sample preparation for transmission electron microscopy

(TEM): For TEM analysis, a small section of the sample was lifted-out and mounted on a TEM grid. First, a $10 \times 6 \mu\text{m}^2$ area was covered with the platinum-based protective layer using a FEI Helios focused-ion beam (FIB). Then, the desired section with a volume of $10 \times 6 \times 5 \mu\text{m}^3$ is carved out using ion-beam milling, and mounted on a transport needle followed by transferring the sample by gluing it onto a copper TEM grid. The sample then was thinned down to a thickness of roughly 30 nm. Figure 53 shows the scanning-electron microscope (SEM) image of the sample attached to the TEM grid prior to the thinning process. TEM was performed using a 200 kV FEI Tecnai Osiris S/TEM tool.

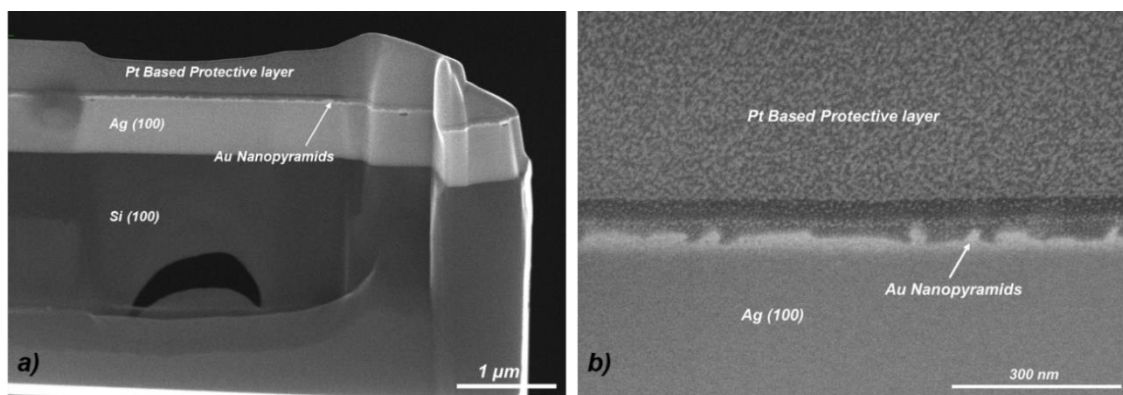


Figure 53. SEM image of the sample suspended on the TEM grid, a) cross-sectional SEM of the lifted-out sample and b) SEM image of a zoomed-in region of the sample shown in a).

Nanopyramid surface absorption measurement: Absorbance of the pyramidal surface nanostructures fabricated by depositing Au under the influence of SO_4^{2-} was measured by placing the sample in an integrating sphere and directing the beam of a broadband light source into the sphere and illuminating the surface nanostructures with a spot size of 1 mm in diameter. The

scattered photons from the surface were collected by a fiber optic and directed to a spectrometer. The absorption from the surface is shown in Figure 54.

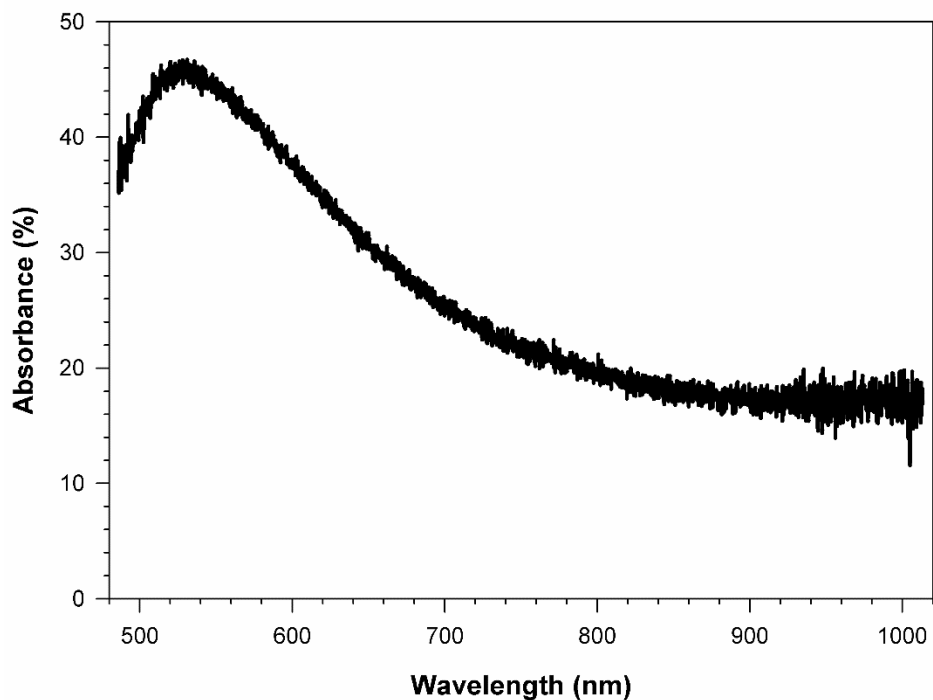


Figure 54. Integrating sphere nanopyramid absorbance measurement. The SERS spectra described in the text were collected with a 785 nm excitation wavelength, the surface had demonstrated up to 20% absorption.

High Efficiency, Single Crystal, Plasmonic Gold Nano-Antennas via Epitaxial Electroless Deposition

Authors' contributions:

S.V.G. and G.W.L conceived and designed the experiments, S.V.G. performed the single crystal Au film growth, vapor deposition of polycrystalline Au, bowtie nano-antennas design and fabrication, FDTD simulation, SERS experiments, SEM imaging, S.K. performed laser scanning 2PPL microscopy experiments and analyses G.W.L. wrote the manuscript with input from all.

6. High Efficiency, Single Crystal, Plasmonic Gold Nano-Antennas via Epitaxial Electroless Deposition

Abstract: Material quality can play a critical role in the performance of nanometer-scale plasmonic device structures. Here, we compare the yield, durability and efficiency of bowtie nano-antennas fabricated from monocrystalline and polycrystalline gold films using subtractive nanofabrication. Focused ion beam milling of monocrystalline Au(100) films deposited through epitaxial electroless deposition to form bowtie nano-antennas results in devices that demonstrate significant performance enhancements compared to devices patterned identically from polycrystalline Au films deposited through conventional physical vapor deposition methods. Single crystal bowtie antennas reveal improvements in pattern transfer fidelity, confinement of local gap fields, the ability to tailor and model local field enhancements, as well as improved thermal and mechanical stability. This work demonstrates the performance advantages of single crystal nanoscale plasmonic materials and highlights a novel deposition strategy for scalable single crystal noble metal deposition. We anticipate that this approach will be broadly exploited for future plasmonic nanostructured device fabrication applications.

Material quality and crystallinity can play an important role in the activity and efficiency of plasmonic structures. The coupling of extended electromagnetic waves to planar metal/dielectric interfaces through surface plasmon polaritons (SPPs) or to nanometer-scale metal structures through locally resonant surface plasmons (LRSPs) leads to confined and amplified local fields that can be exploited for application in energy harvesting, catalysis, strong coupling, etc. The fate of these surface plasmon (SP) excitations is intimately linked with the characteristics of the materials that support them.⁷⁻¹² SPP propagation lengths and SP dephasing and decay times are influenced strongly by material crystallinity and scattering processes that are facilitated by material

defects, grain boundaries, and other forms of surface texture. Single crystal plasmonic structures are expected to yield advantages over their polycrystalline analogues through reductions in optical absorption loss, grain boundary scattering and dissipation, while providing enhanced local fields derived from well-defined faceted nanostructures.

Conventional deposition of plasmonic metals such as gold is typically carried out through physical vapor deposition techniques and generally yields polycrystalline metal films and nanostructures. While deposition strategies and other protocols to mitigate the polycrystalline character of these films have been developed (Norris ETH PVD, template stripping), polycrystalline metal deposition can lead to compromised fabrication yields,^{7,10} as well as loss and dissipation that result in device inefficiency, and remains a significant challenge in the field. We have recently developed an alternative approach to ultrasmooth monocrystalline Au(100) films via electroless deposition from alkaline solutions of common gold salts onto Ag(100)/Si(100) substrates. The method is scalable to the wafer level, environmentally friendly, and represents a promising new approach to the integration of noble metal-based plasmonic structures into CMOS compatible devices architectures (see chapter4). Here, we use this approach to fabricate 100 nm thick single crystal Au(100) films to fabricate bowtie nano-antenna devices by subtractive patterning. Focused ion beam (FIB) milling of these single crystal films results in high quality, low defect density, monocrystalline bowtie antenna structures. By contrast, we have also deposited 100 nm thick polycrystalline gold films by evaporation, utilizing a Si(100) wafer with a 5 nm Cr adhesion layer as a substrate (supporting information), and patterned them identically through gallium ion beam milling. In this manuscript, we employ these bowtie antennas to provide a direct comparison between the performance of single crystal and polycrystalline plasmonic devices.

Bowtie nano-antenna devices were fabricated by a Thermo Fisher Helios NanoLab 650 SEM/FIB system, using a focused gallium ion beam. Figure 55a-b illustrate the sequential milling of material as the focused gallium ion beam is moved over surface regions in a serial fashion to create the bowtie nano-antenna structures on the surface. Figure 55c shows a plan view SEM of the milled single crystal (left) and polycrystalline (right) bowtie structures.

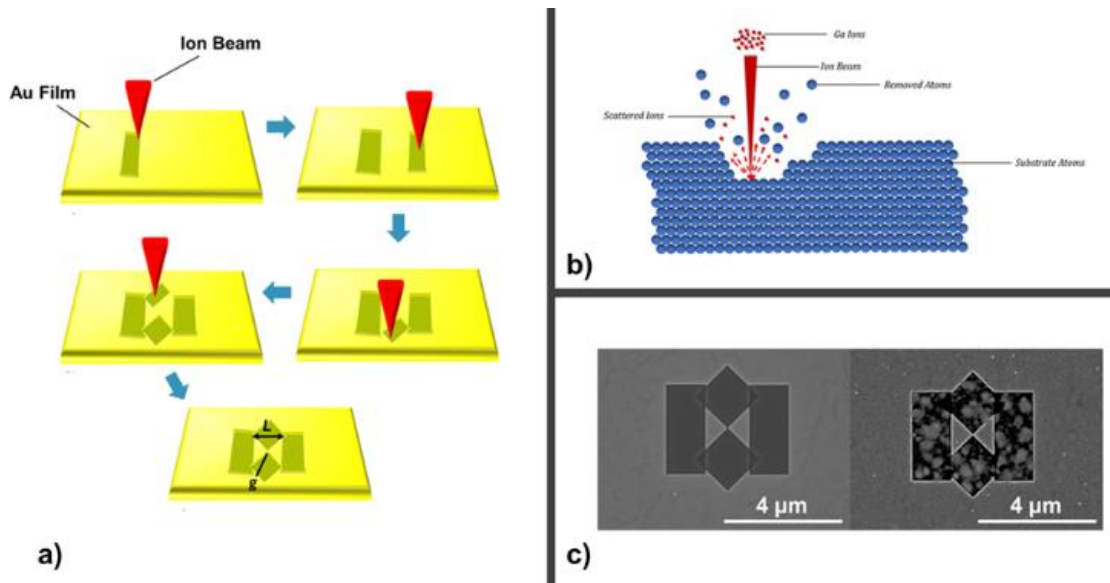


Figure 55. a) Fabrication steps of a bowtie nano-antenna on gold, that involves FIBing away two rectangles and squares to form the basis and the sides of the triangles, b) shows the FIB mechanism for milling, c) shows the SEM images bowtie antennas made on a monocrystalline (left) and polycrystalline (right) Au film respectively

The images reveal significant differences in the quality of pattern transfer, with the milled regions of the monocrystalline film appearing highly uniform, and those of the polycrystalline film much more irregular by contrast. The lack of milling uniformity in the polycrystalline films results from anisotropic, crystal direction-dependent ion milling rates and provides a bowtie structure defined by the remaining non-milled area, surrounded by a region of recessed roughened gold. Note that the pattern generation scheme involved milling rectangular and diamond regions sequentially. This process yields milled regions surrounding the bowtie that lie at different depths within the film and which are separated by small vertical step edges. These regions can be seen readily (Fig 55c, left) in the areas of overlap of the rectangular and diamond regions. The dimensions of the milled geometrical features were chosen to create a bowtie antenna with a length, $L = 1560 \text{ nm}$, a gap, $g = 20 \text{ nm}$, and height, $h = 50 \text{ nm}$. The bowtie nano-antenna dimensions were selected so that they could be resonantly excited with available 780 nm laser radiation to activate the devices and produce a gap field at the antenna feedpoint.

6.1. Yield and Activity as a Function of Film Quality

Focused ion beam milling of 3×10 bowtie nano-antenna arrays was performed on single crystal and polycrystalline gold films. The performance of the bowtie arrays was assessed with a Zeiss scanning laser microscope (SLM) equipped with a 63x objective lens, and a wavelength tunable Coherent Chameleon ultrafast oscillator (75 MHz repetition rate, 140 fs pulse duration) used to activate the antennas. Resonant excitation of the bowtie nano-antennas leads to two-photon photoluminescence (2PPL) that is well-correlated with the locally resonant surface plasmon excitation of the structures. 2PPL imaging has been used extensively to characterize the resonant behaviour of plasmonic nanostructures³⁰⁻³⁴ and is used here as a measure of the nano-antenna plasmonic response and local field enhancement. These structures provide a stringent test of fabrication precision and yield, with the goal of uniform, reproducible and intense local gap fields at the antenna's feedpoints.

2PPL intensity maps of the bowtie arrays induced by 780 nm laser excitation are presented in Figure 56 and highlight the primary performance differences between the mono- and polycrystalline nano-antennas. The 2PPL maps demonstrate that fabrication yield is greatly impacted by the material quality and resulting pattern transfer characteristics. The yield of monocrystalline bowtie antennas is close to 100% as measured by the appearance of an enhanced confined local near-field resulting in 2PPL intensity at the 20 nm wide antenna feed points, and the relative uniformity of this 2PPL intensity for the vast majority of antennas, (Fig 56a). Structures fabricated identically but with polycrystalline-deposited gold (Fig 56b), show poor fabrication yield with few devices showing near-field intensity enhancements at the antenna feed points, and of these, little uniformity in 2PPL intensity. Note that fabrication differences between the mono- and polycrystalline structures (e.g. the presence of a Cr adhesion layer in the case of the polycrystalline antennas) can potentially lead to differences in the resonant response characteristics of the antennas.

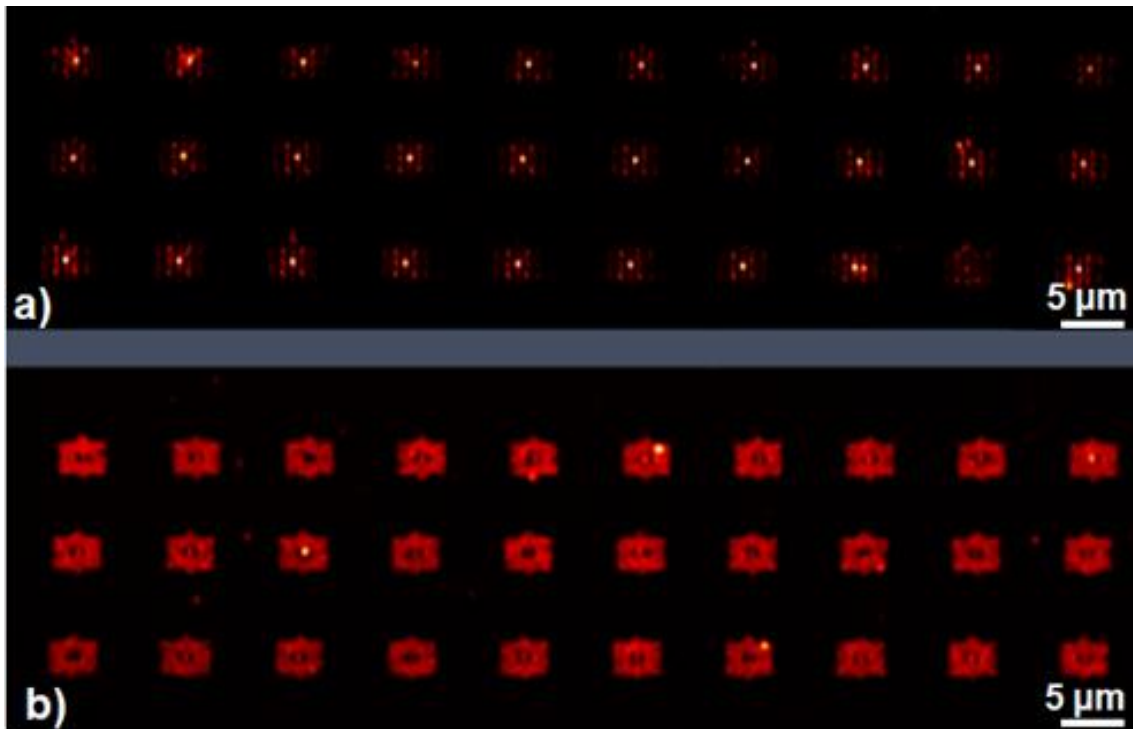


Figure 56. Yield and functionality of bowtie nano-antennas as function of film quality have been demonstrated. Simultaneous excitation of 30 bowtie nano-antennas made on a) single crystal Au film, b) multi-crystalline film.

However, scanning of the laser wavelength in the vicinity of the expected resonant excitation wavelength did not yield improvements in the emission characteristics of the polycrystalline antennas.

2PPL emission from the polycrystalline antennas (Fig 56b), in contrast, shows poor fabrication yield with few antenna structures displaying 2PPL gap intensity. While the integrated emission intensity from the polycrystalline antennas appears brighter than that from single crystal devices, the vast majority of the 2PPL emission from polycrystalline devices emanates from the roughened recessed regions surrounding the bowties, and not from the antenna's feedpoints, as desired. This "background" emission results from the roughened nature of the surrounding regions, as SP's scatter from polycrystalline grain boundaries and material defects that arise from non-uniform and anisotropic milling. Further, the bright, localized 2PPL emission from monocrystalline antenna feedpoints, is significantly more intense than the average level of background

emission emanating from polycrystalline devices, reflecting larger and more uniform field enhancement factors in the single crystal bowtie gaps.

6.2. Polarization Dependence of the Nano-Antennas

The activity of the 2D bowtie structures are known to be highly polarization sensitive. The bowtie nano-antennas fabricated on mono- and polycrystalline Au films were studied under vertically- and horizontally-polarized 780 nm laser irradiation at normal incidence. Their polarization-dependent 2PPL emission characteristics are illustrated in Figure 57, along with a numerical simulation of the anticipated response calculated using a finite difference time domain (FDTD) model of the bowtie structures (Lumerical). To compare the modelled and the experimentally measured antenna response accurately, the geometrical shapes employed in the FIB milling protocol of the fabricated devices were used to design the nano-antennas for the FDTD software model.

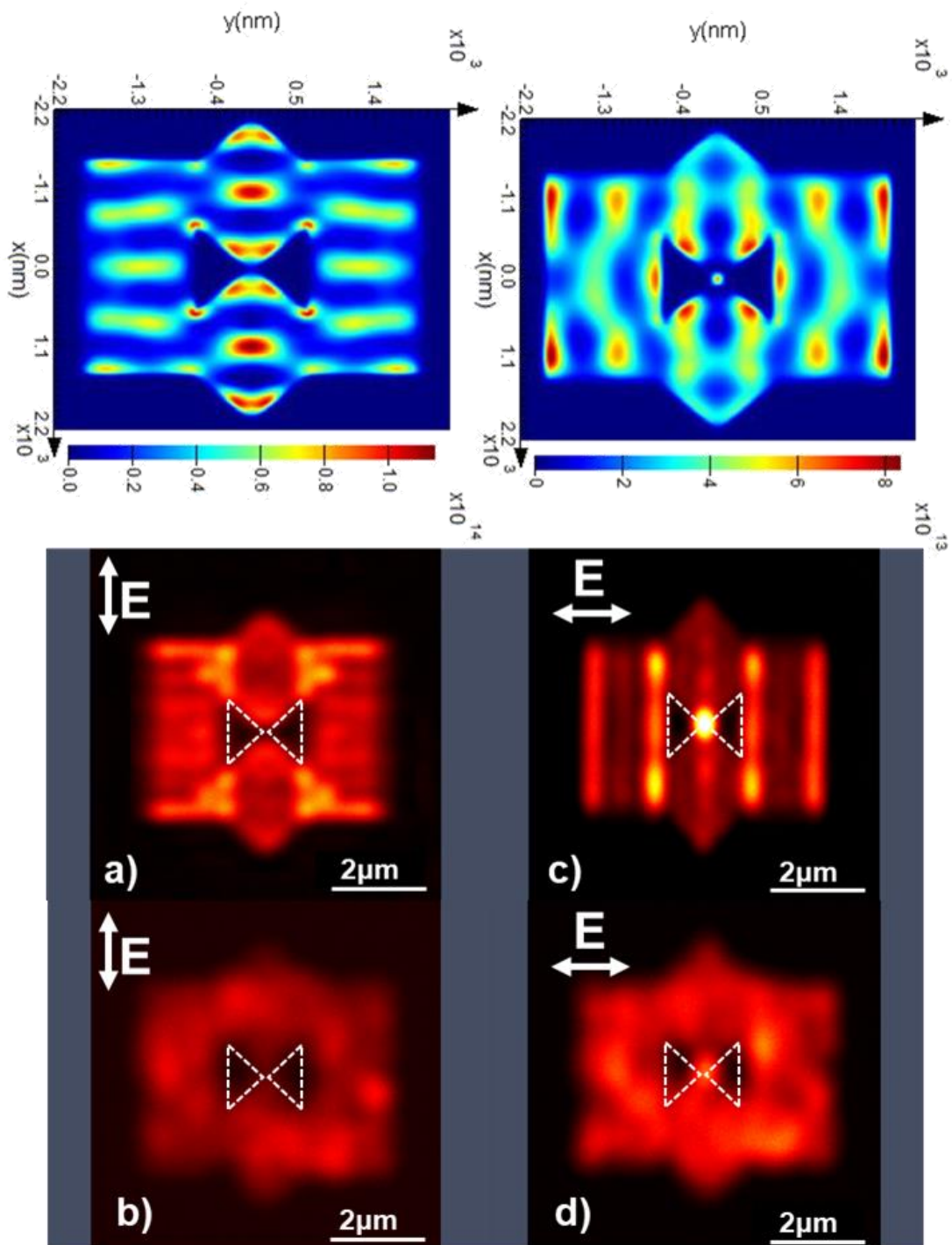


Figure 57. The effect of polarization on the activity of bowtie nano-antennas is shown. a) and b) FDTD modeled antenna for horizontally and vertically polarized excitation respectively. Monocrystalline bowtie nano-antenna (c) and d)) and polycrystalline bowtie nano-antenna (e) and f)) for horizontally and vertically polarized excitation respectively.

The simulated bowtie nano-antennas (Fig 57a) were excited with a plane wave pulse centered at 800 nm with a 100 nm bandwidth for both vertically- and horizontally-polarized light with respect to the bowties. The results presented in Fig 57a-b represent the device response at 780 nm - the same wavelengths used for excitation of the fabricated bowties. As anticipated, the electric field distribution across the device is polarization sensitive, and shows field maxima lines that lie orthogonal to the polarization direction. The milling protocol results in the formation of recessed regions of the film that define local plasmonic cavities characterized by sharply-edged walls. Light that is orthogonally-polarized to the wall edges is edge-coupled into these cavities which are capable of supporting SP modes that appear as field intensity maxima in the FDTD simulations. These are readily visible as horizontal intensity maxima in the outer rectangular milled regions of the antenna under vertically-polarized excitation (Fig 57a), and as vertical intensity maxima in the horizontally-polarized excitation (Fig 57b). The mode patterns observed for the simulated milled structures in Fig 57a-b in the immediate vicinity of the bowtie are further complicated by the plasmonic cavities defined by the diamond-shaped milled regions, leading to interference between modes and more complex intensity structure. Note that excitation of the structures with vertically-polarized incident radiation that is orthogonal to the bowtie axis (Fig 57a) results in no gap field at the antenna feedpoint while horizontally-polarized incident radiation results in a confined local field in the bowtie gap.

Comparison of the plasmonic response of the simulated bowties with the fabricated bowties reinforces the significant differences in pattern transfer quality of the mono- and polycrystalline devices. Fig 57c-d display the corresponding 2PPL emission from a single crystal bowtie under vertically- and horizontally-polarized 780 nm short pulse excitation. There is good qualitative, and to some degree quantitative agreement, between the FDTD modelled device response and the experimentally observed 2PPL response. The experimental response displays horizontal intensity maxima upon excitation with vertically-polarized light, and vertical intensity maxima upon horizontally-polarized excitation and is qualitatively similar to those of the FDTD simulations. Fig 57d also shows an intense localized field maximum at the antenna feedpoint upon horizontally-polarized excitation that is absent under vertical light polarization. Note that

some differences between the simulated and measured antenna responses may reflect the narrow bandwidth 780 nm output of the simulation, in comparison to the experimental measurement that employs an ultrafast laser bandwidth of ~10 nm, centered at 780 nm. Finite quality factors of the milled cavities will couple a range of incident wavelengths into the structures that can lead to SP mode interferences. Constructive interference of a range of incident wavelengths may be the reason for the much larger intensity observed at the antenna feedpoint experimentally (Fig 57d) than is simulated (Fig 57b) for horizontal light polarization. Likewise, more complex constructive and destructive interferences resulting from the multiple SP cavities that define the milled structure may contribute to intensity differences observed in other regions.

Comparison of the 2PPL emission response from polycrystalline bowties (Fig 57e-f) shows very modest polarization dependence, the nature of which is significantly different from that observed from the monocrystalline antennas. Poor pattern transfer quality in the polycrystalline antennas leads to little or no well-defined mode structure as observed in the case of the single crystal antennas. Plasmonic excitation and rapid decay through grain boundary and defect induced plasmon dissipation leads to 2PPL “background” emission with little polarization character. However, it should be noted that the overall intensity of 2PPL emission appears to be more intense for horizontally-polarized excitation, presumably due to the enhanced coupling of light that is enabled by the bowtie antenna for this polarization.

Further refinements in film quality, pattern transfer, and simulation accuracy are currently underway in our laboratory to improve the level of agreement between simulated and fabricated structures. Nevertheless, the high quality of material deposition enabled through our electroless deposition process, provides good qualitative agreement between simulation and experiment.

6.3. Device Stability

The effect of material quality on device stability was also investigated. To do so, the 2PPL intensity emanating from bowties was evaluated upon increasing incident

laser intensity. Figure 58 displays a time sequence of 2PPL images of a single monocrystalline (Fig 58a) and polycrystalline (Fig 58b) bowtie as the laser power was increased sequentially every 5 seconds. Each bowtie was illuminated in this period under the same laser scanning microscope scan rate conditions to ensure equivalent exposures for single and polycrystalline devices. The percentage values appearing in each panel of the figure reflect the percentage of total laser output power coupled into the LSM. The actual power incident on the sample through the LSM 63x objective is a small fraction of this intensity, but scales linearly with the displayed percentage, as measured independently in the absence of a sample with a calibrated power meter. As the laser power is increased, both mono- and polycrystalline devices emit increased 2PPL emission intensity as expected, since 2PPL intensity is proportional to I^2 , where I is the local near-field intensity enhancement^{31,32}. The antennas appear to be non-emissive at low incident intensity, however this is misleading, as the 2PPL emission intensities displayed in Fig 58 have been normalized to the maximum emission intensities observed under high intensity illumination. Figure 58 demonstrates that as the incident intensity is systematically increased, so is the bowtie gap intensity. Further increase in incident intensity results ultimately in the catastrophic rupture of the devices as indicated by the loss of bowtie structure and saturated emission intensity in the 2PPL image maps. We attribute the catastrophic destruction of the bowtie structures to plasmonic decay via photo-thermal mechanisms, generating local heating effects that exceed the thermal and mechanical stability of the structures. Inspection of Figure 58 reveals that the threshold incident intensity necessary to induce catastrophic damage under these illumination conditions is approximately ten times greater for single crystal bowtie devices (~45% incident intensity) than for polycrystalline devices (4.5% incident intensity). We attribute this large difference to the presence of grain boundaries and defects in the polycrystalline structures which increase the dissipation of SPs to heat over the entire milled region of the structures (bowtie and background). Further, the polycrystalline structures of these antennas are anticipated to be less thermally and mechanically stable than their corresponding single crystal counterparts, leading to lower thresholds for bowtie destruction. The absence of grain boundaries in the monocrystalline Au films does not provide such a path for such distributed SP photothermal decay. Further, incident SP decay in single crystal structures can be mediated by additional longer range mechanisms of thermal conduction (e.g. via

phonon dissipation) that are unavailable in polycrystalline structures comprised of nanoscale grains. Thus, our stability study indicates that the single crystal bowtie structures can support ~ 10 times more incident illumination intensity, (corresponding to a 10^2 local intensity enhancement, and therefore, 10^4 local field enhancement), beyond that of polycrystalline bowties, before irreversible and catastrophic loss.

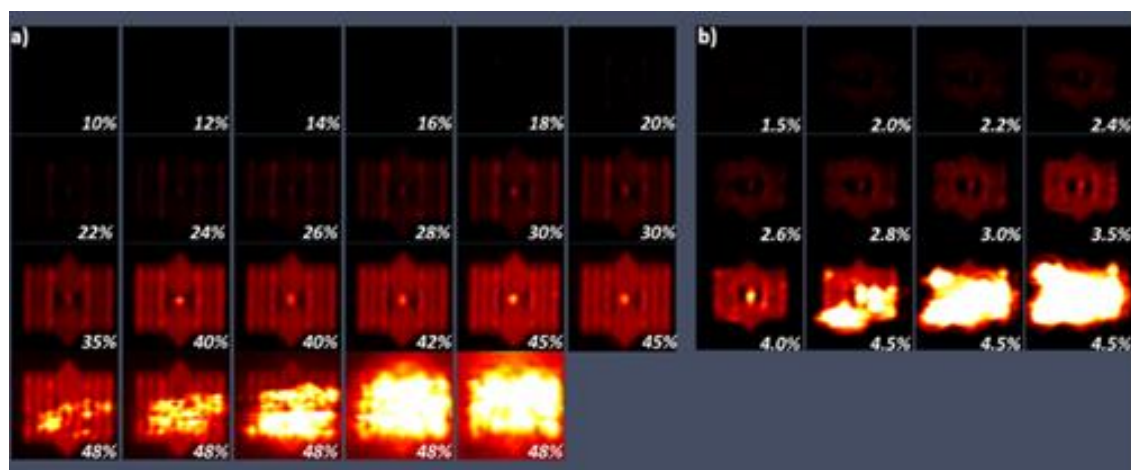


Figure 58. Effect of film quality on bowtie nano-antenna stability. The device stability of a) monocrystalline bowtie antenna and b) polycrystalline bowtie antenna as the incident laser power is sequentially increased. Both devices were excited by a 780nm, 120 fs pulse duration laser. Percentages reflect the fraction of maximum incident laser intensity.

6.4. Plasmonic Activity and Field Enhancement

Surface enhanced Raman spectroscopy (SERS) is a well-known and well-studied process in which the local excitation of SPs leads to a significant enhancement in the Raman scattered light collected from surface molecules^{14–18}. The locally excited electric field and the Raman enhancement can be achieved using nanoparticles, nanostructures made from plasmonic noble metals,^{17–19} or with the help of nano-scaled devices with resonating cavities that can confine the excited SPs within very small gaps^{20–28}. Here, the SERS response from the common Raman reporter molecule benzoic acid (BA) is used to compare the SERS efficiency as a measure of the relative magnitude of the field confinement for mono- and polycrystalline bowtie nano-antennas. In a receiving antenna,

the maximum power gain is directly related to the maximum effective area of the antenna, A_e , which is calculated through:

$$A_e = \frac{\lambda^2}{4\pi} \quad (1)$$

where λ is the wavelength of the incident photon²⁹. The field confinement magnitude at the gap of the plasmonic bowtie nano-antennas is linked to the coupling efficiency of photons to SPs, which in turn, is a function of surface quality of the film from which the device is made^{7,10–12}. The surface roughness of the polycrystalline devices negatively impacts the intensity of excited SPs at the bowtie feedpoint by enabling photon-SP decoupling at grain boundaries and material defects, thereby reducing the magnitude of the field at the gap. This route for SP intensity decay is minimized for the monocrystalline Au nano-antennas, resulting in a larger gap field.

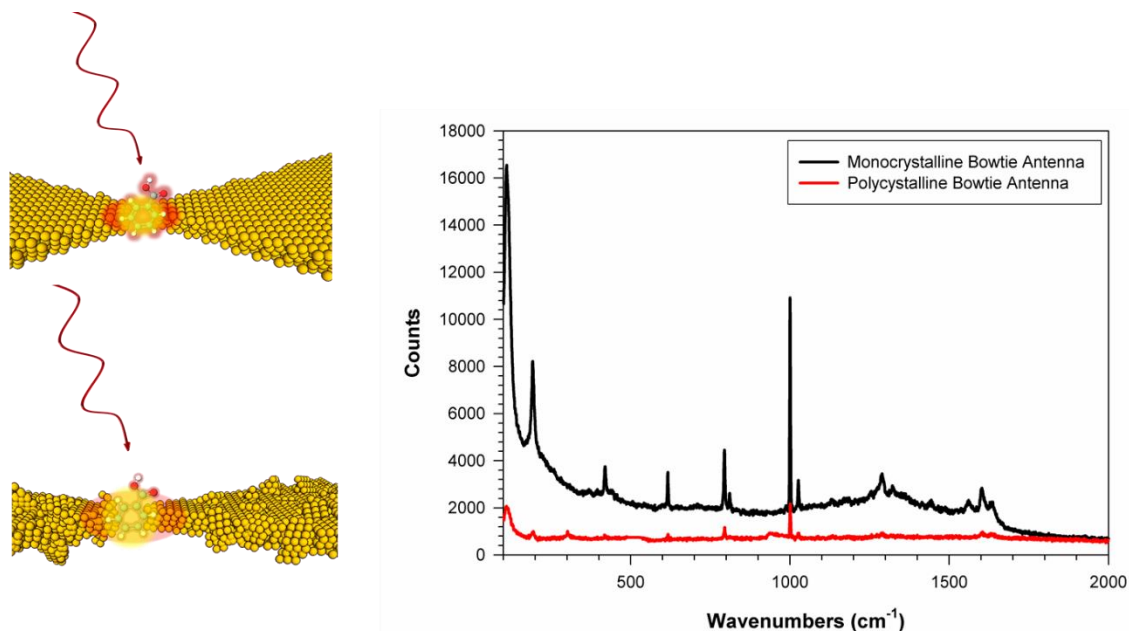


Figure 59. Surface enhanced Raman spectra of benzoic acid from a) monocrystalline Au bowtie nano-antenna and b) polycrystalline Au bowtie nano-antenna, are shown and compared in c). The SERS was carried out by a Renishaw Raman microscope (785 nm).

Both mono- and polycrystalline devices were coated with 10 μ L of 0.02 M BA in methanol, by drop casting, followed by solvent evaporation. SERS was carried out using a Renishaw Invia Raman microscope and a fiber coupled continuous wave 785 nm diode laser, as the excitation source. The Raman spectra were collected at 50% incident

laser intensity with a 10s exposure time. The bowties were far enough apart from one another that Raman data from single devices could readily be acquired. The SERS spectra from BA coated bowties appear in Figure 59 and are representative of the mono- and polycrystalline responses from many bowtie measurements. The data suggest that the larger observed SERS enhancement from single crystal antenna can be attributed to the quality of the Au film on which the devices were fabricated and that single crystal nanostructures support larger near-field gap intensities than their polycrystalline counterparts, suggesting significant advantages in the use of single crystal plasmonic materials.

6.5. Conclusion

We have presented a direct comparison of the performance of mono- versus polycrystalline plasmonic bowtie nano-antennas. Single crystal bowties were fabricated via FIB milling of Au films deposited by epitaxial electroless deposition in alkaline environments onto Ag(100)/Si(100) substrates. Polycrystalline antennas were fabricated through an identical patterning protocol on polycrystalline films deposited by Au evaporation onto a Si(100) wafer containing a 5nm thick Cr adhesion layer. The quality and yield of pattern transfer onto single crystal films far surpasses that of polycrystalline films and leads to significant performance advantages of the single crystal devices. These include the uniformity, and intensity of local near-field distributions, the ability to model accurately these distributions, and the resulting stability of single crystal devices compared to their polycrystalline analogues. Single crystal devices demonstrate the ability to support one order of magnitude more incident intensity (and therefore 10^4 times the local field enhancement) than polycrystalline devices, before their catastrophic loss via photo-thermal decay. This enhanced stability is attributed to the greater thermal and mechanical characteristics of single crystal materials. Single crystal bowties have also been shown to provide a greater SERS enhancement factor than polycrystalline structures through reduced photon-surface decoupling.

In summary, we have demonstrated that the development a new scalable and green solution-deposition method has enabled the fabrication of large area single crystal

Au(100) films for the subtractive manufacture of single crystal plasmonic devices and that there is strong evidence for improved fabrication and performance yields for these single crystal nanoscale plasmonic structures compared to their polycrystalline counterparts.

References

1. Raether, H. *Surface Plasmons on Smooth and Rough Surfaces and on Gratings* Springer.
2. Kretschmann, E., Raether, H. Notizen: Radiative Decay of Non Radiative Surface Plasmons Excited by Light. *Z. Für Naturforschung A* 23, 2135–2136 (2014).
3. Barnes, W. L., Dereux, A. & Ebbesen, T. W. Surface plasmon subwavelength optics. *Nature* (2003). doi:10.1038/nature01937
4. Zhang, Z. & Zhang, J. Surface plasmon polaritons: physics and applications. *J. Phys. Appl. Phys.* 45, 19 (20120321).
5. Kik, P. G. & Brongersma, M. L. *Surface Plasmon Nanophotonics* 1–9 (Springer, Dordrecht, 2007). doi:10.1007/978-1-4020-4333-8_1
6. Pitarke, J. M., Silkin, V. M., Chulkov, E. V. & Echenique, P. M. Theory of surface plasmons and surface-plasmon polaritons. *Rep. Prog. Phys.* 70, 1 (2007).
7. Huang, J.-S. et al. Atomically flat single-crystalline gold nanostructures for plasmonic nanocircuitry. *Nat. Commun.* 1, 150 (2010).
8. Zhang, K. et al. Single-crystal metal growth on amorphous insulating substrates. *Proc. Natl. Acad. Sci.* 201717882 (2018). doi:10.1073/pnas.1717882115
9. Zhou, C., Yu, J., Qin, Y. & Zheng, J. Grain Size Effects in Poly-crystalline Gold Nanoparticles. *Nanoscale* 4, 4228–4233 (2012).
10. Park, J. H. et al. Single-Crystalline Silver Films for Plasmonics. *Adv. Mater.* 24, 3988–3992 (2012).
11. High, A. A. et al. Visible-frequency hyperbolic metasurface. *Nature* 522, 192–196 (2015).
12. Lu, Y.-J. et al. Plasmonic Nanolaser Using Epitaxially Grown Silver Film. *Science* 337, 450–453 (2012).
13. Mattox, D. M. *Handbook of Physical Vapor Deposition (PVD) Processing*. (William Andrew, 2010).

14. Moskovits, M. Surface-enhanced spectroscopy. *Rev. Mod. Phys.* 57, 783–826 (1985).
15. Campion, A. & Kambhampati, P. Surface-enhanced Raman scattering. *Chem. Soc. Rev.* 27, 241–250 (1998).
16. Drachev, V. P. & Shalaev, V. M. Biomolecule Sensing with Adaptive Plasmonic Nanostructures. in *Surface-Enhanced Raman Scattering* 351–366 (Springer, Berlin, Heidelberg, 2006). doi:10.1007/3-540-33567-6_18
17. Corni, S. & Tomasi, J. Studying SERS from Metal Nanoparticles and Nanoparticles Aggregates with Continuum Models. in *Surface-Enhanced Raman Scattering* 105–123 (Springer, Berlin, Heidelberg, 2006). doi:10.1007/3-540-33567-6_6
18. Tian, F., Bonnier, F., Casey, A., Shanahan, A. E. & Byrne, H. J. Surface enhanced Raman scattering with gold nanoparticles: effect of particle shape. *Anal. Methods* 6, 9116–9123 (2014).
19. Kerr, K. & Kerr, M. A. Bromide-Assisted Anisotropic Growth of Gold Nanoparticles as Substrates for Surface-Enhanced Raman Scattering. *J. Spectrosc.* 2016, 8 (2016).
20. Zhang, J. et al. Whispering-gallery nanocavity plasmon-enhanced Raman spectroscopy. *Sci. Rep.* 5, 15012 (2015).
21. Zhan, P. et al. DNA Origami Directed Assembly of Gold Bowtie Nanoantennas for Single-Molecule Surface-Enhanced Raman Scattering. *Angew. Chem. Int. Ed.* 57, 2846–2850 (2018).
22. Simoncelli, S. et al. Quantitative Single-Molecule Surface-Enhanced Raman Scattering by Optothermal Tuning of DNA Origami-Assembled Plasmonic Nanoantennas. *ACS Nano* 10, 9809–9815 (2016).
23. Kühler, P., Weber, M. & Lohmüller, T. Plasmonic Nanoantenna Arrays for Surface-Enhanced Raman Spectroscopy of Lipid Molecules Embedded in a Bilayer Membrane. *ACS Appl. Mater. Interfaces* 6, 8947–8952 (2014).
24. Kahraman, M., Tokman, N. & Çulha, M. Silver Nanoparticle Thin Films with Nanocavities for Surface-Enhanced Raman Scattering. *ChemPhysChem* 9, 902–910 (2008).

25. Zhang, J., Irannejad, M. & Cui, B. Bowtie Nanoantenna with Single-Digit Nanometer Gap for Surface-Enhanced Raman Scattering (SERS). *Plasmonics* 10, 831–837 (2015).
26. Jäckel, F., Kinkhabwala, A. A. & Moerner, W. E. Gold bowtie nanoantennas for surface-enhanced Raman scattering under controlled electrochemical potential. *Chem. Phys. Lett.* 446, 339–343 (2007).
27. Feng, L. et al. Silver-coated elevated bowtie nanoantenna arrays: Improving the near-field enhancement of gap cavities for highly active surface-enhanced Raman scattering. *Nano Res.* 8, 3715–3724 (2015).
28. Hatab, N. A. et al. Free-Standing Optical Gold Bowtie Nanoantenna with Variable Gap Size for Enhanced Raman Spectroscopy. *Nano Lett.* 10, 4952–4955 (2010).
29. Balanis, C. A. *Antenna theory: analysis and design* / Constantine A. Balanis. (John Wiley, 2005).
30. M. R. Beversluis, A. Bouhelier, & L. Novotny, Continuum generation from single gold nanostructures through near-field mediated intraband transitions. *Phys. Rev. B* 68, 115433 (2003).
31. K. Imura, T. Nagahara, & H. Okamoto, Plasmon mode imaging of single gold nanorods. *J. Am. Chem. Soc.* 126, 12730–12731 (2004).
32. P. Mühlischlegel, H-J. Eisler, O. J. F. Martin, B. Hecht, & D. W. Pohl, Resonant optical antennas. *Science* 308, 1607–1609 (2005).
33. P. Ghenuche, S. Cherukulappurath, T. H. Taminiau, N. F. van Hulst, & R. Quidant, Spectroscopic mode mapping of resonant plasmon nanoantennas. *Phys. Rev. Lett.* 101, 116805 (2008).
34. J-S. Huang, et al. Atomically flat single-crystalline gold nanostructures for plasmonic nanocircuitry, *Nat. Comm.*, DOI: 10.1038/ncomms1143 (2010).

Supplementary Materials

High Efficiency, Single Crystal, Plasmonic Gold Nano-Antennas via Epitaxial Electroless Deposition

*Sasan V. Grayli, Saeid Kamal, Gary W. Leach**

Monocrystalline Silver Deposition on Silicon

Silver Ag(100) deposition was carried out using a Kurt J. Lesker Company PVD-75 thermal evaporation tool with a base pressure of $<2 \times 10^{-7}$ Torr. Ag (99.99% Kurt J. Lesker Company) was evaporated from an alumina coated tungsten wire basket. The substrate was heated via a backside quartz lamp and the temperature was monitored with a K type thermocouple attached to the backside of the sample chuck assembly. Deposition was carried out at a substrate temperature of 340 °C and a rate of 3 Å/s. Prior to Ag deposition, substrates were immersed in either dilute HF acid solutions (10:1 with de-ionized water), or similarly diluted commercial buffered oxide etch solutions (BOE, CMOS Grade, J.T. Baker Inc.), to remove the native oxide layer from the surface of the silicon wafer. All activities, prior to characterization of the films, were carried out under class 100 clean room conditions or better.

Electroless Deposition of Monocrystalline Gold on Silver

A 1 x 1 cm² Ag(100) substrate was used as surface on which to grow a 200 nm thick monocrystalline Au(100) film electrolessly. The Ag substrate was submerged in 10 mL of 1 M NaOH which acted as the deposition bath. Then 250 µL of 0.025 M of HAuCl₄ solution was added to the deposition bath (10 mL NaOH). The solution was placed in a water bath where its temperature was kept at 70°C for 60 minutes undisturbed to grow a 200 nm thick monocrystalline Au(100) film on the Ag(100)/Si(100) substrate. The

sample was then washed with distilled water and sonicated in isopropanol alcohol for 60 s and air dried.

Bowtie Gold Nano-Antenna Fabrication

An FEI Helios Focused-Ion beam (FIB) tool (4D LABS) was used to fabricate the gold bowtie nano-antennas. The process was carried under the pre-set conditions in the tool for Au films, in which the desired milling depth was 50 nm. The ion beam current was set at 7.7 pA for the 30 kV operating voltage. Under these conditions, for 50 nm depth etching the dose was set to be 33 pC/ μm^2 and this value was doubled for the milling the monocrystalline Au film. The exposure time for fabrication of bowtie nano-antennas on the monocrystalline Au film was also increased by a factor of 2 over the parameters used for milling polycrystalline films to achieve a milling depth of 50 nm, due to the lower material removal rate for single crystal Au. Figure 60 shows the fabricated bowtie antenna on both monocrystalline and polycrystalline Au achieved under these etching conditions. The dimensions of the nano-antennas ($L=1560$ nm) was designed to be twice the wavelength of the 780 nm incident photons to achieve efficient coupling.

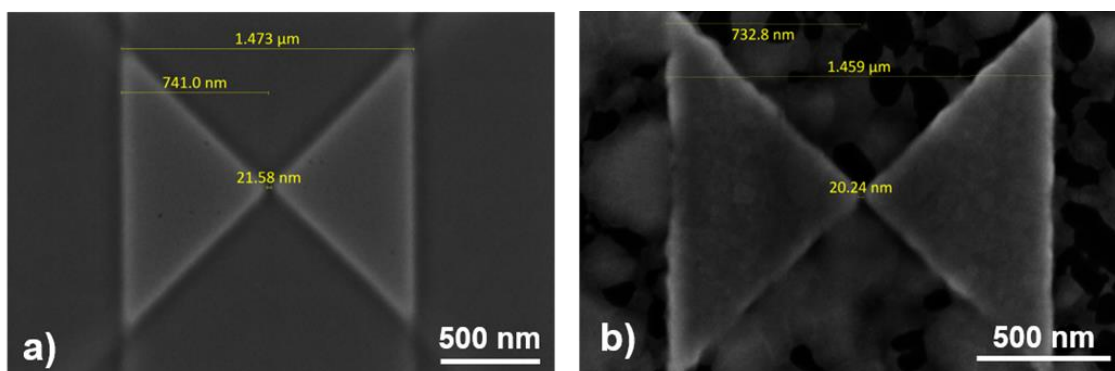


Figure 60. The fabricated Au bowtie nano-antennas on a) monocrystalline Au(100) and b) thermally evaporated polycrystalline Au.

Benzoic Acid (BA) Preparation for SERS

The BA solution was prepared by dissolving 0.0488 g of BA solid powder (Coleman & Bell) in 20 mL of methanol to achieve 0.02 M concentration. From this

solution, 10 μL of BA was drop casted on the bowtie nano-antennas described in this paper

Finite-Difference Time-Domain Simulations

The FDTD analysis was carried out using Lumerical Solutions FDTD tool to simulate the electric field distribution across the surface of the fabricated bowtie for comparison with the experimental results. The design of the structures input to the FDTD model were as close as possible to the fabricated structures for more accurate analysis. The images shown in the figure 57a) and b) of the manuscript, are from a power monitor placed 50 nm above the structure at 0° and 90° polarization respectively. The source used in this simulation was emitting a plane wave with a bandwidth from 730 nm to 830 nm (centered at 800 nm). A uniform mesh with 1 nm x 1 nm x 1 nm size was used over the region under simulation with 1000 fs simulation time. The dimension of the FDTD simulation area was $5 \times 5 \times 2 \mu\text{m}^3$ (3D simulation) and the mesh accuracy of the simulation was set at 5 (“High accuracy”) with “conformal variant 1” for the mesh refinement selection and 0.25 nm minimum mesh step. The boundary conditions were set for the perfect matching layer (“PML”) with 12 pml layers in all directions and 0.0001 pml reflection. The substrate on which the bowtie nano-antenna was designed, was a $10 \times 10 \times 2 \mu\text{m}^3$ cuboid and the selected optical material was “Au (Gold)-CRC”.

Laser Scanning Microscopy

The 2PPL microscopy was performed using a Zeiss LSM 510 MP laser scanning microscope equipped with a 140 fs Chameleon Ultra excitation laser (Coherent) with a 75 MHz repetition rate that was tunable from 710-980 nm. The high-resolution images were collected by an LD Plan-Neofluar 63x/0.75 Korr objective lens while the bowtie nano-antennas were irradiated with 780 nm wavelength.

Surface Enhanced Raman Spectroscopy (SERS)

Surface enhanced Raman spectroscopy SERS was performed with a Renishaw (Invia) Raman microscope/spectrometer equipped with a 785 nm diode laser source (set at 50% of laser power). Raman spectra were acquired using a 50x objective with 10s exposure time acquisitions.

7. Future Work and the Impact of EED

It was shown that EED can have a broad impact in the field of plasmonics by enabling the deposition of ultra-smooth noble metal surfaces. As demonstrated in chapter 3, this process also allows for deposition of very thin layer Au films. Metal films with few monolayer thicknesses can behave as quantum metals where the electronic energy states are more separated and the bulk electron plasma does not have the same density as the thicker metal films¹. As a result such thin film metals have become a major focus in the field of plasmonics and nano-photonics. This chemistry can also be applied to create quantum wells by alternating the deposition of different ultrathin metallic films onto a pre-lithographed nanoelectrode array.

The developed electroless deposition process has exhibited a “healing effect” via filling inter-grain gaps in a polycrystalline metal. The aforementioned effect can be utilized to improve the quality of an underlying polycrystalline metal film by placing the surface in the electrochemical bath presented by this work to improve the surface quality. The figure below shows an e-beam evaporated Au film before and after electroless Au deposition for 60 minutes.

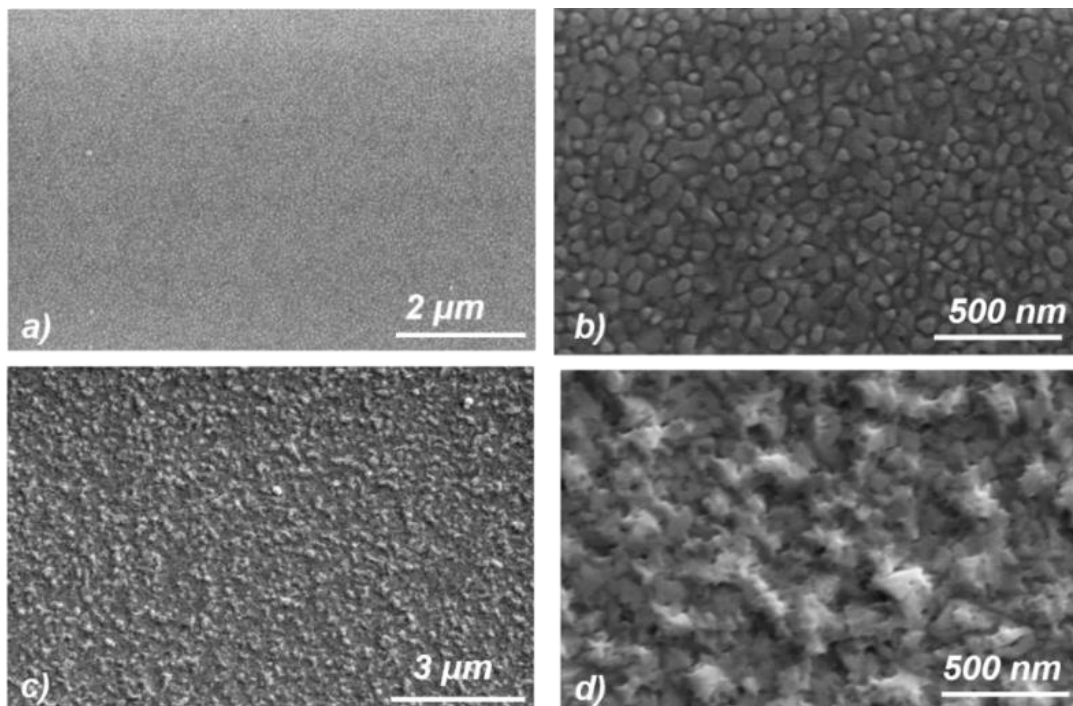


Figure 61. Demonstration of the healing effect of the EED process; a) and b) are the e-beam polycrystalline Au before and c) and d) are the polycrystalline Au film after EED treatment.

The healing effect can also be used to grow nano-patterned surfaces in such a way that, in opposed to grainy and polycrystalline features resulting from evaporation based techniques, EED chemistry grown nanostructures with more uniform crystalline formation are generated [Figure 62].

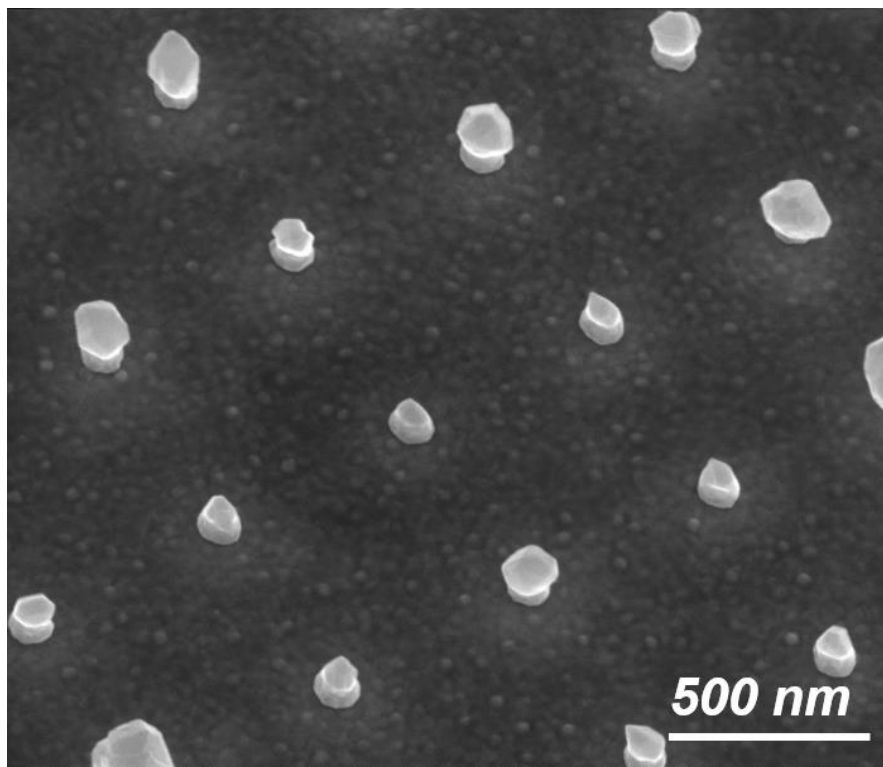


Figure 62. Au nanostructures grown on a polycrystalline Au substrate using EED process.

One major impact of this chemistry is in fabrication of plasmonic metasurfaces as was shown in previous chapters. The capability of plasmonic nanostructures in confining and focusing the electromagnetic radiation in very small regions and formation of hot spots, can be exploited for a variety of different applications. Chemical reactions can be induced using the locally excited SPs and an example of that can be found in plasmonic based water splitting devices that use local field enhancements to break water molecules to hydrogen and oxygen²⁻⁵. This chemistry also enables deposition of thin layers of metals which can be used to deposit known catalyst metallic surfaces, such as Pt, so that plasmonic excitation of the underlying metal (i.e. Au or Ag) does not get hindered. Such devices are now part of a research study in the Leach group.

The local field at the generated hot spots on plasmonic nanostructures can also result in material conversion. Early results obtained from Au metasurfaces fabricated with EED chemistry showed that such a process can lead to coating the metallic surface with a thin layer of a non-metallic material. It is well understood that changes in the dielectric material at the interface of plasmonic structures will impact the locally excited

SP resonance. It was observed that arrays of Au nanopillars coated with benzoic acid (BA) ($n=1.54$) can absorb more than 60% of photons at 785 nm wavelength. Exposing the BA coated array ($\Lambda=700$ nm, $d=250$ nm) to a laser with the same peak emission appeared to have led to conversion of the BA to reduced graphene oxide (rGO) [Figure 63].

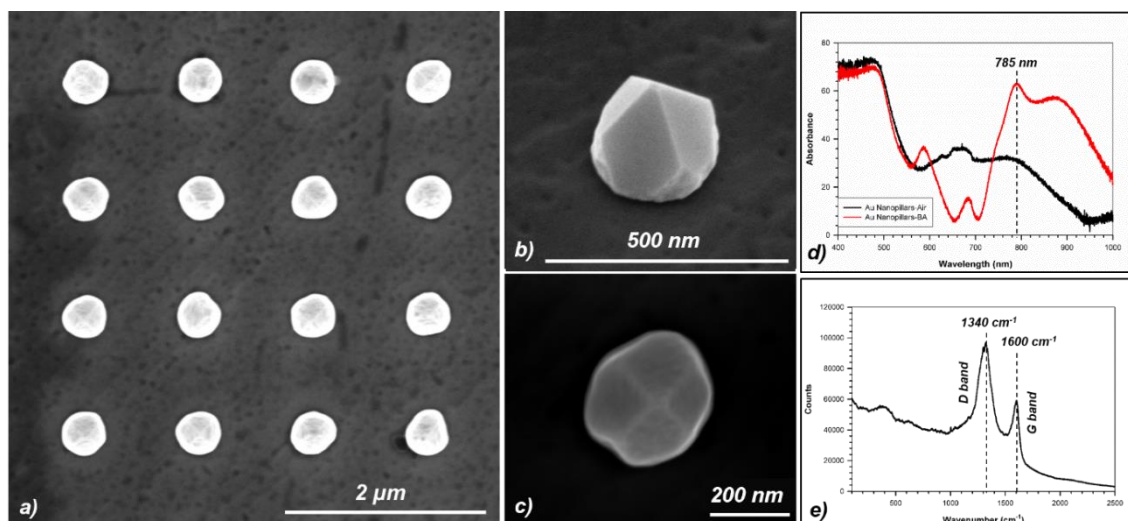


Figure 63. a) shows the SEM image of series of Au nanopillars after material conversion, an ordered textured surface can be noticed. b) is SEM image of a clean Au nanopillar before the addition of BA. c) SEM image of an Au nanopillar after exposure. d) is the absorption data of the same array before (black) and after being coated with BA (red), collected in an integrating sphere. e) is the Raman spectrum collected from the Au nanopillar array after the exposure.

Another area of impact of the presented EED chemistry, is in the fabrication of hot electron based photovoltaic and sensors devices (previously developed in the Leach research lab). A major hurdle in this field is the quality of the deposited metal films. Operation of such devices in the visible region of the electromagnetic spectrum requires low defect density metal-dielectric interfaces to maximize the conversion of photons to hot electrons which also impacts the probability of hot electron ejection from metal to the conduction band of adjacent semiconductor materials. Our proposed electrochemical process provides a low-cost metal deposition method through which ultra-smooth monocrystalline plasmonic metal films can be deposited which can be ideal for the fabrication of hot electron based devices.

Copper is another metal that was shown that can be deposited using this electroless deposition process. The Cu is also a known plasmonic metal that has not been explored to the same extent as other noble metals such as Au and Ag. This electroless deposition chemistry enables Cu to be also grown epitaxially on Ag(100) or Au(100) as planar films. Furthermore, metasurfaces made of Cu metal can also be made where the Cu can grow as single crystal metal nanostructures [Figure 64].

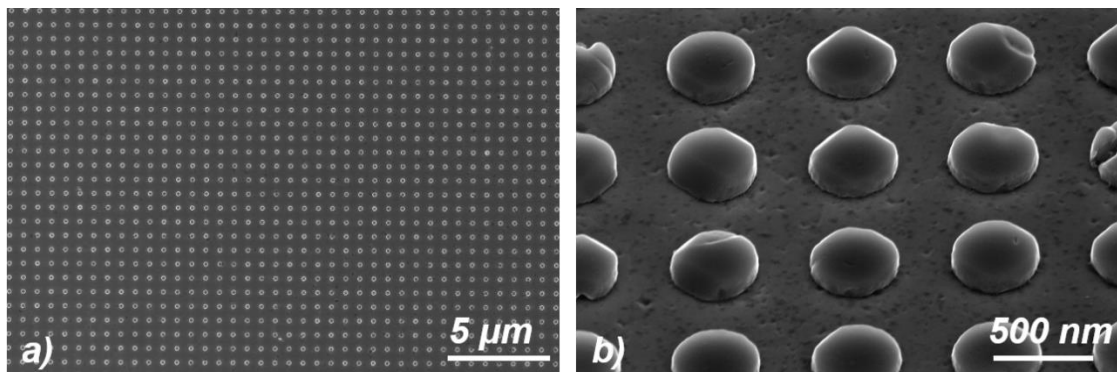


Figure 64. a) Cu metasurface array on Au(100) and b) is a tilt view of the same array of Cu nanostructures.

Copper metal is also of great interest for its contact killing effect in which bacteria that come in an intimate contact with the metal will get destroyed. Although the exact mechanism of the anti-bacterial effect is not quite well-understood, the phenomenon is under widespread investigation across the clinical research community.⁶⁻¹⁰ Our research group is currently involved in an ongoing research project with the Vancouver General Hospital (VGH) involving the use of SP excitation on Cu nanostructured surfaces as a way to improve the contact killing effect of the Cu metal by means of generating local heat through photo-thermal effects.

Additionally the described electrochemical deposition process can be utilized to make new metallic catalyst materials. It was shown that the process allows for co-reduction of known catalyst metal ions (i.e. Pt, Ir, Pd and Ru) with other metals to create new alloyed based metal films capable of improving catalytic effects. Some early results demonstrate that a combination of Pt-Ag and Pt-Au can lead to the lowering of hydrogen evolution reaction's overpotential in both acidic and basic solutions. It is noteworthy that

the mentioned results were obtained on smooth planar films. Scenarios in which 3D surface nanostructures with controlled size and well-defined crystalline facets are implemented can be a driver for further research in this field.

The presented applications mark only a few areas of impact of the developed electrochemical deposition process. Given the growing interest in the incorporation of photonics and plasmonics into different areas of research, it is fair to assume an ever growing horizon for use of such chemistry in many more different areas of research as the work progresses forward.

References

1. Miller, T., Samsavar, A., Franklin, G. E. & Chiang, T.-C. Quantum-Well States in a Metallic System: Ag on Au(111). *Phys. Rev. Lett.* **61**, 1404–1407 (1988).
2. Lee, J., Mubeen, S., Ji, X., Stucky, G. D. & Moskovits, M. Plasmonic Photoanodes for Solar Water Splitting with Visible Light. *Nano Lett.* **12**, 5014–5019 (2012).
3. Warren, S. C. & Thimsen, E. Plasmonic solar water splitting. *Energy Environ. Sci.* **5**, 5133–5146 (2012).
4. Szuromi, P. Plasmonic Water Splitting. *Science* **339**, 1125–1125 (2013).
5. Zilio, P., Dipalo, M., Tantussi, F., Messina, G. C. & Angelis, F. de. Hot electrons in water: injection and ponderomotive acceleration by means of plasmonic nanoelectrodes. *Light Sci. Appl.* **6**, e17002 (2017).
6. Santo, C. E., Taudte, N., Nies, D. H. & Grass, G. Contribution of Copper Ion Resistance to Survival of Escherichia coli on Metallic Copper Surfaces. *Appl. Environ. Microbiol.* **74**, 977–986 (2008).
7. Molteni, C., Abicht, H. K. & Solioz, M. Killing of Bacteria by Copper Surfaces Involves Dissolved Copper. *Appl. Environ. Microbiol.* **76**, 4099–4101 (2010).
8. Grass, G., Rensing, C. & Solioz, M. Metallic Copper as an Antimicrobial Surface. *Appl. Environ. Microbiol.* **77**, 1541–1547 (2011).
9. Zeiger, M., Solioz, M., Edongué, H., Arzt, E. & Schneider, A. S. Surface structure influences contact killing of bacteria by copper. *MicrobiologyOpen* **3**, 327–332 (2014).

10. Borkow, G. Using Copper to Fight Microorganisms. (2012).
doi:info:doi/10.2174/187231312801254723

Appendices

Appendix

Lift-Out Process for TEM

The steps that involved in preparing the sample for the TEM on the planar Au(100) film are shown below:

The desired region is chosen and coated with Pt protecting layer and then materials are removed using FIB around the selected area.

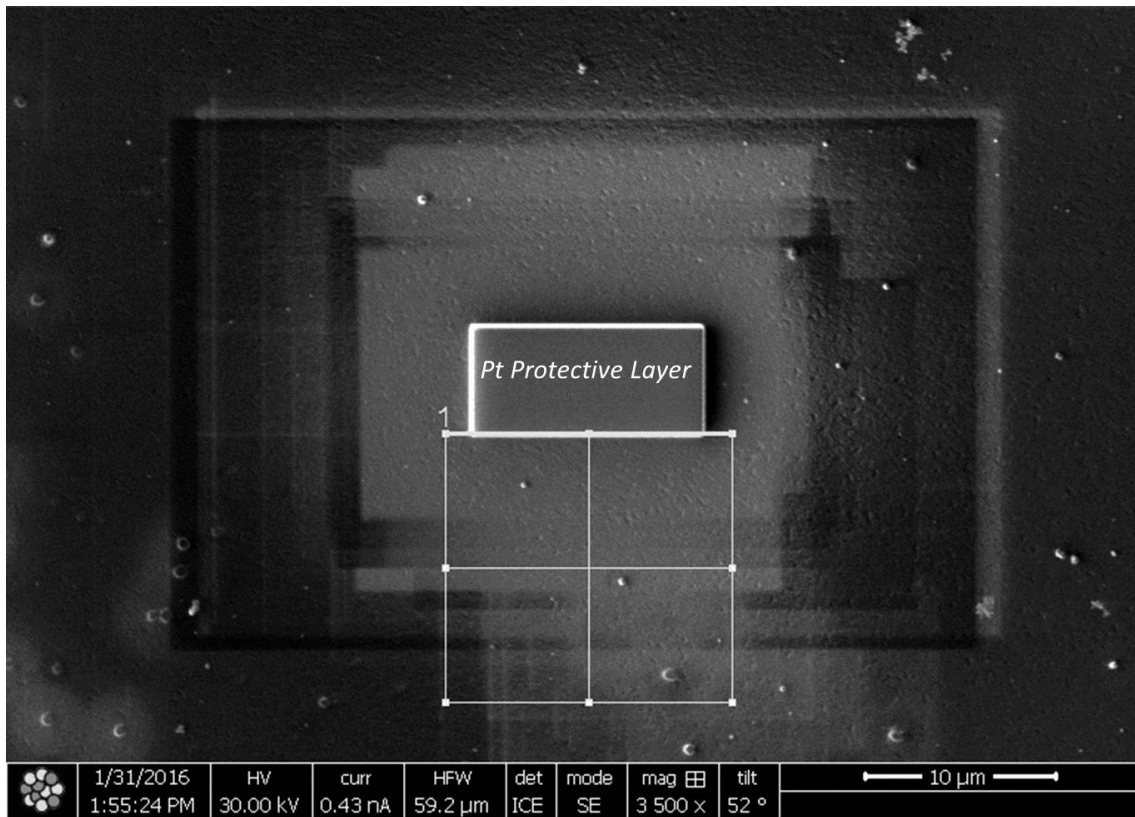


Figure A1. Image taken by FIB demonstrates the region that was chosen to be lifted-out and the area that was going to be milled away.

After removing materials from top and bottom of the selected area, the right end of the sample will be attached to a needle before completely detaching from the surface.

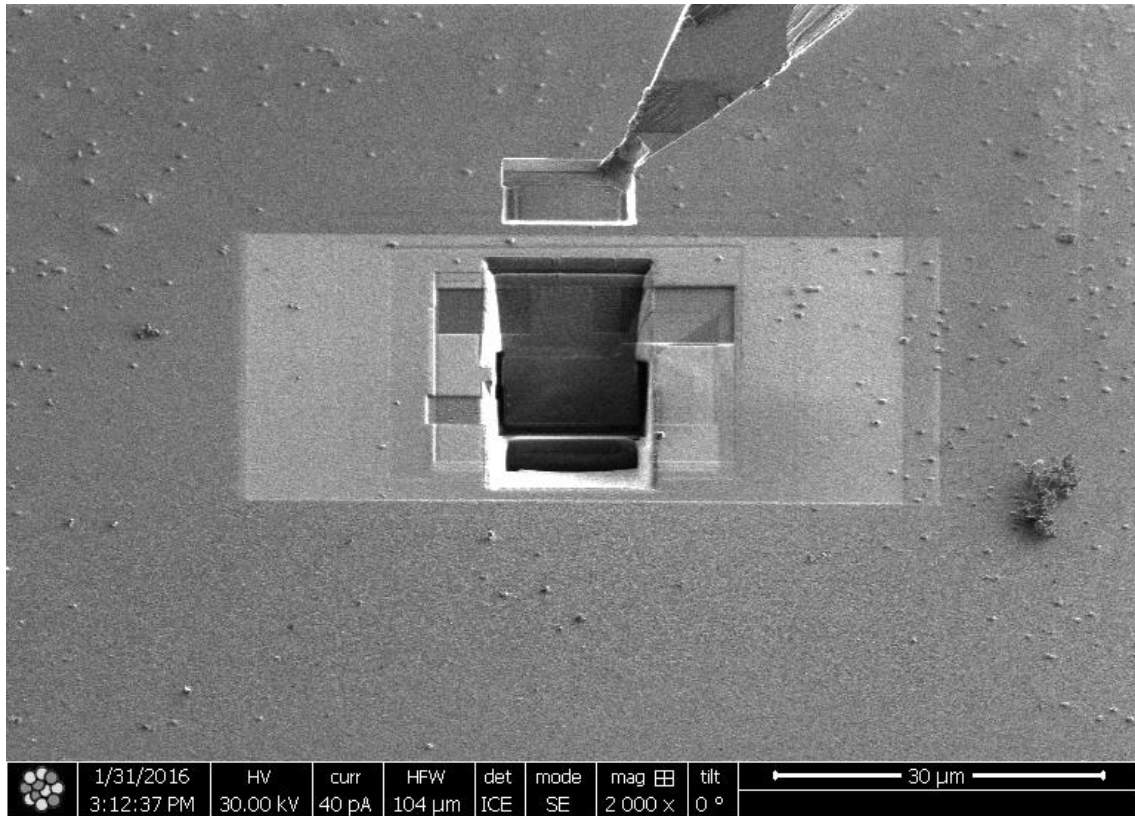


Figure A2. The removal of the specimen from the surface. The sample is attached to the needle and is lifted-out of the substrate.

Once the specimen is attached to the needle, the connected end of it to the surface will be milled away and the needle will be retracted from the substrate while carrying the attached specimen [Figure A2].

The sample now needs to be installed on the TEM grid to be further prepared for TEM analysis. A region on the TEM grid was prepared by milling away a portion of the material on the grid [Figure A3]. To avoid the sample to be bent after thinning process due to internal stresses, the area on the grid was prepared so that the specimen could be attached from both ends.

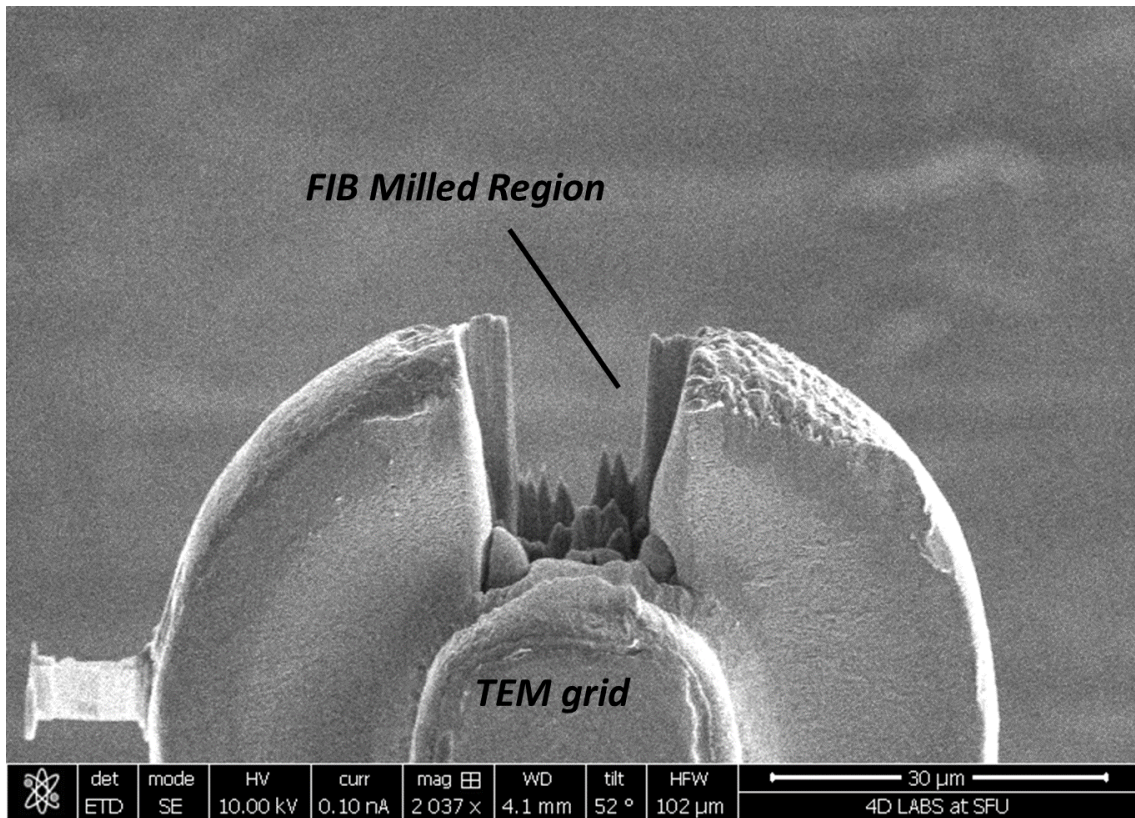


Figure A3. The TEM grid and the region that was prepared for the specimen installation.

After the region of interest is prepared on the TEM grid, the needle will be moved to the vicinity of the grid and then specimen from its loose end will be glued to the grid. Furthermore, the end of the specimen that is attached to the needle will be released by FIB milling and then glued to the grid as shown in Figure A4.

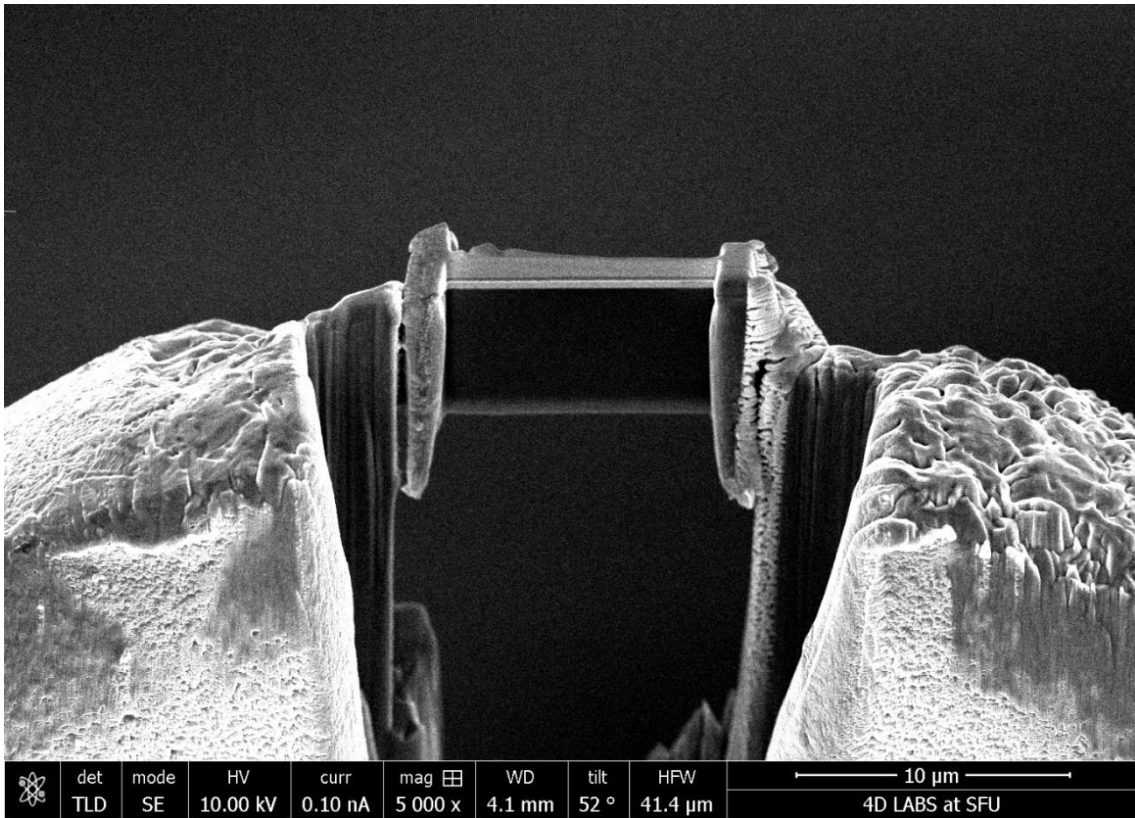


Figure A4. The installation of the specimen at the prepared region on the TEM grid.

The specimen then is thinned down to so that it becomes transmissive to electron beam during the TEM.

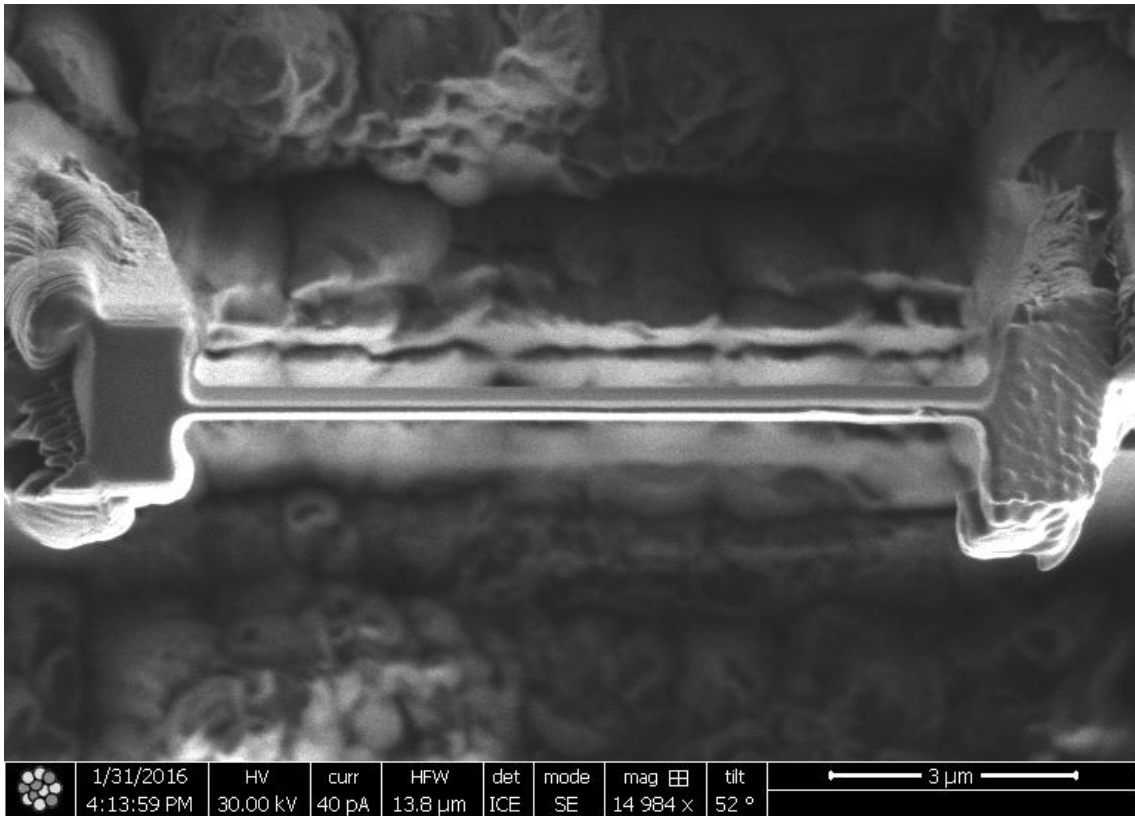


Figure A5. The top view image of the thinned down specimen taken by ion beam.

Similar approach was taken for performing TEM on Au sample with surface nanostructure. In this lift-out process, the specimen was attached only on one end to the TEM grid and a small portion of the sample was thinned down to prevent the it from bending due to internal stress.

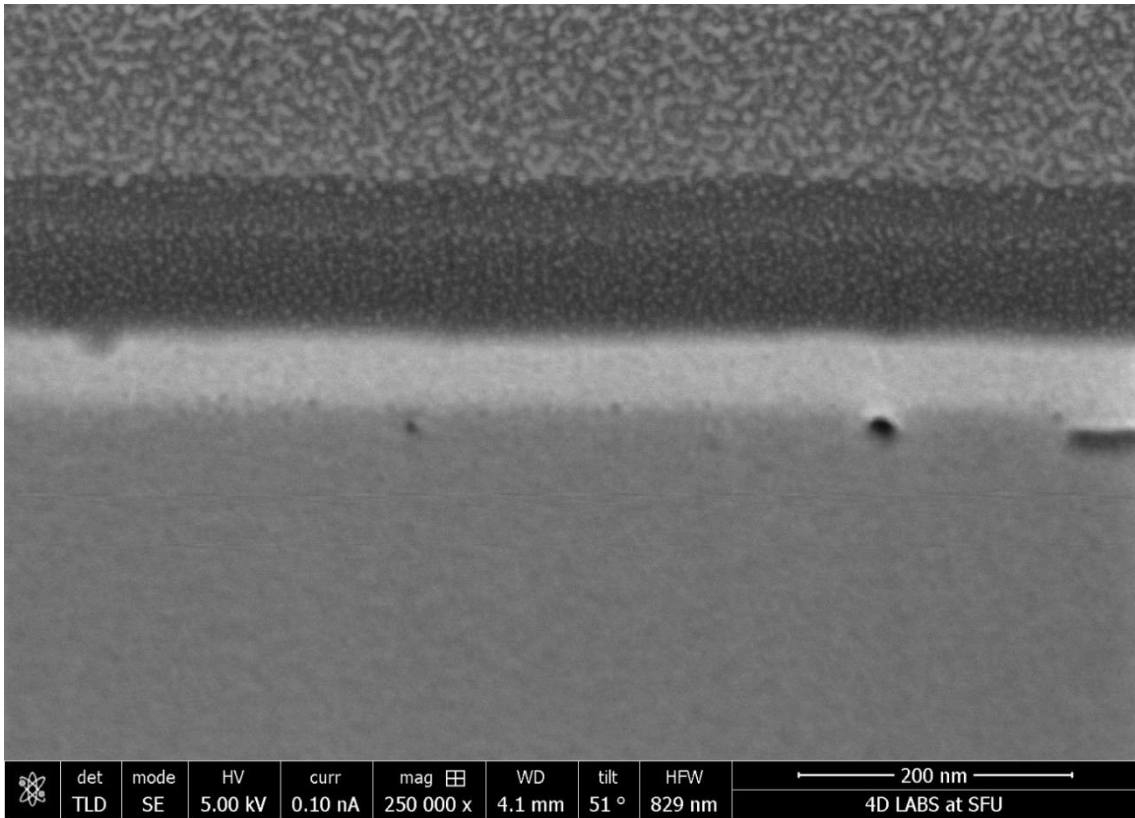


Figure A6. The cross-section SEM of the sample after it was mounted to the TEM grid.

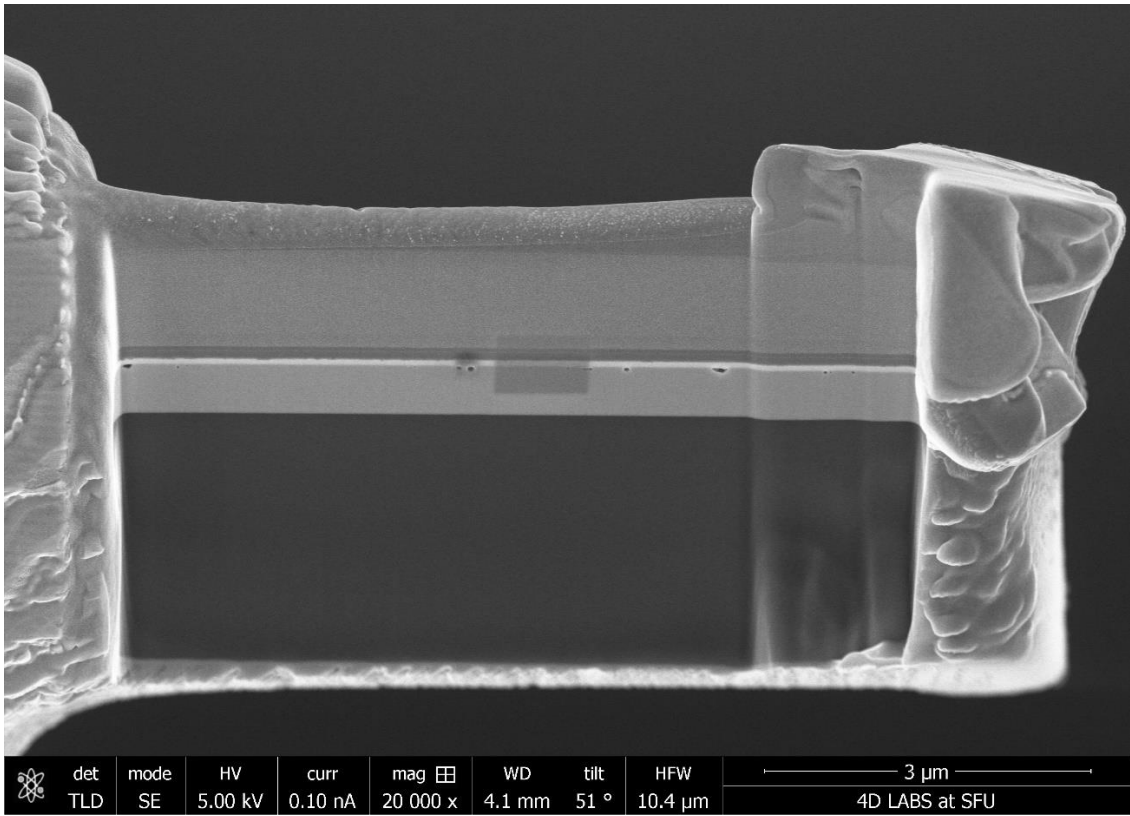


Figure A7. The cross-section SEM of the sample after 1st round of thinning.

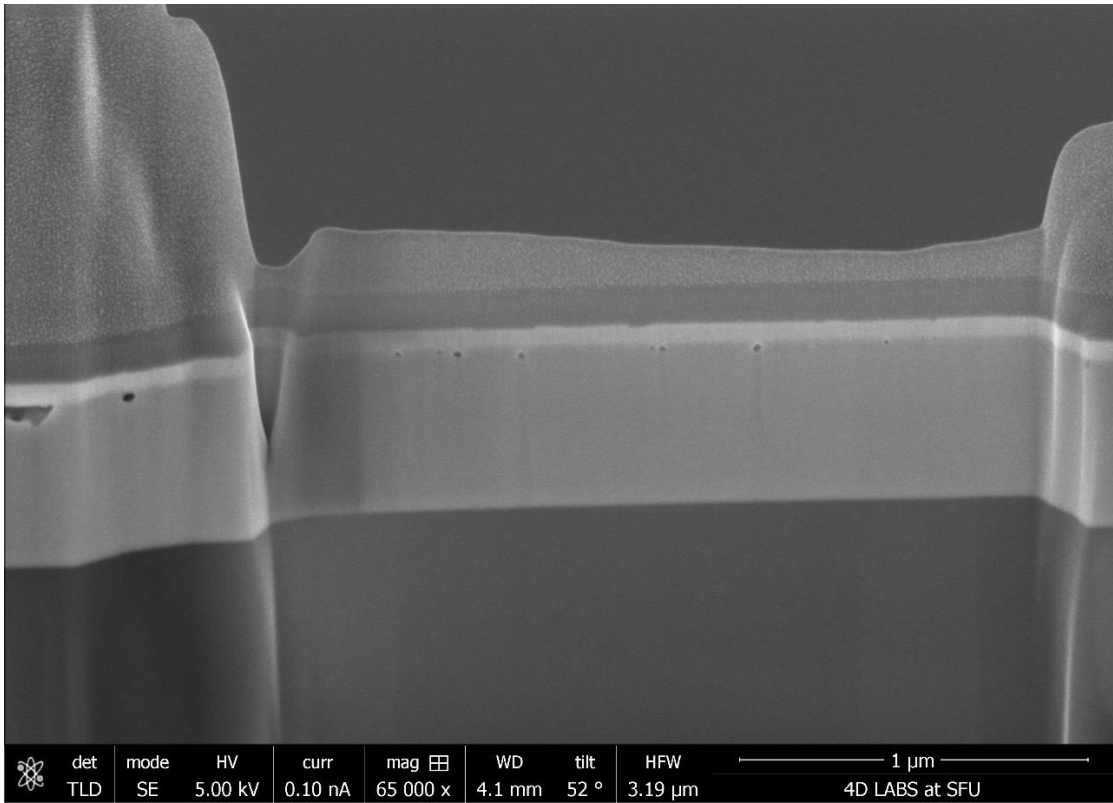


Figure A8. The cross-section SEM of the region of the specimen that was selected for more thinning ideal for TEM.

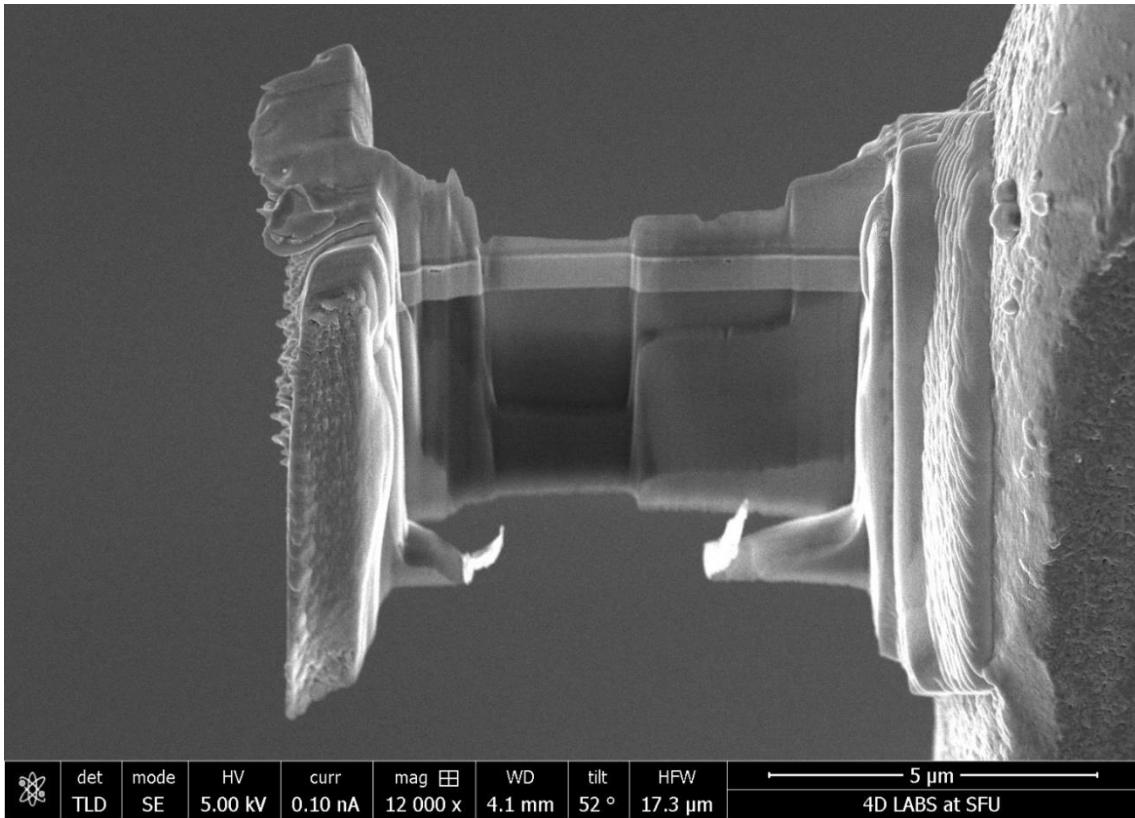


Figure A9. The cross-section SEM of the specimen after different round of thinning process. This image was taken after the stage was rotated to assess both sides of the sample during the thinning.

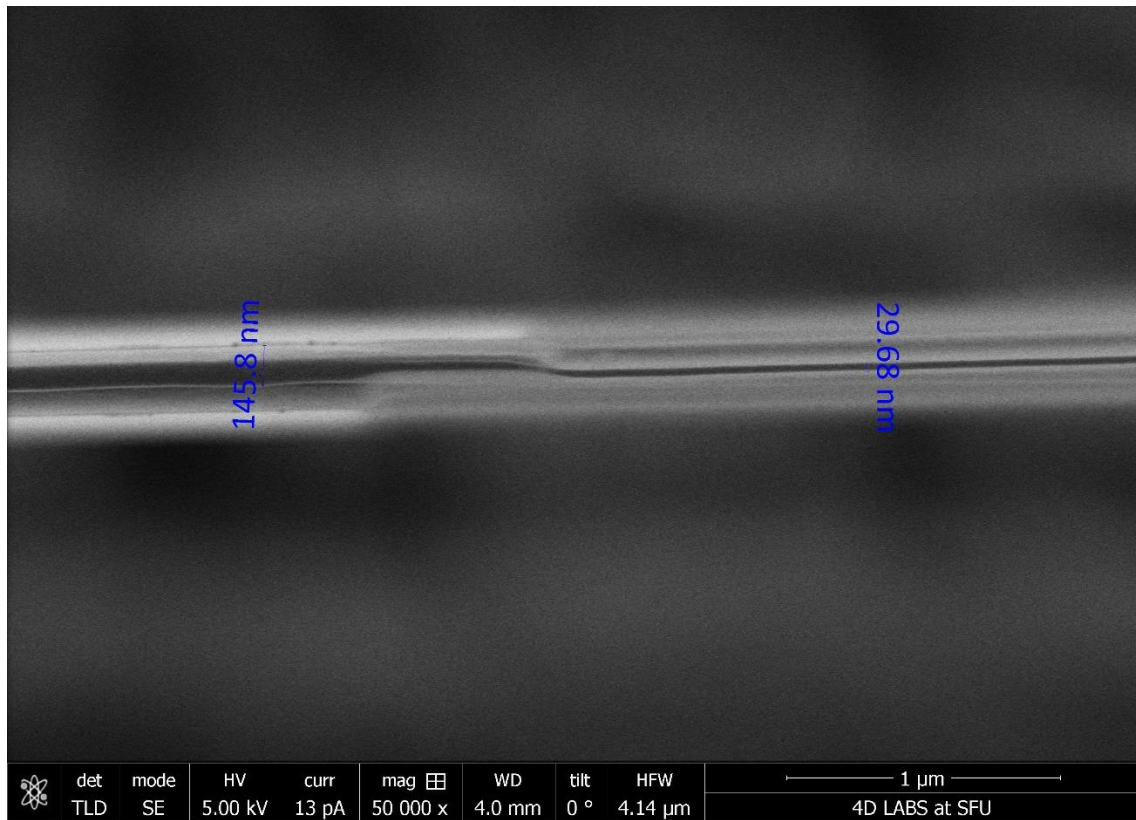


Figure A10. The top view SEM shows the final thickness of the specimen ready for TEM. The region that indicates ≈ 29 nm is where the TEM will be performed.

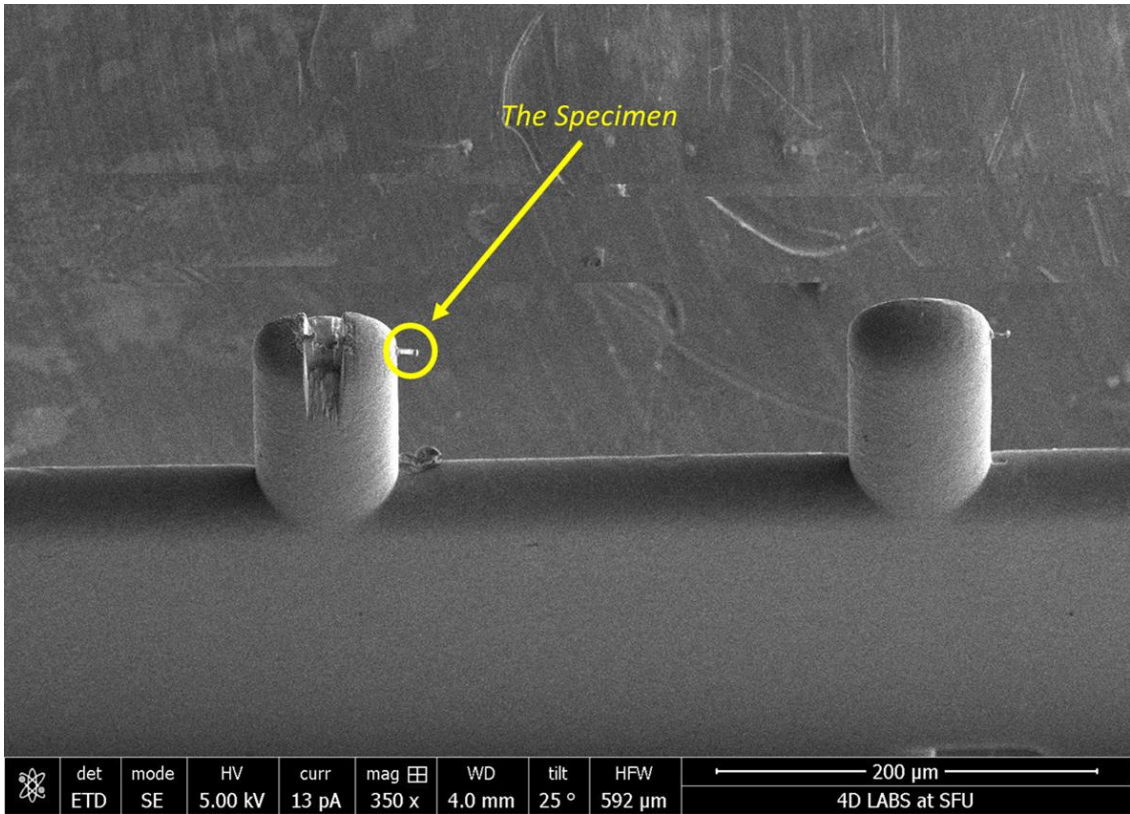


Figure A11. A view of the TEM grid with the specimen attached to it ready for TEM.